T H E U N I V E R S I T Y O F M I C H I G A N

COLLEGE OF ENGINEERING
Department of Engineering Mechanics

Special Technical Report

THE KINEMATICS OF THE PLASTIC FLOW OF GRANULAR MEDIA

Lawrence A. Larkin

ORA Project 05894

under contract with:

DEPARTMENT OF THE ARMY
ORDNANCE TANK-AUTOMOTIVE COMMAND
DETROIT ORDNANCE DISTRICT
CONTRACT NO. DA-20-018-AMC-0980T
DETROIT, MICHIGAN

administered through:

OFFICE OF RESEARCH ADMINISTRATION ANN ARBOR

April 1964

This report was also a dissertation submitted in partial fulfillment of the requirements for the degree of Doctor of Philosophy in The University of Michigan, 1964.

PREFACE

The author would like to express his appreciation to Professor R. M. Haythornthwaite for his suggestion of this topic and his guidance during the course of the research. Thanks are also due Mr. Milo Kaufman, Senior Laboratory Machinist, for his assistance and suggestions during the experimental portion of this work.

This work forms part of a program of research carried out under Contracts DA-20-018-ORD-23276 and DA-20-018-AMC-0980T between the United States Department of Defense and The University of Michigan.

TABLE OF CONTENTS

LIST OF TABLES

LIST OF ILLUSTRATIONS

LIST OF ILLUSTRATIONS (Continued)

LIST OF ILLUSTRATIONS (Continued)

LIST OF ILLUSTRATIONS (Concluded)

ABSTRACT

A plastic stress-strain relationship or flow rule is sought for a material obeying the Coulomb yield criterion. In this investigation a kinematic model is developed and experimental evidence is obtained which suggests that the model may have physical significance. The stress-strain relationship forms an essential part of the mechanics of deformable solids since it is generally recognized that the correct stress solution to boundary value problems must necessarily be associated with a deformation field. Furthermore, recent work in the theory of plasticity has shown that stress-strain relationships of a certain class can be sufficient for the establishment of uniqueness of the stress solution.

The analysis is made within the framework of the assumption of an ideal rigid-plastic material. Considering the available experimental evidence, it is not anticipated that this analysis will provide a useful approximation for materials other than relatively large-grained media such as sand.

The various proposed plastic stress-strain relationships are reviewed. Attention is given to the assumption of perfect plasticity and its theoretical and physical implications. The kinematic model of G. de Josselin de Jong is discussed in detail. De Jong's model, which is limited to plane strain, allows a deviation of the directions of principle stress and strain rate. His experimental observations show evidence of this phenomenon, and indeed it seems to be a likely explanation for other kinematic observations.

The application of this model to three-dimensional states of strain made by R. M. Haythornthwaite is further generalized by the addition of dilatation. The kinematic consequences of this model are investigated for the axially symmetric case. The model permits the directions of principal stress and strain rate to deviate except in those particular circumstances where perfect plasticity dilatations are occurring.

The stress and velocity equations for the various stress states satisfying the Coulomb condition can be separated into four groups. Of the two nontrivial groups, one is statically determinate, the other is kinematically determinate. Additional consideration is limited to the former group because of its apparent suitability to problems of classical interest and its mathematical convenience. The stress and velocity equations of this group are hyperbolic. In general, the stress and velocity characteristics do not coincide. However, the kinematic model allows just sufficient deviation of the principal di-

rections such that coincidence of one set of velocity and stress characteristics is possible.

The problem of indentation by a flat-ended, frictionless, circular punch was chosen for analysis and testing. Sufficient stress boundary conditions are present such that the stresses can be found independently of the stress-strain law. The stress characteristics and distribution were determined by a numerical procedure which was programmed on a high-speed digital computer. The surface radius of the deforming region was then determined for the cases of maximum deviation and zero deviation of the principal directions. This radius was selected as a kinematic observable since it was confirmed to be adequately sensitive to deviations in the directions of principal stress and strain rate.

Small scale punching tests were performed on a uniform Ottawa sand. The sequence of surface displacements was photographed and the failure load was recorded. The failure load was adequately predicted for the larger angles of friction corresponding to the higher densities of the material, however, it was underestimated for the lower angles of friction obtained with lower densities. The observed surface displacements demonstrated that the dilatation rate was essentially zero and that the deviation of the principal directions was close to the maximum value possible with the slip-expansion model developed in this study. This indicates that under certain circumstances, the kinematic model provides a physically appropriate flow rule for the Coulomb yield criterion.

CHAPTER I

INTRODUCTION

A law relating the kinematics of plastic flow to the stress state at failure is an essential part of the complete theory of the plastic failure of granular materials. Until recently, investigations concerning failure of a granular material were restricted to determinations of stresses, and the accompanying deformations were considered only in a qualitative manner if at all. This was due to the statically determinate nature of the governing stress equations obtained from the yield criterion and the equilibrium equations. However, for many boundary value problems there are not sufficient stress boundary conditions for a unique determination of the stresses. The additional information necessary was generally obtained by the application of a worst condition or similar extremum principle. However, in the mechanics of deformable solids, it is generally recognized that this information must be supplied by the stress-strain relationship and that the correct stress solution must be associated with a deformation field satisfying all of the deformation boundary conditions.

Recent work in the theory of plasticity has shown that stress-strain relationships of a certain type are sufficient for the establishment of uniqueness of solution to boundary value problems. If it is

postulated that the yield criterion relating the stresses at yield is also the plastic potential from which the strain increments at yield can be derived, then uniqueness of the stresses can be shown (see Hill[1]). This postulate, which has been widely accepted in connection with the yield of metals, has recently been extended to soils. However, unlike the situation for metals, the postulate that the plastic potential and the yield function are identical has led to results which are at variance with experimental data.

The purpose of this study is to obtain evidence of the actual laws governing flow in granular materials. The analysis here proceeds by idealized models which reproduce only the main features (and hopefully the important ones) of the actual material. Attention will be centered on axially symmetric flow. The approach will be to investigate the possible stress-strain relationships and to apply them to a statically determinate problem with a suitable flow observable. After the variation of this observable with the different stress-strain relationships has been determined, this problem will be reproduced in the laboratory and information concerning the law governing axially symmetric plastic flow will be inferred from the comparison of the experimental observations and the theoretical predictions.

A. COULOMB YIELD CRITERION

If the material is assumed to be isotropic, then the yield criterion must be a function of the stress invariants only, i.e., it must

not change for an arbitrary rotation of the coordinate axes. Drucker and Prager[2] proposed the following generalization of the Coulomb yield criterion (in principal stress form):

$$f(\text{yield}) = \alpha(\sigma_1+\sigma_2+\sigma_3)+\left[\frac{1}{6}(\sigma_1-\sigma_2)^2+(\sigma_2-\sigma_3)^2+(\sigma_3-\sigma_1)^2)\right]^{1/2} = k$$

When specialized to plane strain α and k can be determined in terms of the cohesion and the angle of friction. When plotted using the principal stresses as coordinates this function forms a right circular cone with the octahedral axis as its axis and with its apex in the tension octant. Shield[3] remarked that this yield surface is a valid generalization of the Coulomb law to three dimensions, but that there is no limit to the number of yield functions which reduce to the Coulomb law in two-dimensional problems. Shield then interpreted the Coulomb law as giving the limiting stress conditions on any plane in a three-dimensional mass of material. He then took the well known result obtained from the fact that the Mohr's circle representing the limiting stress state must be tangent to the two lines representing the Coulomb yield criterion in the σ-τ plane (see Figure 1-1),

$$\sigma_b N^2 - \sigma_a = 2cN, \qquad \sigma_b \geq \sigma_c \geq \sigma_a$$

$$N = \tan(\pi/4 + \phi/2)$$

where

c - cohesion

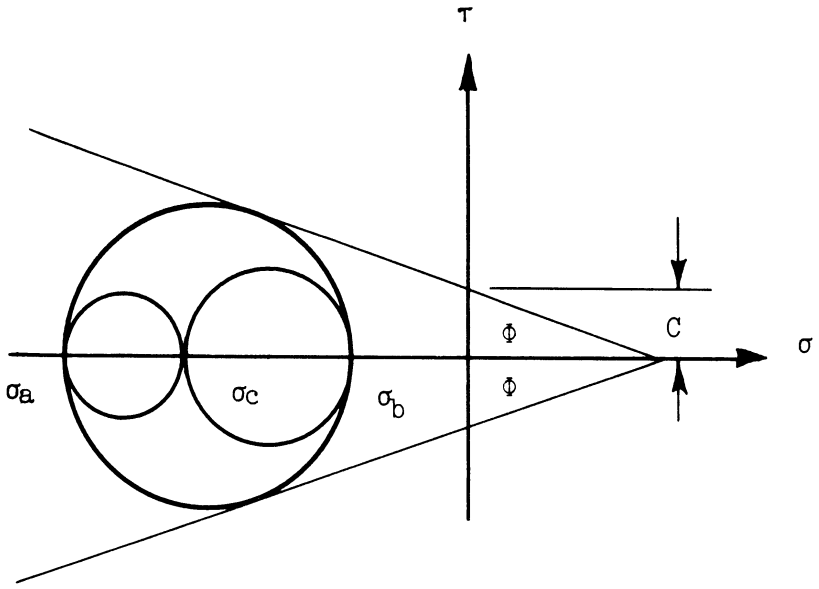

Figure 1-1. Mohr's circles for a general state of stress at failure in a Coulomb material.

and found the six possible planes obtained by substituting the principal stresses σ_1, σ_2, and σ_3 for σ_a, σ_b, and σ_c in all permutations. These six planes enclose a right hexagonal pyramid whose axis is the octahedral axis and whose cross section in the octahedral plane is an irregular hexagon as shown in Figure 1-2. Because of the mathematical convenience of the plane sides and the relative success of correlating with experimental data, this generalized Coulomb yield criterion will be used throughout this study.

From Figure 1-2, it is seen that the Coulomb yield surface for an isotropic material has 60° symmetry. Therefore an experimental determination of the yield surface can be made by considering stress states which lie on only one of the six segments. The ordinary triaxial soil testing apparatus is capable of only axial compression and axial extension tests which give stress states corresponding to the corners of the yield surface. The two usual methods of reaching stress states corresponding to intermediate points on a segment of the yield surface are testing a hallow cylinder with unequal internal and external pressure and an axial load, and stressing a specimen with combined hydrostatic pressure, torsion, and axial load.

Several investigations of the yield surface for sands have been reported. Habib[4] performed tests on specimens subjected to combined hydrostatic pressure, torsion, and axial load. He used solid cylindrical specimens in a dense condition. For intermediate stress states

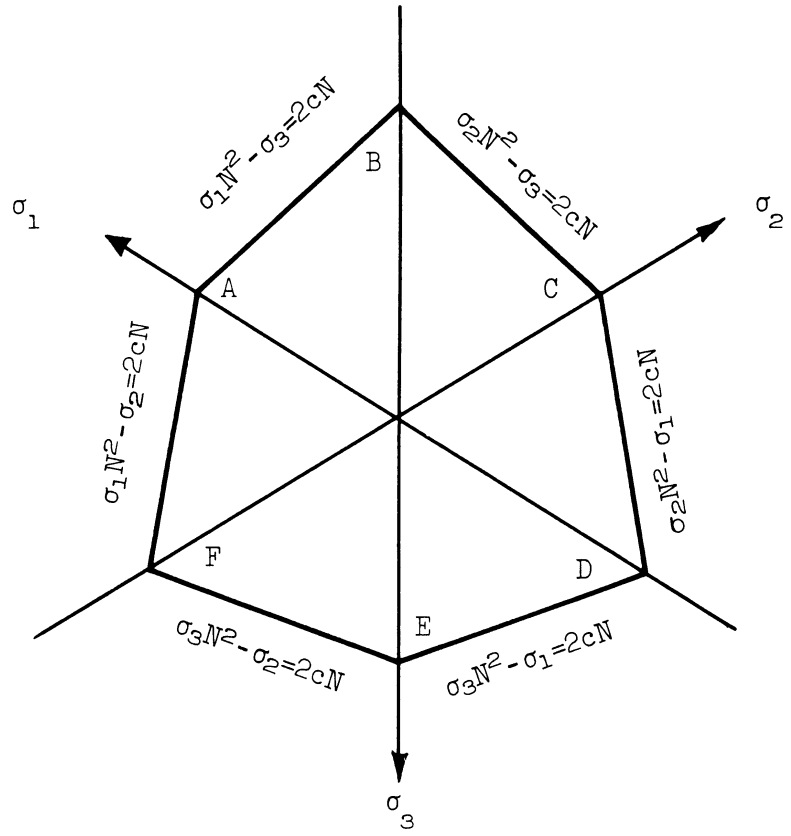

Figure 1-2. Section of the Coulomb yield surface in the octahedral plane.

his results deviated by as much as 5° or 16% from the yield surface standardized on the results from the standard compression test. Moreover, the extension tests gave an angle of friction of 7° or 22% lower than the compression test. Peltier[5] and Haythornthwaite[6] reported similar deviations in extension tests, while Kirkpatrick,[7] Wu, Loh, and Malvern,[8] and Bishop and Eldin[9] have found good agreement between the results of compression and extension tests. Kirkpatrick,[7] and Wu, Loh, and Malvern[8] have also reported experimental results with hollow cylinders loaded with additional axial load and unequal internal and external pressures. Kirkpatrick's tests essentially covered only one intermediate stress state and the samples were at the minimum porosity. He found the angle of friction to be 2° or 5% greater than that found by the standard compression test. The tests by Wu, Loh, and Malvern were more comprehensive. Their tests yielded an angle of friction which was greater than that given by the compression test by 14% at the most for the intermediate stress states tested.

B. IDEAL RIGID-PLASTIC MATERIAL

The ideal rigid-plastic material is homogeneous and time independent. The material remains rigid until the stresses in the material satisfy a certain yield condition, which is independent of the stress history or stress path and the rate of stress application. Furthermore, this yield condition is independent of the total strain. When the stress state satisfies the yield condition, unrestricted deformation

or flow can occur as long as unloading does not take place. As soon as the stress state retreats from the yield surface the material becomes rigid again. A stress-strain diagram along with an unloading cycle is shown in Figure 1-3. Note that there is no one-to-one correspondence of stress and total strain. Any number of strains correspond to the stress when it is at the yield level while during the unloading-loading cycle an infinity of stresses correspond to the same strain. Therefore, only a relationship between stress and strain increment or rate is anticipated. The material also lacks viscosity. Hence for quasi-static problems, only the ratios of the strain increments or rates will be found, not their actual values. The term "rate" or "velocity" used in this connection does not necessarily refer to time but it can refer to any suitable monotonically increasing quantity associated with progressive deformation. This is completely analogous to the basic hinge angle in the collapse mechanism of a beam or frame to which all the other hinge angles in the structure are proportional (e.g., see Hodge[10]).

Admittedly the ideally rigid-plastic material is a rather rough approximation to the actual behavior of materials. However the approximations made are not without good reason from the standpoint of mathematical tractability. Consider the problem of a surface footing or the problem of indentation with a flat-ended die as it is called in the literature on metal working. The theory of elasticity (e.g., see

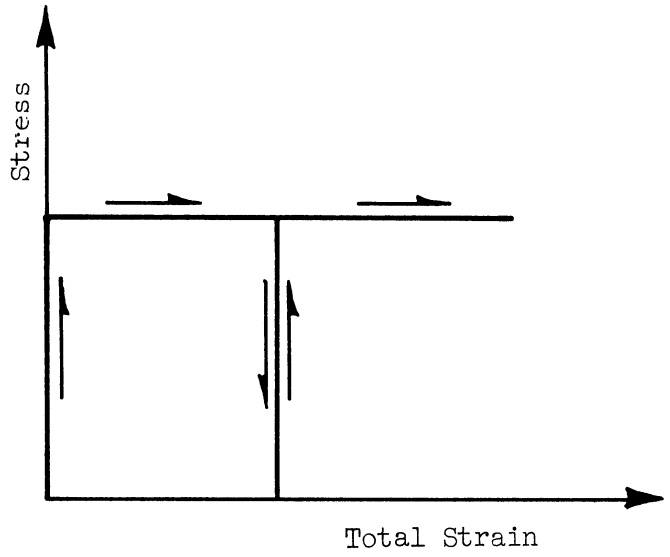

Figure 1-3. Stress-strain diagram for an ideal rigid-plastic material.

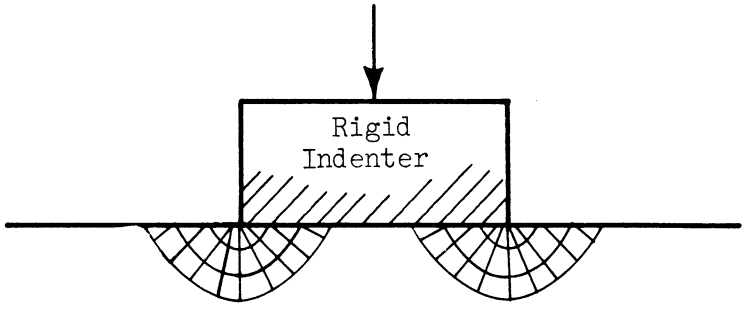

Figure 1-4. Constrained yielding under a rigid punch.

Timoshenko and Goodier[11]) shows the stresses to be infinite at the corners of the die. This indicates that yielding starts at these points from the onset of loading. Following a steadily increasing loading program, the yielded zones at any load below the ultimate collapse load may be as shown in Figure 1-4. When the material at the corners is stressed to yield, a mechanism comes into action, perhaps slippage, which prevents the stress state from going beyond the yield surface. When additional load is added, the material in the yielded zone may give or slip thus shifting the additional load to the rigid portion some of which subsequently yields. The footing or die is still supported by the rigid, unyielded body of material in the center until the load increases to the point where the yielded zone has extended completely under the die. At this load, flow of the material, possibly with the same kinematics as the mechanism for yield, is no longer restrained and may occur indefinitely unless arrested by the occurrence of some other phenomenon. In this case the predominant arresting factor is possibly the formation of a more favorable geometry due to the partial burying of the footing or die.

From this possible description of the yielding process in a boundary value problem, the simplicity of the ideally rigid-plastic material can be appreciated. With such a material, the stress state in the deforming mass must satisfy a yield condition which is independent of the stress path and which is maintained throughout the flow process.

Only the plastic strain rates at ultimate failure need be considered to complete the solution. The load and the extent of the plastic zone, at ultimate failure only, are investigated. Hence, the intermediate stages of progressive yielding, where the growth of the elastic-plastic interface is determined for each load increment, is ignored. Neglected too are the effects of strain hardening or weakening, the consideration of which requires a step-by-step determination of the strain history for each point throughout the yielded zone.

Turn now to the actual behavior of the material under consideration in this study. At the outset, fine-grained, cohesive materials will be ruled out. These materials are quite time-dependent, usually due to the presence of pore water. Further, their strength is usually quite dependent on the stress history. Instead, attention will be confined to relatively large-grained, permeable materials, with full drainage permitted, the strength characteristics of which are principally frictional. Since a great deal of testing has been done on sands, the following discussion will deal with this material exclusively although the analysis may well be applicable to other cohesionless, granular materials.

The typical stress-strain curves for sand as found in most textbooks on soil mechanics are shown in Figure 1-5. They are labeled simply as being for the loose state or the dense state. These curves are similar for either the triaxial or the shear box testing apparatus.

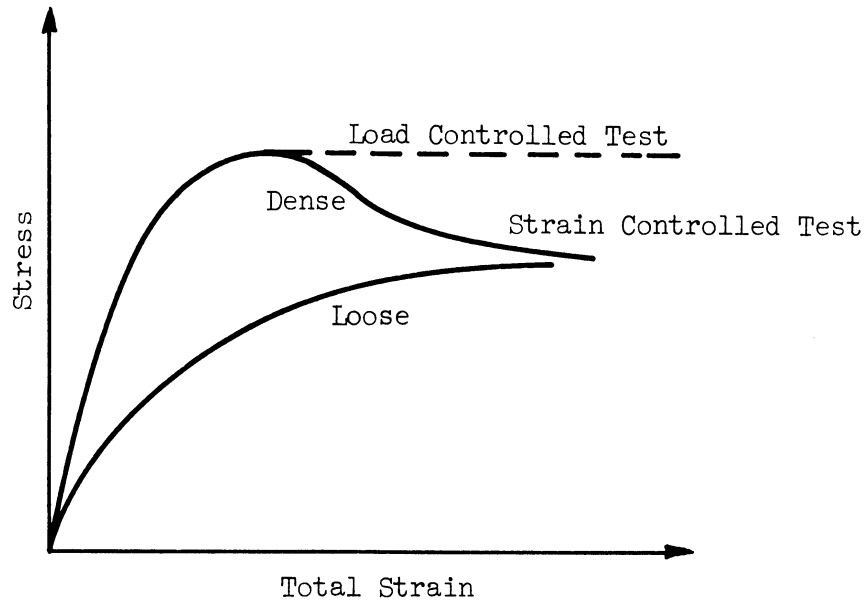

Figure 1-5. Typical stress-strain curves for sand.

The elastic limit is quite low for either density state and it is followed by an irreversible strain-hardening region. For a dense specimen tested in a strain controlled machine this strain-hardening portion is followed by a strain-weakening portion of considerable extent in some cases and finally by a fairly constant stress region which is reached only after considerable strain. The stress in the constant region is referred to as the ultimate or residual stress and the corresponding angle of friction as the ultimate or residual friction angle. Sand in the loose state exhibits a gradually decreasing strain-hardening rate which eventually becomes nearly zero. The strain at which flow occurs at fairly constant stress is usually quite large for both types of curves, anywhere from 5-20% total strain. Now, both types of stress-strain curves are departures from the ideal rigid-plastic material and their general shape is certain to be reflected in the load-

deflection curves in such tests as footing tests. Hence any results obtained by assuming the material to be ideally rigid-plastic cannot be expected to give good agreement with tests performed on a material for which the stress-strain curves have important deviations from the idealized model.

If the Coulomb yield surface as shown in Figure 1-2 is accepted as giving an adequate description of the failure condition for sands, then the yield surface can be established for a particular material by experimentally establishing one point on it such as a corner point which can be tested with the standard triaxial apparatus. The maximum angle of friction, obtained from the peak stress, is not a constant for a particular sand but is a function of the density. This angle of friction is usually correlated with the initial density. Hence the determination of the angle of friction-initial density relationship for a particular sand will require a series of tests. A noteworthy example of such a test series, using the standard triaxial apparatus, has been reported by Chen.[12] He was able to obtain very consistent results due largely to his exceptional specimen preparation techniques.

The question of dependence of the yield surface on the stress path or history has been investigated for the stress states attainable with the standard triaxial machine. In the standard compression test, the hydrostatic pressure is first applied and then the excess axial load is applied until failure. Bishop and Eldin[9] performed a series

of drained tests using four different stress paths to failure for compression tests. The entire range of initial densities of the particular sand was tested. The stress paths followed were: (1) application of hydrostatic pressure and then the application of the excess axial compression; (2) application of the hydrostatic pressure, then maintaining the axial stress constant, the pressure was reduced until failure; (3) stressing with an all-around pressure to 101 psi and then reducing the pressure to 5 psi from which point an axial pressure was added until failure as in the standard test; and (4) application of the vertical load and the ambient pressure, varied in such a manner that no lateral strain occurred, until the pressure reached 30 psi and then the standard compression test was carried out. Axial extension tests were also performed with failure being produced by increasing the lateral pressure while holding the axial stress constant and by decreasing the axial stress while holding the lateral pressure constant. The tests exhibited only small scatter and the results show that the angle of friction is practically independent of the stress path and that it can be expressed as simply a function of the initial density.

Conclusive results concerning the effects of the rate of loading on the strength of sands have been difficult to achieve due to the added difficulties encountered in dynamic testing. Casagrande and Shannon[13] carried out a test series on a dense, dry sand in the drained condition. However, the scatter in the results prevent any definite

trends from being observed. Through an extensive series of tests, Whitman[14] was able to conclude that the variation in the friction angle in the range of loading times from 5 minutes to 5 milliseconds is not more than 10% for dry sands. The effects of loading rates on saturated sands is more serious however. Saturated samples in a drained condition were tested by Seed and Lundgren[15] at three various rates of loading called static, slow, and rapid with loading times of 10-15 minutes, 4 seconds, and .02 second, respectively. First, the results of the rapid tests on drained and undrained specimens were essentially the same, indicating that, although provisions are made for drainage to take place, the rate of loading in the rapid test is so fast that there is no time for drainage to occur and excess or negative pore pressures will develop. Hence, for a drained test on a dense, saturated, fine sand, the strength was somewhat higher for the slow tests and up to 40% higher for the rapid tests than for the static tests, and for a dense, saturated, coarse sand, the strengths for the slow and static tests were the same, but the rapid tests were again up to 40% higher.

CHAPTER II

KINEMATICS OF PLASTIC FLOW

As discussed in the definition of an ideal rigid-plastic material, the one-to-one correspondence of stress and total strain which exists for an elastic material will not be expected for a rigid-plastic material. The only simple relationship expected between the stresses and the deformations is a relationship between the stresses at a point at an instant and the strain increment or the strain rate at that point at that instant.

The first plastic stress-strain rate relationship for solids was proposed by St. Venant.[16] It was restricted to plane strain only. The relationship was obtained by assuming zero volume change and coincidence of the maximum shear stress and maximum slip directions. Shortly thereafter, M. Levy[17] generalized St. Venant's equations into a stress-strain rate law for the general three-dimensional case. The next notable advance was by R. von Mises when he made the hypothesis that the strain increments were proportional to the derivatives of the yield surface with respect to the corresponding stress components. He gave this hypothesis two physical interpretations[18]: firstly, for a body at the yield stress the strain rates occur in such a manner that for infinitely small variations of stress inside the yield surface no additional work

is dissipated; and secondly, the actual dissipated work of deformation is an extremum compared to all other amounts of work which would be dissipated by neighboring states of stress on the yield surface acting through the same strain rates. Both of these interpretations become obvious when one realizes that the hypothesized strain rates are proportional to the components of the normal to the yield surface. More recently D. C. Drucker[19] has given the normality of the strain rate components a somewhat different interpretation by postulating that for an ideally plastic material, the net work done by an external agency over the cycle of application and removal is positive or zero if plastic deformation has occurred in the cycle. This assumption of normality of the strain rate components to the yield surface has been termed the assumption of perfect plasticity or alternatively, a material whose strain rate components are normal to the yield surface is called a perfectly plastic material.

These stress-strain rate laws were developed primarily to describe the flow strains for ductile solids and although very plausible physical explanations or work postulates may be given to them and certain uniqueness and variational theorems can be formulated from them, correctness of solution is desired and the real test of their validity lies in their agreement with experimental results.

Recently, the assumption of perfect plasticity has been applied to granular materials.[3,6,19] Since the yield surface is in the shape

of a pyramid, the strain rate components normal to this surface predicts that a perfectly plastic Coulomb material will have a certain expansion rate during plastic flow. This expansion or dilatancy is a well known property for sands, except when they are in a very loose condition. However, it is also recognized that the expansion rate starts to decrease after some deformation and eventually drops to zero. Hence it has been suggested that the perfectly plastic flow rule be limited to initial motion problems or to problems involving small total strains; but even then, the predicted dilatation rate is usually several times the experimentally observed rates.

Consider a set of data for a standard triaxial test showing the corresponding volume changes for the total axial strains. An initial contraction usually occurs which is followed by a dilatation except in very loose sands. As can be seen from Figure 2-1, the initial contraction is associated with the preflow region while dilatation can be approximately associated with the flow region of the stress-strain curve. For plastic strain rates it is this dilatation rate during flow which is important, not the total volume change. Haythornthwaite[6] has shown that for a sand to be acting like a perfectly plastic material, the curve relating percentage volume change and total axial strain should have a slope of

$$\frac{d\left(\frac{\Delta V}{V}\right)}{d\epsilon} = \tan^2(\pi/4 + \phi/2) - 1$$

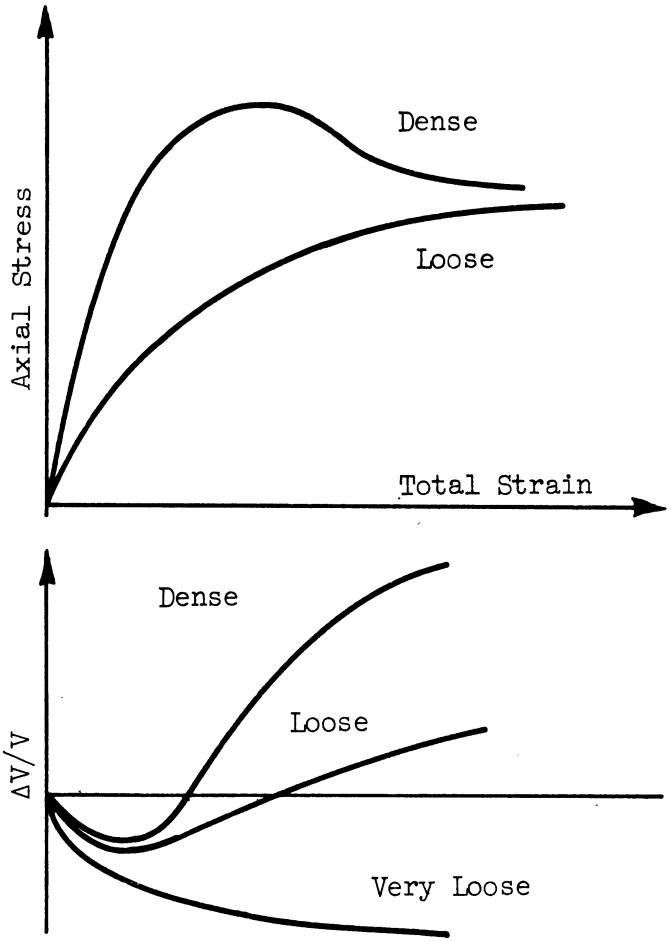

Figure 2-1. Typical stress-strain and volume change diagrams from triaxial tests on sands.

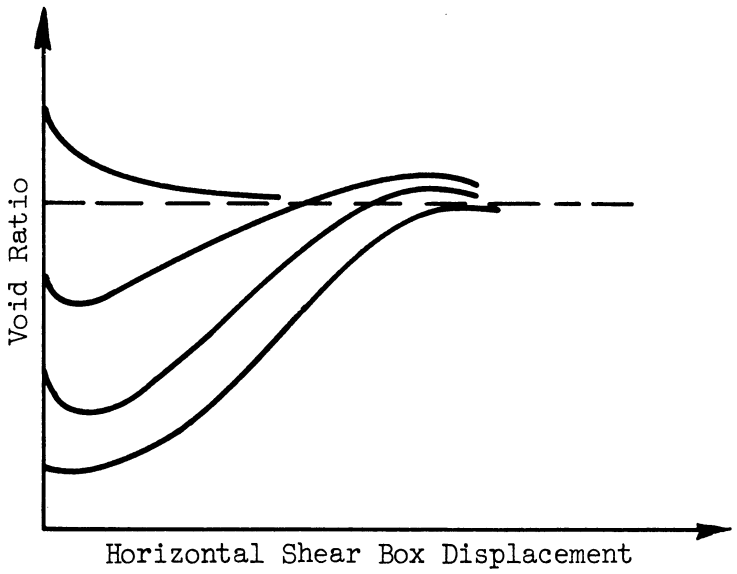

Figure 2-2. Variation of the void ratio with shear box displacement.

regardless of the size and shape of the deforming region. He measured the actual dilatation rate for a series of triaxial specimens with an initial porosity in the range of 50%. The largest dilatation rate observed was about 20% of that value predicted by the perfect plasticity assumption. Comparison of the volume change curves from triaxial tests with the results shown in Table I will show that, in general, the volume change rates for the perfectly plastic assumption are much too high.

TABLE I

SLOPE OF THE VOLUME CHANGE CURVE FOR PERFECT PLASTICITY

ϕ	$\tan^2(\pi/4 + \phi/2)-1$
25°	1.46
30°	2.00
35°	2.69
40°	3.60

These dilatations or expansions accompanying the yielding of granular media have been carefully studied by Roscoe, Schofield, and Wroth.[21] Using the shear box designed by Roscoe[22] to impose uniform simple shear strain on samples and hence making it possible to determine the void ratio with some reliability at all times during the test, they were able to establish the existence of a unique void ratio, which is reached, after sufficient yielding has occurred, regardless of the initial void ratio of the soil sample. In Figure 2-2 are shown the void ratio paths

of samples at various initial void ratios. It can be seen that samples on the dense side of this critical void ratio expand until this void ratio is reached and then no further volume change occurs and that samples on the loose side contract to the critical void ratio. This void ratio was found to be a function of the normal pressure. The investigators used sand, glass beads, and 1 mm steel balls for their tests on cohesionless materials. These tests have shown that the dilatation rate during initial plastic flow is strongly dependent on the initial void ratio, and that for large total strains involved in continued plastic flow, the dilatation rate is zero.

In order to reconcile the assumption of perfect plasticity with the experimental results, thereby retaining the benefit of a proof of uniqueness of stress and of the upper and lower bound theorems, etc., strain-hardening models have been proposed. The essential feature of the models, as far as the expansion rates are concerned, is that the yield surface is terminated in the compression octant of principal stress space. In the model proposed by Jenike and Shield[23] the terminating surface is a plane perpendicular to the hydrostatic stress axis and a semisphere or similar surface was proposed by Drucker, Gibson, and Henkel.[24] With the yield surface so terminated, zero or even contracting strain rates are possible for certain states of stress. These yield surface models are capable of describing many more of the features of the phenomenon of plastic flow in granular materials than

the rigid-plastic model, but it should be realized that in order to show uniqueness of stress with these strain dependent yield surfaces, the initial surface must be known and the history of strain known throughout.

Therefore, it appears that if the simplicity of the rigid-plastic analysis is retained and if a flow rule giving acceptable dilatation rates is desired, then the assumption of perfect plasticity must be dropped and with it much of the restrictiveness concerning the uniqueness of stress at yield. The most obvious step is to assume the volume change is negligible and that the directions of principal stress and strain rate coincide. This has been done by several investigators.[25,26,27] However, experimental evidence and the ability to explain certain kinematic phenomena make the flow rule proposed by G. de Josselin de Jong appear more promising. De Jong restricted his considerations to the plane strain problem. He obtained the kinematics of granular materials from a model in which deformations occurred by slip or glide along certain directions. De Jong reasoned that since the supposed mechanism for yield and redistribution of stresses in a granular material was slippage along the critical Coulomb shear planes, then it would be reasonable to use such a mechanism to describe the flow kinematics. For the zero volume change condition de Jong considered plane strain flow to be composed of a linear combination of two independent slips along critical shear planes as shown in Figure 2-3.

Figure 2-3. Distortion of a plane element by slips on critical shear planes.

This kinematic model allows the remarkable result that the directions of principal stress and strain rate do not necessarily coincide and that they can deviate by as much as $\phi/2$ in either direction. Furthermore, when $\phi = 0$, the directions of principal stress and strain rate do necessarily coincide, a fact which has been experimentally justified for metals. For an arbitrary dilatation rate, the slip along the critical shear plane can be replaced by an expanding layer. Here again the directions of principal stress and strain rate do not necessarily coincide but the amount of deviation is less and it is dependent on the expansion rate. It is interesting to note that when the expansion rate coincides with that required by the perfect plasticity assumption, then de Jong's slip model gives the same flow rule as the perfect plasticity flow rule and the directions of principal stress and strain rate do necessarily coincide. Haythornthwaite[29] has applied de Jong's

model to three-dimensional states of strain. He investigated the kinematic consequences of this model for the case of zero dilatation and axial symmetry. He found much the same results concerning the possible amount of deviation of the principal directions.

Coincidence of the directions of principal stress and strain rate is a necessary consequence of the combined assumptions of isotropy and the existence of a functional relationship between stress and strain rate, or equivalently, from the assumption that the strain rates are derivable from a potential which is a function of the stress invariants. Therefore, lack of coincidence does not necessarily imply lack of isotropy but instead, shows the lack of a functional relationship between stress and strain rate.

A similar flow rule for plane strain deformations has been hypothesized by S. Takagi.[30] Essentially, his flow rule contains an arbitrary expansion rate and a corresponding deviation of the principal directions such that one set of stress characteristics and one set of velocity characteristics coincide. There is a good possibility that this frequently occurs as will be seen in the following paragraph, but Takagi states that this must be true in order to satisfy conditions on boundary lines, or to connect two discontinuous solutions across a line. This statement does not seem to be justifiable. Although discontinuous velocity fields are generally joined by a velocity characteristic, this is a kinematic phenomenon and there seems to be no justifi-

cation for assuming that this is necessarily a critical Coulomb shear plane or stress characteristic.

The rupture planes or boundaries between the undeforming and the deforming material is the most readily and most often observed kinematic phenomenon of flow. In many tests where the rupture planes have been observed, the stresses are not known throughout the entire deforming region because of the presence of deformation boundary conditions. However, the stresses in certain portions of the deforming region can be completely determined by the known stresses on the boundary, the yield condition, and the equilibrium equations. These statically determined regions are shaded in Figure 2-4. Note that the extent of the statically determined region cannot be predicted, only its shape. Hence, in each of these problems the principal stress directions are known in a certain, not insignificant, zone. The rupture plane is a kinematic quantity and it must be a zero extensional strain plane (see discussion by Shield[31]). The Mohr's circles for strain rates are shown in Figure 2-5 for de Jong's theory and for the perfect plasticity theory for plane strain. It can be seen that for the perfect plasticity theory, both the critical Coulomb shear stress planes are zero extension planes or potential rupture planes while de Jong's kinematic theory allows the strain rates enough freedom such that one of the potential rupture planes can coincide with one of the critical Coulomb shear stress planes. Therefore, if the expansion rates are less than that required by perfect

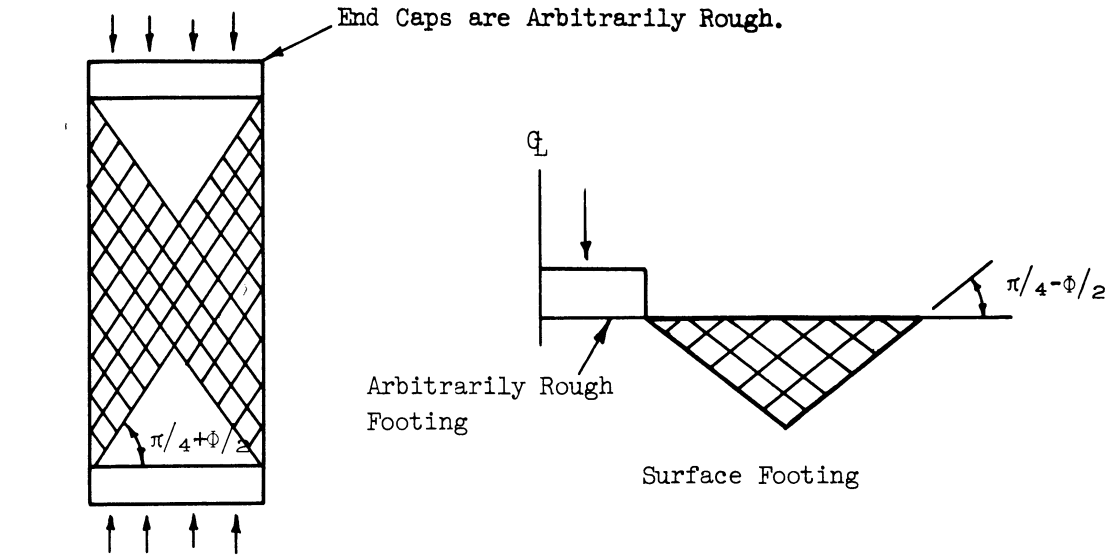

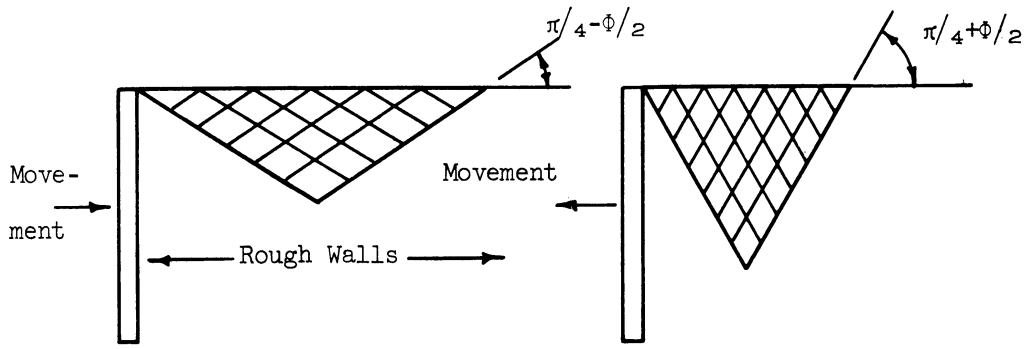

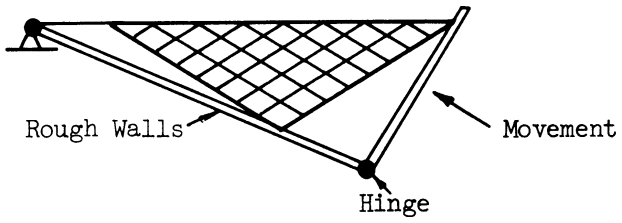

Figure 2-4. Statically determined regions in some plane strain problems with mixed boundary conditions.

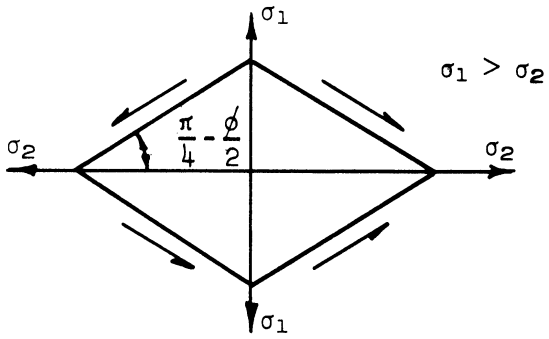

Orientation of Coulomb Shear Planes to Principal Stress Directions

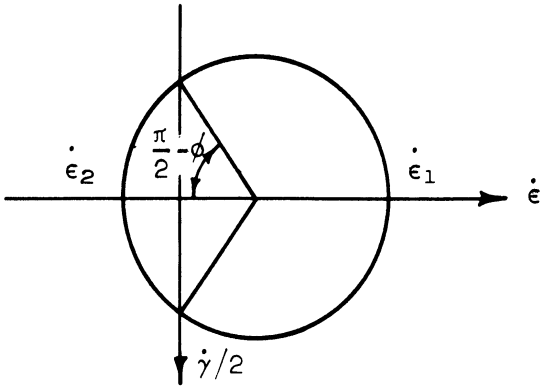

Perfect Plasticity Assumption

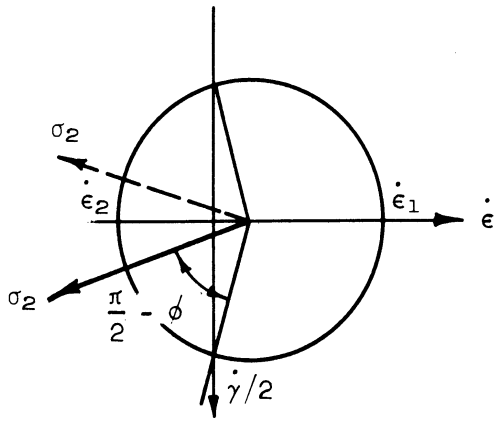

Positive Expansion

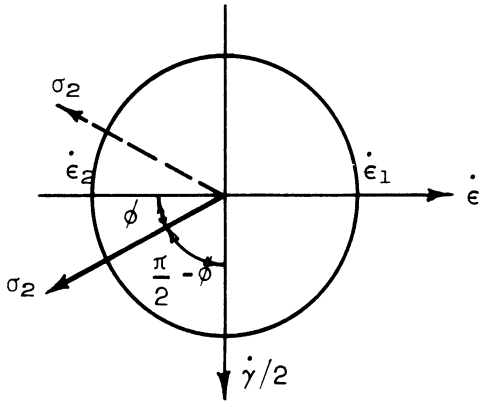

Zero Expansion

De Jong's Theory with Maximum Deviation of Principal Directions

Figure 2-5. Relations between the Coulomb shear stress planes and the rupture planes.

plasticity, then the occurrence of coincidence of the rupture planes with the Coulomb shear planes is a good indication of the occurrence of deviation of the directions of principal stress and strain rate. The coincidence of rupture planes and the Coulomb shear planes is in evidence in many triaxial specimens, in footing tests (see Sylwestrowicz,[32] or Selig and MeKee[33]), and in model retaining wall tests (see J. Brinch Hansen[25]). A detailed experimental study concerning the possibility of deviation of the principal directions was also made by de Jong.[28] Using the apparatus shown in Figure 2-4, he measured displacement increments, rupture lines, and strain rates by means of photographs and reported further evidence supporting the occurrence of the deviations of the directions of principal stress and strain rate.

The deviation of the directions of principal stress and strain rate may be difficult to accept because of the notion that isotropy necessarily implies coincidence of the principal directions. It is much to de Jong's credit to have made this deviation plausible through the use of his slip model. Indeed, this deviation seems to be a likely explanation for the occurrence of commonly observed rupture planes and other kinematic phenomena which de Jong studied in detail.

CHAPTER III

FLOW RULE FOR A FRICTIONAL DILATING MATERIAL

In this section flow rules for the cases of plane strain and axial symmetry will be investigated by the use of a slip-expansion model. Extending the ideas of de Jong,[28] and Haythornthwaite,[29] it will be assumed that the general plane strain and axially symmetric velocity state is caused by independent slips and expansions on any or all planes on which the critical or limiting Coulomb shear stress is acting. It will be seen that such a model will not restrict the principal strain directions to coincide with the principal stress directions, but instead it will only limit the possible deviations between the two. It should be noted that the perfect plasticity flow rules associated with the Tresca yield criterion and with the Coulomb criterion can be shown to be special cases of this flow rule.

The Coulomb yield surface has been previously discussed in Chapter I and illustrated in Figure 1-2. It is recalled that this surface can be constructed by plotting the Coulomb yield criterion in the normal stress-shearing stress plane and constructing the Mohr's circles for permutations of the principal stresses. These circles are shown in Figure 3-1 for any side regime and any two diametrically opposite corner regimes. For a side regime, which is a side exclusive of end

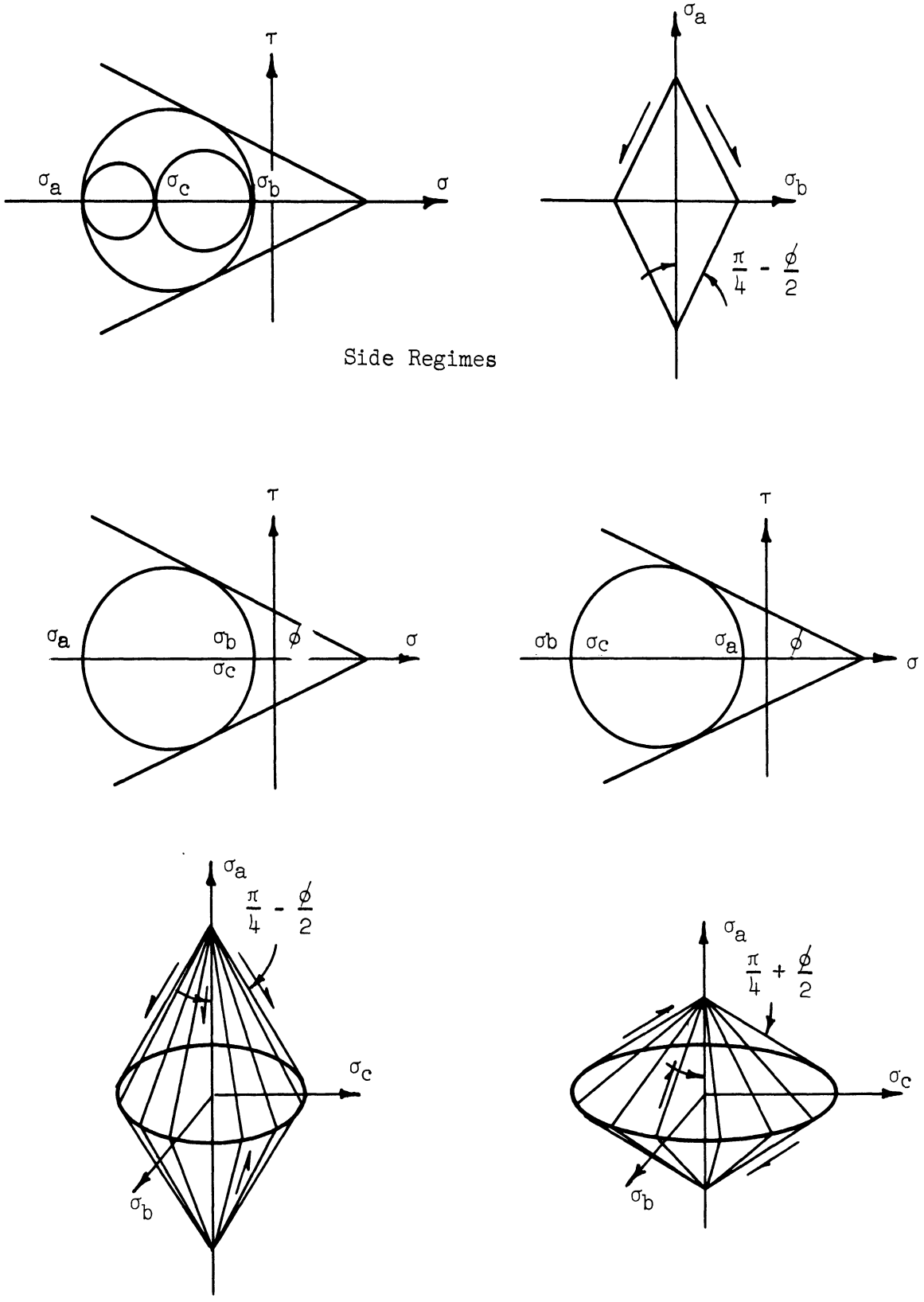

Figure 3-1. Mohr's circle representation and corresponding physical elements for the regimes of the Coulomb yield criterion.

points, one of the principal stresses has a value intermediate to the other two and the critical shear stress occurs on only two planes inclined to the principal stress directions as shown on the element beside the corresponding Mohr's circle. However, for the corner regimes, two of the principal stresses are equal. Hence in the plane of the directions of the two equal stresses, every direction is a principal stress direction. In this case the critical shear stress occurs on all planes tangent to the cone which has the unequal stress direction for its axis and a half-angle of $\pi/4 + \phi/2$ or $\pi/4 - \phi/2$ for regimes A, E, C, or D, B, F, respectively. This is shown in the physical element below the corresponding Mohr's circle in Figure 3-1.

A. SLIP-EXPANSION MODEL

The model is shown in Figure 3-2. An arbitrary direction is represented by the unit vector $\overline{AB}$ which is at an angle λ from the σ_a-axis and whose projection on the σ_b-σ_c plane forms an angle ξ with the σ_b-axis. The unit vector $\overline{G}$ represents the direction of the critical Coulomb shear stresses acting at point B. It forms an angle ψ with the σ_a-axis, ψ assuming the values $\pi/4 + \phi/2$ or $\pi/4 - \phi/2$ depending on the regime. The vector $\overline{E}$ represents the slip on a plane through point B and it forms an angle of $\psi+\overline{w}\beta$ with the σ_a-axis, where β is the angle of expansion and $\overline{w} = \pm 1$. The sign of $\overline{w}$ is chosen such that positive β is associated with expansion. The projections of both $\overline{G}$ and $\overline{E}$ in the σ_b-σ_c plane subtends an angle of Θ with the σ_b-axis. The

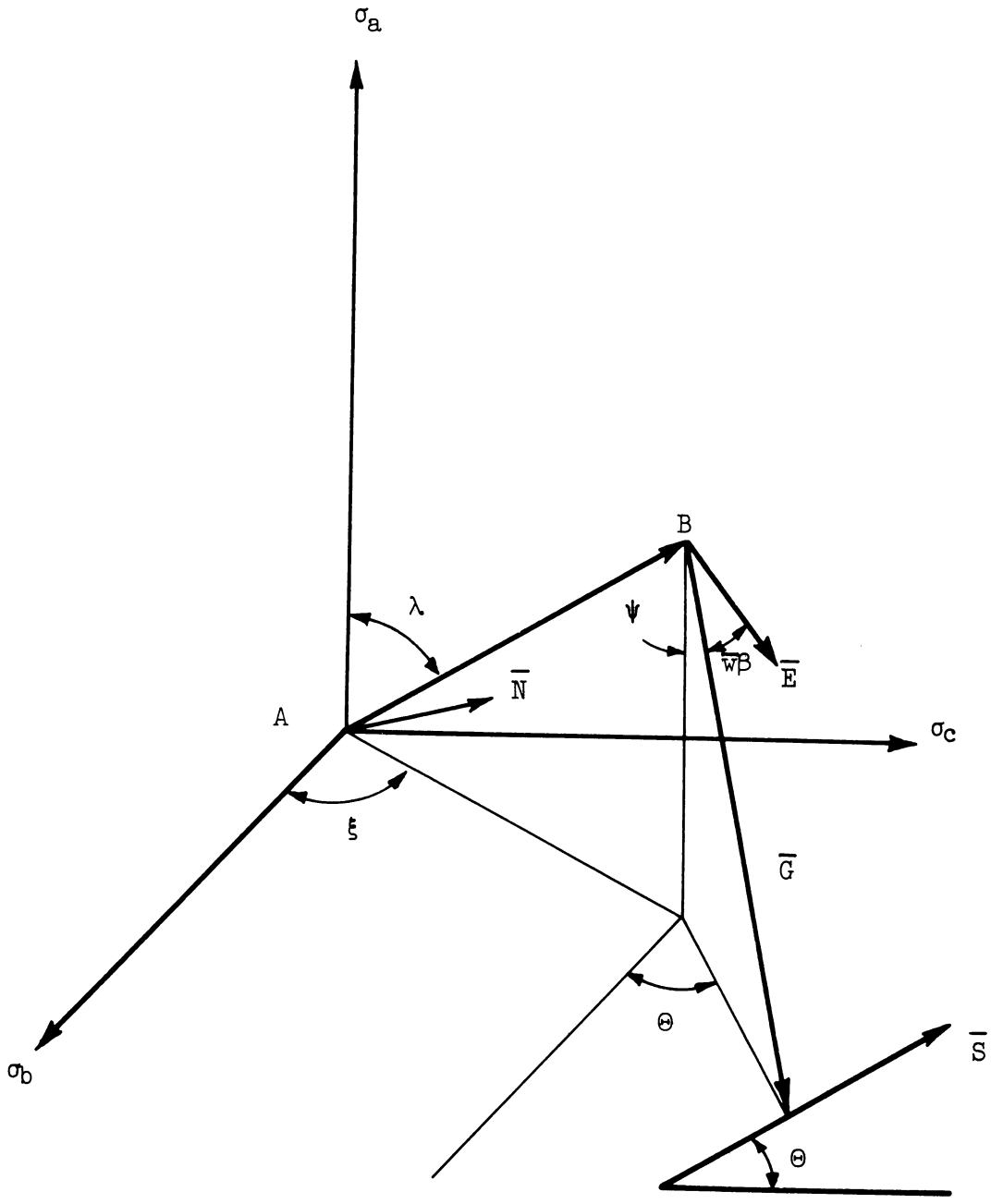

Figure 3-2. The slip-expansion model.

plane of sliding is tangent to the cone which has its vertex at B and has $\bar{G}$ as a generator. Hence, this plane is uniquely determined by vectors $\overline{G}$ and $\bar{S}$, where $\bar{S}$ is the intersection of the slip plane with the σ_b-σ_c plane.

Since the motion is the same over the plane of sliding, the motion of point B with respect to point A varies only with respect to the perpendicular distance from A to the plane of sliding through B. Denoting the absolute value of this variation by "e" and choosing its sign such that the sliding takes place in the same direction as the shear stress on the sliding plane, the slide vector is

$$\bar{E} = \bar{w}e[-\cos(\psi+\bar{w}\beta)\bar{i} + \sin(\psi+\bar{w}\beta)\cos\theta\bar{j} + \sin(\psi+\bar{w}\beta)\sin\theta\,\bar{k}].$$

The state of strain rate at a point in any direction can be completely specified by the extensional strain rate in that direction and by the shearing strain rate between that direction and any two mutually perpendicular directions. Let the line $\overline{AB}$ be the general direction and let $\bar{N}$ be the unit normal to the plane of slip. These can be represented by the vectors

$$\overline{AB} = \cos\lambda\bar{i} + \sin\lambda\cos\xi\bar{j} + \sin\lambda\sin\xi\bar{k}$$

$$\bar{N} = \sin\psi\bar{i} + \cos\psi\cos\theta\bar{j} + \cos\psi\sin\epsilon\bar{k}$$

Then using the engineering definition of extensional strain rate

$$\dot{\epsilon} = (\overline{AB}\cdot\bar{N})(\overline{AB}\cdot\bar{E}).$$

Carrying out the specified vector and scalar operations

$$\dot{\epsilon} = \frac{\bar{w}e}{2}[\cos^2(\xi-\theta)\sin^2\lambda(\sin(2\psi+\bar{w}\beta)+\sin\bar{w}\beta) \tag{3.1}$$

$$- \cos(\xi-\theta)\sin2\lambda\cos(2\psi+\bar{w}\beta)-\cos^2\lambda(\sin(2\psi+\bar{w}\beta)-\sin\bar{w}\beta)]$$

Denote the shearing strain rate of $\overline{AB}$ and another line perpendicular to it and in the plane of $\overline{AB}$ and the σ_a-axis as $\dot{\gamma}_\lambda$ (Figure 3-3). Let $\overline{DB}$ be a unit vector in this plane and let it be perpendicular to $\overline{AB}$, then the rotation rate of $\overline{AB}$ in the positive λ direction is

$$\dot{\omega}_\lambda = (\overline{AB}\cdot\bar{N})(\overline{DB}\cdot\bar{E})$$

where

$$\overline{DB} = -\sin\lambda\bar{i} + \cos\lambda\cos\xi\bar{j} + \cos\lambda\sin\xi\bar{k}$$

Hence, calling positive shearing strain rate

$$\dot{\gamma}_\lambda = \dot{\omega}_\lambda - \dot{\omega}_{\lambda+\pi/2} \tag{3.2}$$

then this shearing strain rate is

$$\dot{\gamma}_\lambda = \frac{\bar{w}e}{2}[-\cos(\xi-\theta)\cos(2\psi+\bar{w}\beta)\cos2\lambda + \cos^2(\xi-\theta)\sin2\lambda(\sin(2\psi+\bar{w}\beta)+\sin\bar{w}\beta) \tag{3.3}$$

$$+ \sin2\lambda(\sin(2\psi+\bar{w}\beta)-\sin\bar{w}\beta)]$$

Denoting the shearing strain rate of $\overline{AB}$ and a third line normal to $\overline{AB}$ and to the plane of $\overline{AB}$ and the σ_a-axis as $\dot{\gamma}_\xi$, (Figure 3-4) and letting

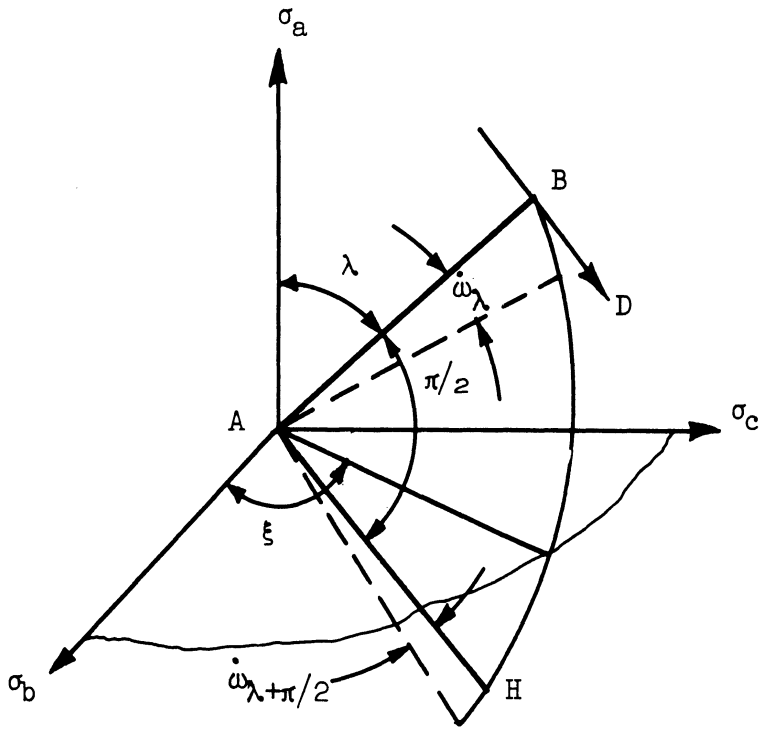

Figure 3-3. Illustration of the shearing strain rate $\dot{\gamma}_\lambda$.

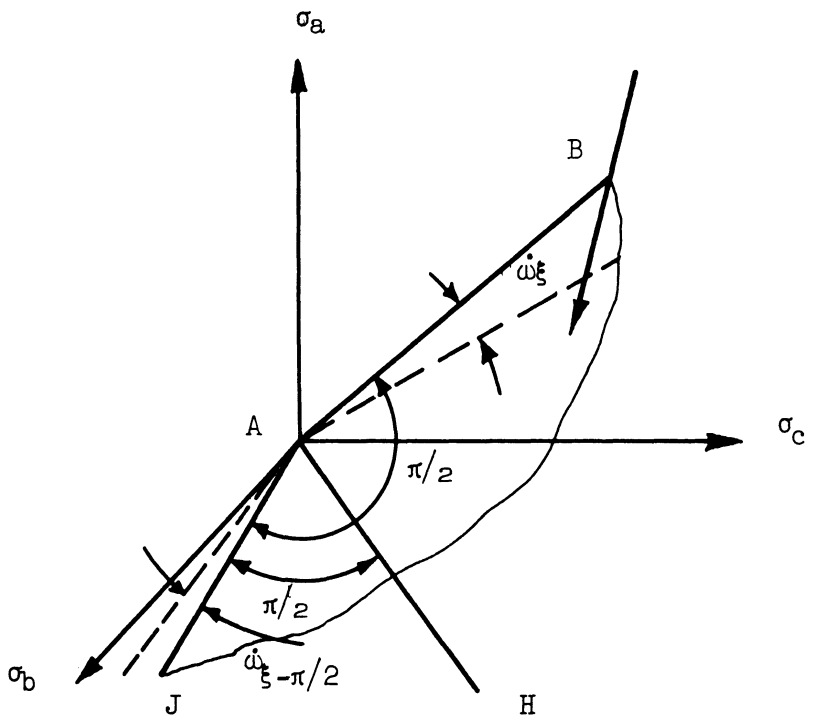

Figure 3-4. Illustration of the shearing strain rate γ_ξ.

$\overline{FB}$ be a unit vector in this plane and normal to $\overline{AB}$ and in the positive ξ direction, then the shearing strain rate in this plane is

$$\dot{\gamma}_{\xi} = (\overline{AB}\cdot\overline{N})(\overline{E}\cdot\overline{FB}) - (\overline{FB}\cdot\overline{N})(-\overline{AB}\cdot\overline{E})$$

where

$$\overline{FB} = 0\overline{i} + \sin\xi\overline{j} - \cos\xi\overline{k}.$$

Upon carrying out the operations, this becomes

$$\dot{\gamma}_{\xi} = -\overline{w}\sin(\xi-\theta)[\cos(2\psi+\overline{w}\beta)\cos\lambda - \cos(\xi-\theta)\sin\lambda(\sin(2\psi+\overline{w}\beta) + \sin\overline{w}\beta)] \tag{3.4}$$

If slip and expansion occur on many planes through point B, which is possible for all stress regimes, then the resultant strain rates can be considered as the sum of the strain rates from all of the slips. They can be expressed

$$\dot{\epsilon} = \frac{1}{2}\sin^2\lambda\sum_{i=0}^{n}\overline{w}e_i\cos^2(\xi-\theta_i)[\sin(2\psi+\overline{w}\beta_i)+\sin\overline{w}\beta_i] \tag{3.5a}$$

$$-\frac{1}{2}\sin2\lambda\sum_{i=0}^{n}\overline{w}e_i\cos(\xi-\theta_i)\cos(2\psi+\overline{w}\beta_i) - \frac{1}{2}\cos^2\lambda\sum_{i=0}^{n}\overline{w}e_i[\sin(2\psi+\overline{w}\beta_i)-\sin\overline{w}\beta_i],$$

where n is any non-negative integer

$$\dot{\gamma}_{\lambda} = -\cos 2\lambda \sum_{i=0}^{n} \overline{w} e_i \cos(\xi-\theta_i)\cos(2\psi+\overline{w}\beta_i) + \frac{1}{2}\sin 2\lambda \sum_{i=0}^{n} \overline{w} e_i [\sin(2\psi+\overline{w}\beta_i)-\sin\overline{w}\beta_i]$$

$$+ \frac{1}{2}\sin 2\lambda \sum_{i=0}^{n} \overline{w} e_i \cos^2(\xi-\theta_i)[\sin(2\psi+\overline{w}\beta_i)+\sin\overline{w}\beta_i], \tag{3.5b}$$

$$\dot{\gamma}_{\xi} = \sin\lambda \sum_{i=0}^{n} \overline{w} e_i \sin(\xi-\theta_i)\cos(\xi-\theta_i)[\sin(2\psi+\overline{w}\beta_i)+\sin\overline{w}\beta_i]$$

$$-\cos\lambda \sum_{i=0}^{n} \overline{w} e_i \sin(\xi-\theta_i)\cos(2\psi+\overline{w}\beta_i). \tag{3.5c}$$

B. FLOW RULES

These results can be specialized to give a rule governing the plastic flow possible for each of the stress regimes.

1. Side Regimes ($\overline{w}$ = +1 from Figure 3.1)

On a side regime of the yield surface slip-expansion can occur on only two planes through B, one at $\theta = 0$, $\psi = \pi/4-\phi/2$ and one at $\theta = \pi$, $\psi = \pi/4-\phi/2$. Thus,

$$\dot{\epsilon} = -\frac{1}{2}(\cos^2\lambda-\cos^2\xi\sin^2\lambda)[e_o\cos(\phi-\beta_o)+e_1\cos(\phi-\beta_1)]$$

$$+ \frac{1}{2}(\sin^2\lambda\cos^2\xi+\cos^2\lambda)(e_o\sin\beta_o+e_1\sin\beta_1) \tag{3.6a}$$

$$-\frac{1}{2}\sin 2\lambda\cos\xi[e_o\sin(\phi-\beta_o)-e_1\sin(\phi-\beta_1)]$$

$$\dot{\gamma}_\lambda = \frac{1}{2}\sin 2\lambda(1+\cos^2\xi)[e_o\cos(\phi-\beta_o)+e_1\cos(\phi-\beta_1)]$$

$$- \frac{1}{2}\sin 2\lambda\sin^2\xi(e_o\sin\beta_o+e_1\sin\beta_1)-\cos 2\lambda\cos\xi[e_o\sin(\phi-\beta_o)-e_1\sin(\phi-\beta_1)], \tag{3.6b}$$

$$\dot{\gamma}_\xi = \frac{1}{2}\sin\lambda\sin 2\xi[e_o(\cos(\phi-\beta_o)+\sin\beta_o)+e_1(\cos(\phi-\beta_1)+\sin\beta_1)]$$

$$-\cos\lambda\sin\xi[e_o\sin(\phi-\beta_o)-e_1\sin(\phi-\beta_1)]. \tag{3.6c}$$

It is clear that $\lambda = \pi/2, -\pi/2, \xi = \pi/2, -\pi/2$ are directions of principal strain rate since $\dot{\gamma}_\lambda = \dot{\gamma}_\xi = 0$ at these values. Furthermore $\dot{\epsilon} = 0$ in the direction, therefore this type of slip and expansion gives plane strain deformation which is the case de Gosselin de Jong considered. The other directions of principal strain rate are $\xi = 0, \pi$ and values of λ equal to

$$\alpha = \frac{1}{2}\tan^{-1}\left[\frac{e_o\sin(\phi-\beta_o)-e_1\sin(\phi-\beta_1)}{e_o\cos(\phi-\beta_o)+e_1\cos(\phi-\beta_1)}\right] \tag{3.7}$$

For simplicity in discussing the results, it will be assumed that β_i is restricted within the practical limits of

$$-\phi/2 \leq \beta_i \leq \phi, \tag{3.8a}$$

and that the angle of friction ϕ is bracketed by

$$0 \leq \phi \leq \pi/4. \tag{3.8b}$$

Then from Eq. (3.7) it can be seen that α, the angle of deviation of the direction of principal strain rate from the direction of principal stress, is limited within the range

$$-\frac{1}{2}(\phi-\beta_1) \leq \alpha \leq \frac{1}{2}(\phi-\beta_o). \tag{3.9}$$

From Eq. (3.6a) the strain rates in the principal stress directions are

$$\dot{\epsilon}_{bb} = \frac{1}{2}[e_o\cos(\phi-\beta_o)+e_1\cos(\phi-\beta_1)] + \frac{1}{2}[e_o\sin\beta_o+e_1\sin\beta_1] \tag{3.10a}$$

$$\dot{\epsilon}_{aa} = -\frac{1}{2}[e_o\cos(\phi-\beta_o)+e_1\cos(\phi-\beta_1)] + \frac{1}{2}[e_o\sin\beta_o+e_1\sin\beta_1] \tag{3.10b}$$

The ratio between these two strain rates is independent of the individual slips only if $\beta_o = \beta_1$. It will be assumed that this is the case. Therefore, the flow rule can be written

$$\frac{\dot{\epsilon}_{bb}}{\dot{\epsilon}_{aa}} = -\frac{\cos(\phi-\beta)+\sin\beta}{\cos(\phi-\beta)-\sin\beta} = -\Omega, \quad \dot{\epsilon}_{bb} \geq 0, \quad \dot{\epsilon}_{aa} \leq 0 \tag{3.11}$$

Since Ω is assumed to be independent of the actual slips its value can be determined from any plane strain test in which the ratio between the strain rates in the principal stress directions are observed.

This plane strain flow rule contains several other flow rules of particular note as special cases. For the simple Coulomb glide case,

the expansion rate is zero. Hence $\beta = 0$, and the above results become

$$-\frac{\phi}{2} \leq \alpha \leq \frac{\phi}{2}, \quad \frac{\dot{\epsilon}_b}{\dot{\epsilon}_a} = -1, \quad \dot{\epsilon}_b \geq 0, \text{ and } \dot{\epsilon}_a \leq 0,$$

where $\dot{\epsilon}_a$ and $\dot{\epsilon}_b$ are principal strain rates. Note that principal strain rates can be used in this case since the slip model indicates that their ratio is independent of the individual slips. In the case where $\phi = 0$, the above results show that the principal directions necessarily coincide. When $\beta = \phi$, Eq. (3.9) shows coincidence to be necessary and Eq. (3.11) becomes

$$\frac{\dot{\epsilon}_b}{\dot{\epsilon}_a} = -\tan^2(\pi/4 + \phi/2), \quad \dot{\epsilon}_b \geq 0, \quad \dot{\epsilon}_a \leq 0$$

which is the perfect plasticity flow rule for a material obeying the Coulomb criterion.

2. Corner Regimes

From Figure 3-1, $\bar{w} = +1$ for regimes D, B, and F. For these stress states it is possible for slip and expansion to occur on infinitely many planes through B, all at $\psi = \pi/4 - \phi/2$. The strain rates from Eq. (3.5) become

$$\dot{\epsilon} = \frac{1}{2}\sin^2\lambda\sum_{i=0}^{n} e_i\cos^2(\xi-\theta_i)[\cos(\phi-\beta_i)+\sin\beta_i]$$

$$- \frac{1}{2}\cos^2\lambda\sum_{i=0}^{n} e_i[\cos(\phi-\beta_i)-\sin\beta_i] - \frac{1}{2}\sin 2\lambda\sum_{i=0}^{n} e_i\cos(\xi-\theta_i)\sin(\phi-\beta_i), \tag{3.12a}$$

$$\dot{\gamma}_\lambda = -\cos 2\lambda\sum_{i=0}^{n} e_i\cos(\xi-\theta_i)\sin(\phi-\beta_i) + \frac{1}{2}\sin 2\lambda\sum_{i=0}^{n} e_i[\cos(\phi-\beta_i)-\sin\beta_i]$$

$$+ \frac{1}{2}\sin 2\lambda\sum_{i=0}^{n} e_i\cos^2(\xi-\theta_i)[\cos(\phi-\beta_i)+\sin\beta_i], \tag{3.12b}$$

$$\dot{\gamma}_\xi = -\cos\lambda\sum_{i=0}^{n} e_i\sin(\xi-\theta_i)\sin(\phi-\beta_i)$$

$$+\sin\lambda\sum_{i=0}^{n} e_i\sin(\xi-\theta_i)\cos(\xi-\theta_i)[\cos(\phi-\beta_i)+\sin\beta_i]. \tag{3.12c}$$

For regimes A, E, and C, $\bar{w} = -1$ by Figure 3-1. The stresses at these regimes are such that slip and expansion is possible on an infinity of planes through B, all at $\psi = \pi/4+\phi/2$. Hence from Eq. (3.5)

$$\dot{\epsilon} = -\frac{1}{2}\sin^2\lambda\sum_{i=0}^{n} e_i\cos^2(\xi-\theta_i)[\cos(\phi-\beta_i)-\sin\beta_i]$$

$$+ \frac{1}{2}\cos^2\lambda\sum_{i=0}^{n} e_i[\cos(\phi-\beta_i)+\sin\beta_i] - \frac{1}{2}\sin 2\lambda\sum_{i=0}^{n} e_i\cos(\xi-\theta_i)\sin(\phi-\beta_i), \tag{3.13a}$$

$$\dot{\gamma}_{\lambda} = -\cos 2\lambda \sum_{i=0}^{n} e_i \cos(\xi-\Theta_i)\sin(\phi-\beta_i) - \frac{1}{2}\sin 2\lambda \sum_{i=0}^{n} e_i[\cos(\phi-\beta_i)+\sin\beta_i] \tag{3.13b}$$

$$- \frac{1}{2}\sin 2\lambda \sum_{i=0}^{n} e_i \cos^2(\xi-\Theta_i)[\cos(\phi-\beta_i)-\sin\beta_i],$$

$$\dot{\gamma}_{\xi} = -\cos\lambda \sum_{i=0}^{n} e_i \sin(\xi-\Theta_i)\sin(\phi-\beta_i) - \sin\lambda \sum_{i=0}^{n} e_i \sin(\xi-\Theta_i)\cos(\xi-\Theta_i)[\cos(\phi-\beta_i)-\sin\beta_i] \tag{3.13c}$$

The components of strain rate for the principal stress directions for regimes D, B, and F are,

$$\dot{\epsilon}_{aa} = -\frac{1}{2}\sum_{i=0}^{n} e_i[\cos(\phi-\beta_i)-\sin\beta_i], \tag{3.14a}$$

$$\dot{\epsilon}_{bb} = \frac{1}{2}\sum_{i=0}^{n} e_i \cos^2\Theta_i[\cos(\phi-\beta_i)+\sin\beta_i] \tag{3.14b}$$

$$\dot{\epsilon}_{cc} = \frac{1}{2}\sum_{i=0}^{n} e_i \sin^2\Theta_i[\cos(\phi-\beta_i)+\sin\beta_i] \tag{3.14c}$$

$$\dot{\gamma}_{ac} = -\sum_{i=0}^{n} e_i \sin\Theta_i \sin(\phi-\beta_i), \tag{3.14d}$$

$$\dot{\gamma}_{cb} = \sum_{i=0}^{n} e_i \sin\Theta_i \cos\Theta_i[\cos(\phi-\beta_i)+\sin\beta_i] \tag{3.14e}$$

$$\dot{\gamma}_{ab} = -\sum_{i=0}^{n} e_i \cos\Theta_i \sin(\phi-\beta_i), \tag{3.14f}$$

and for regimes A, E, and C are,

$$\dot{\epsilon}_{aa} = \frac{1}{2}\sum_{i=0}^{n} e_i[\cos(\phi-\beta_i)+\sin\beta_i], \tag{3.15a}$$

$$\dot{\epsilon}_{bb} = -\frac{1}{2}\sum_{i=0}^{n} e_i\cos^2\theta_i[\cos(\phi-\beta_i)-\sin\beta_i], \tag{3.15b}$$

$$\dot{\epsilon}_{cc} = -\frac{1}{2}\sum_{i=0}^{n} e_i\sin^2\theta_i[\cos(\phi-\beta_i)-\sin\beta_i], \tag{3.15c}$$

$$\dot{\gamma}_{ac} = -\sum_{i=0}^{n} e_i\sin\theta_i\sin(\phi-\beta_i), \tag{3.15d}$$

$$\dot{\gamma}_{cb} = -\sum_{i=0}^{n} e_i\sin\theta_i\cos\theta_i[\cos(\phi-\beta_i)-\sin\beta_i], \tag{3.15e}$$

$$\dot{\gamma}_{ab} = -\sum_{i=0}^{n} e_i\cos\theta_i\sin(\phi-\beta_i). \tag{3.15f}$$

It can be seen that the strain rates in any direction for any of these six regimes can be written as

$$\begin{aligned}\dot{\epsilon} = {} & \sin^2\lambda(\cos^2\xi\ \dot{\epsilon}_{bb} + \frac{1}{2}\sin2\xi\ \dot{\gamma}_{cb} + \sin^2\xi\ \dot{\epsilon}_{cc}) \\ & + \cos^2\lambda\ \dot{\epsilon}_{aa} + \frac{1}{2}\sin2\lambda(\cos\xi\ \dot{\gamma}_{ab} + \sin\xi\ \dot{\gamma}_{ac}),\end{aligned} \tag{3.16a}$$

$$\begin{aligned}\dot{\gamma}_{\lambda} = {} & \sin2\lambda(-\dot{\epsilon}_{aa} + \cos^2\xi\ \dot{\epsilon}_{bb} + \frac{1}{2}\sin2\xi\ \dot{\gamma}_{cb} + \sin^2\xi\ \dot{\epsilon}_{cc}) \\ & + \cos2\lambda(\cos\xi\ \dot{\gamma}_{ab} + \sin\xi\ \dot{\gamma}_{ac}),\end{aligned} \tag{3.16b}$$

$$\dot{\gamma}_{\xi} = \sin\lambda[\sin2\xi(\dot{\epsilon}_{bb}-\dot{\epsilon}_{cc})- \cos2\xi\ \dot{\gamma}_{cb}] + \cos\lambda[\sin\xi\ \dot{\gamma}_{ab}-\cos\xi\ \dot{\gamma}_{ac}]. \tag{3.16c}$$

If the deformations at the corner stress regimes are specialized to the case of axial symmetry, then the circumferential direction is a principal strain rate direction by definition. Let the σ_3 axis be the circumferential direction, then for regimes F, D, and A, C, the circumferential stress is one of the equal stresses. Then axial symmetry requires that

$$\dot{\gamma}_{ab} = \dot{\gamma}_{cb} = 0.$$

From Eqs. (3.14e), (3.14f), (3.15e), and (3.15f), it can be seen that this can be satisfied by an infinite variety of slips and expansions.

The directions of principal strain rate are those directions in which axial strain rates alone occur. A line in such a direction has no shearing strain rate with any line perpendicular to it. Such a condition can be assured by equating to zero the shearing strain rate between this line and any two other lines perpendicular to it and noncolinear with each other. Thus the principal directions can be found by finding the angles λ and ξ where

$$\dot{\gamma}_{\lambda} = \dot{\gamma}_{\xi} = 0.$$

Imposing axial symmetry on Eqs. (3.16b) and (3.16c), this means that

$$\sin\lambda \sin2\xi(\dot{\epsilon}_{bb}-\dot{\epsilon}_{cc}) - \cos\lambda \cos\xi \dot{\gamma}_{ab} = 0, \qquad (3.17a)$$

$$\sin2\lambda(\cos^2\xi \dot{\epsilon}_{bb}+\sin^2\xi \dot{\epsilon}_{cc}-\dot{\epsilon}_{aa}) + \cos2\lambda \sin\xi \dot{\gamma}_{ac} = 0. \qquad (3.17b)$$

The only significant roots to these equations are $\xi = \pi/2$ and values of λ equal to

$$\alpha = \frac{1}{2}\tan^{-1}\left(\frac{\dot{\gamma}_{ac}}{\dot{\epsilon}_{aa}-\dot{\epsilon}_{cc}}\right). \tag{3.18}$$

Substituting the strain rates in terms of the slips and expansions into Eq. (3.18) for regimes D and F gives

$$\alpha = \frac{1}{2}\tan^{-1}\left[\frac{2\Sigma e_i \sin\Theta_i \sin(\phi-\beta_i)}{\Sigma e_i[\cos(\phi-\beta_i)-\sin\beta_i]+\Sigma e_i \sin^2\Theta_i[\cos(\phi-\beta_i)+\sin\beta_i]}\right] \tag{3.19a}$$

and for regimes A and C gives

$$\alpha = \frac{1}{2}\tan^{-1}\left[\frac{-2\Sigma e_i \sin\Theta_i \sin(\phi-\beta_i)}{\Sigma e_i[\cos(\phi-\beta_i)+\sin\beta_i]+\Sigma e_i \sin^2\Theta_i[\cos(\phi-\beta_i)-\sin\beta_i]}\right] \tag{3.19b}$$

This angle of deviation of the directions of principal stress and strain rate, α, assumes its largest positive and negative values when slip is occuring on only one plane described by either $\Theta = \pi/2$ or $\Theta = -\pi/2$. Therefore α is limited by

$$-\frac{1}{2}(\phi-\beta_0) \leq \alpha \leq \frac{1}{2}(\phi-\beta_1), \tag{3.20}$$

where β_0 or β_1 is that expansion angle acting on the single plane of

sliding that gives the maximum positive or negative deviations. Note that the upper and lower limits on α are realized only when a plane strain velocity field is occurring. However, these limiting values can be approached without the plane strain case actually being realized.

For regimes B and E, the unequal stress direction is the circumferential direction. Therefore, the σ_a-axis is the circumferential direction and axial symmetry requires that

$$\dot{\gamma}_{ac} = \dot{\gamma}_{ab} = 0.$$

The other two principal strain rate directions lie in the plane of σ_b and σ_c. Since every direction in the σ_b-σ_c plane is a principal stress direction, the relationship between the principal stress and strain rate directions in this plane is not definite.

Since it is possible for slip and expansion to occur in a completely arbitrary manner on any or all of the critical shear planes, the flow rule for the corner regimes has a good deal of freedom. Again, it should be noted that it is necessary that all the expansion angles β_i be equal in order for any relationship between the strain rates to be independent of the individual slips. It will be assumed that this is the case. Then take the strain rates for regimes D and F as an example. From Eqs. (3.14) it can be seen that

$$0 \geq \frac{\dot{\epsilon}_\Theta}{\dot{\epsilon}_{aa}} \geq -\Omega, \quad 0 \geq \frac{\dot{\epsilon}_{cc}}{\dot{\epsilon}_{aa}} \geq -\Omega, \quad \dot{\epsilon}_{aa} \leq 0, \quad \dot{\epsilon}_{cc} \geq 0, \text{ and } \dot{\epsilon}_\Theta \geq 0. \tag{3.21a}$$

The only relationship independent of the individual slips is

$$\frac{\dot{\epsilon}_{\theta}+\dot{\epsilon}_{cc}}{\dot{\epsilon}_{aa}} = -\frac{\cos(\phi-\beta)+\sin\beta}{\cos(\phi-\beta)-\sin\beta} = -\Omega \qquad (3.21b)$$

Equations (3.21) are a complete statement of the flow rule for regimes D and F. Similarly, from Eqs. (3.15) it can be seen that

$$0 \geq \frac{\dot{\epsilon}_{\theta}}{\dot{\epsilon}_{aa}} \geq -\Omega^{-1}, \quad 0 \geq \frac{\dot{\epsilon}_{cc}}{\dot{\epsilon}_{aa}} \geq -\Omega^{-1}, \quad \dot{\epsilon}_{aa} \geq 0, \quad \dot{\epsilon}_{cc} \leq 0, \quad \dot{\epsilon}_{\theta} \leq 0 \qquad (3.22a)$$

for regimes A and C, and that

$$\frac{\dot{\epsilon}_{\theta}+\dot{\epsilon}_{cc}}{\dot{\epsilon}_{aa}} = -\frac{\cos(\phi-\beta)-\sin\beta}{\cos(\phi-\beta)+\sin\beta} = -\Omega^{-1} \qquad (3.22b)$$

For regimes B and E, $\dot{\epsilon}_{aa}$ corresponds to $\dot{\epsilon}_{\theta}$ and any of the strain rates in the σ_b-σ_c plane are principal strain rates. Therefore, from Eqs. (3.14) the flow rule for regime B is

$$0 \geq \frac{\dot{\epsilon}_b}{\dot{\epsilon}_{\theta}} \geq -\Omega, \quad 0 \geq \frac{\dot{\epsilon}_c}{\dot{\epsilon}_{\theta}} \geq -\Omega, \quad \epsilon_b \geq 0, \quad \epsilon_c \geq 0, \quad \epsilon_{\theta} \leq 0, \qquad (3.23a)$$

and

$$\frac{\dot{\epsilon}_c+\dot{\epsilon}_b}{\dot{\epsilon}_{\theta}} = -\Omega, \qquad (3.23b)$$

and from Eqs. (3.15), the flow rule for regime E is given by

$$0 \geq \frac{\dot{\epsilon}_b}{\dot{\epsilon}_{\theta}} \geq -\Omega^{-1}, \quad 0 \geq \frac{\dot{\epsilon}_c}{\dot{\epsilon}_{\theta}} \geq -\Omega^{-1}, \quad \dot{\epsilon}_b \leq 0, \quad \dot{\epsilon}_c \leq 0, \quad \dot{\epsilon}_{\theta} \geq 0, \qquad (3.24a)$$

and

$$\frac{\dot{\epsilon}_c+\dot{\epsilon}_b}{\dot{\epsilon}_\theta} = -\Omega^{-1}. \tag{3.24b}$$

Since the dilatation rate parameter Ω is assumed to be independent of the particular slips occurring, then its value at a certain instant can be determined from any test for which the appropriate regime is known. The observations necessary are merely the volume change rate and the appropriate axial strain rate.

These results can be specialized to give some flow rules of particular note. The Coulomb glide case discussed by Haythornthwaite[29] is obtained by setting $\beta = 0$. The limitation on the possible deviation of the principal stress and strain rate directions changes to

$$-\phi/2 \leq \alpha \leq +\phi/2, \tag{3.25}$$

and the dilatation rate is zero, hence the parameter

$$\Omega = 1. \tag{3.26}$$

If in addition the material is insensitive to hydrostatic pressure, i.e., $\phi = 0$, then $\alpha = 0$ from Eq. (3.25). Hence the directions of principal stress and strain rate coincide and the flow rule is identical with the flow rule associated with the Tresca yield condition. The special case where $\beta = \phi$ gives the perfect plasticity case since Eq. (3.20) shows the deviation to be necessarily zero and since

$$\Omega = \tan^2(\pi/4 + \phi/2). \tag{3.27}$$

The regimes of the yield surface and the associated axially symmetric flow rule can be separated into four groups. Assuming $\sigma_1 \geq \sigma_2$ they are as follows:

(I) At B $\sigma_1 = \sigma_2, \quad \sigma_\theta = \sigma_1 N^2 - 2cN$ (3.31a)

$$\dot{\epsilon}_1 \geq 0, \quad \dot{\epsilon}_2 \geq 0, \quad \dot{\epsilon}_\theta \leq 0, \quad \dot{\epsilon}_1 + \dot{\epsilon}_2 + \Omega\, \dot{\epsilon}_\theta = 0 \tag{3.31b}$$

At E $\sigma_1 = \sigma_2 = \sigma_\theta N^2 - 2cN$ (3.32a)

$$\dot{\epsilon}_1 \leq 0, \quad \dot{\epsilon}_2 \leq 0, \quad \dot{\epsilon}_\theta \geq 0, \quad \dot{\epsilon}_1 + \dot{\epsilon}_2 + \Omega^{-1}\, \dot{\epsilon}_\theta = 0 \tag{3.32b}$$

(II) On AB $\sigma_1 N^2 - \sigma_\theta = 2cN, \quad \sigma_1 > \sigma_2 > \sigma_\theta$ (3.33a)

$$\dot{\epsilon}_1 \geq 0, \quad \dot{\epsilon}_2 = 0, \quad \dot{\epsilon}_\theta \leq 0, \quad \dot{\epsilon}_1 + \Omega\, \dot{\epsilon}_\theta = 0 \tag{3.33b}$$

On EF $\sigma_\theta N^2 - \sigma_2 = 2cN, \quad \sigma_\theta > \sigma_1 > \sigma_2$ (3.34a)

$$\dot{\epsilon}_1 = 0, \quad \dot{\epsilon}_2 \leq 0, \quad \dot{\epsilon}_\theta \geq 0, \quad \Omega\dot{\epsilon}_2 + \dot{\epsilon}_\theta = 0 \tag{3.34b}$$

The directions of stress and strain rate necessarily coincide for this group since the zero strain direction is a principal stress and principal strain rate direction by the plane strain condition and the circumferential direction is a principal stress and principal strain rate direction from axial symmetry.

(III) On AF $\sigma_1 N^2 - \sigma_2 = 2cN, \quad \sigma_1 > \sigma_\theta > \sigma_2$ (3.35a)

$$\dot{\epsilon}_{11} \geq 0, \quad \dot{\epsilon}_{22} \leq 0, \quad \dot{\epsilon}_\theta = 0, \quad \dot{\epsilon}_{11} + \Omega\, \dot{\epsilon}_{22} = 0 \tag{3.35b}$$

For this group the circumferential direction is also the zero strain rate direction, hence the other two directions of principal stress and strain rate do not nesessarily coincide by Eq. (3.7), and the deviation is bracketed by Eq. (3.9)

$$\text{(IV)}\quad \text{At F}\quad \sigma_1 = \sigma_\theta, \quad \sigma_2 = \sigma_1 N^2 - 2cN \tag{3.36a}$$

$$\dot{\epsilon}_{11} \geq 0, \quad \dot{\epsilon}_{22} \leq 0, \quad \dot{\epsilon}_\theta \geq 0, \quad \dot{\epsilon}_{11} + \Omega\, \dot{\epsilon}_{22} + \dot{\epsilon}_\theta = 0 \tag{3.36b}$$

$$\text{At A}\quad \sigma_2 = \sigma_\theta = \sigma_1 N^2 - 2cN \tag{3.37a}$$

$$\dot{\epsilon}_{11} \geq 0, \quad \dot{\epsilon}_{22} \leq 0, \quad \dot{\epsilon}_\theta \leq 0, \quad \Omega^{-1}\, \dot{\epsilon}_{11} + \dot{\epsilon}_{22} + \dot{\epsilon}_\theta = 0 \tag{3.37b}$$

By Eq. (3.9) the $\dot{\epsilon}_1$ and $\dot{\epsilon}_2$ directions do not necessarily coincide with the σ_1 and σ_2 directions, and the deviations are limited by Eq. (3.20).

CHAPTER IV

ANALYSIS OF THE FIELD EQUATIONS

An analysis of the stress and velocity equations and solutions for both plane strain and axial symmetry will be presented herein. Although the plane strain case has been treated in much detail by de Jong,[28] it is included here to show the effects of a dilatation rate on the velocity field. The axial symmetry problem will involve the investigation of all of the differing regimes of the Coulomb yield surface. Similar investigations of the axial symmetry case have been performed by Shield[34] for perfectly plastic materials yielding according to the Tresca criterion and by Cox, Eason, and Hopkins[20] for perfectly plastic materials obeying the Coulomb criterion.

The analysis of the stress fields will be limited to considerations of quasi-static conditions. In addition, the effects of granular material weight will be included where possible. Therefore for the axial symmetry case, it will be required that the stresses satisfy the equations of equilibrium

$$\frac{\partial \sigma_r}{\partial r} + \frac{\partial \tau_{zr}}{\partial z} + \frac{\sigma_r - \sigma_\theta}{r} = 0, \qquad (4.1a)$$

$$\frac{\partial \tau_{zr}}{\partial r} + \frac{\partial \sigma_z}{\partial z} + \frac{\tau_{zr}}{r} + \gamma = 0, \qquad (4.1b)$$

where γ is the weight density of the granular material.

Assuming the velocity field is axially symmetric when the stress field is axially symmetric, the velocity-strain rate relations are

$$\dot{\epsilon}_r = \frac{\partial u}{\partial r}, \quad \dot{\epsilon}_z = \frac{\partial w}{\partial z}, \quad \dot{\epsilon}_\theta = \frac{u}{r}, \quad \dot{\gamma}_{rz} = \frac{\partial u}{\partial z} + \frac{\partial w}{\partial r}, \qquad (4.2)$$

where u and w are the radial and axial velocity components, respectively. Likewise the plane strain velocity-strain rate relations are given by

$$\dot{\epsilon}_x = \frac{\partial u}{\partial x}, \quad \dot{\epsilon}_y = \frac{\partial v}{\partial y}, \quad \dot{\gamma}_{xy} = \frac{\partial u}{\partial y} + \frac{\partial v}{\partial x}, \qquad (4.3)$$

where u and v are the velocity components in the x and y directions.

A. PLANE STRAIN

For the case of plane strain, the stress field is hyperbolic. The stress characteristics are the planes of critical Coulomb shear stress as shown in Figure 4-1. The equations governing the stress field are the well known Kötter equations (see Hill[27] or Sokolovski[35]). These will not be discussed; instead attention will be restricted to the velocity equations.

The plane strain flow rule Eq. (3.7) and Eq. (3.11) is shown in Figures 4-2 and 4-3. Introducing the angle ν as the angle between the σ_2 direction and the x-axis, then the two independent relationships between the strain rates can be written as

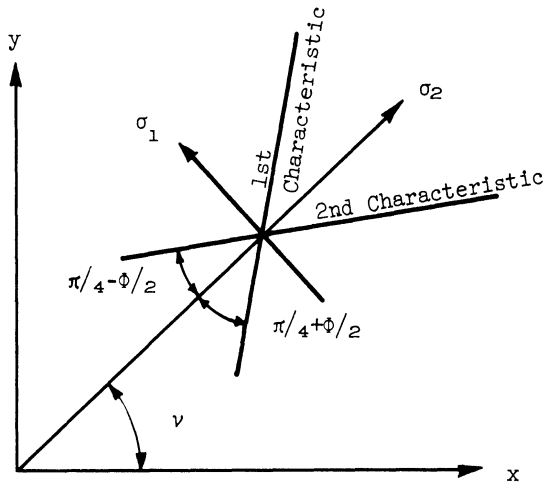

Figure 4-1. Stress characteristics and principal stress directions for plane strain conditions.

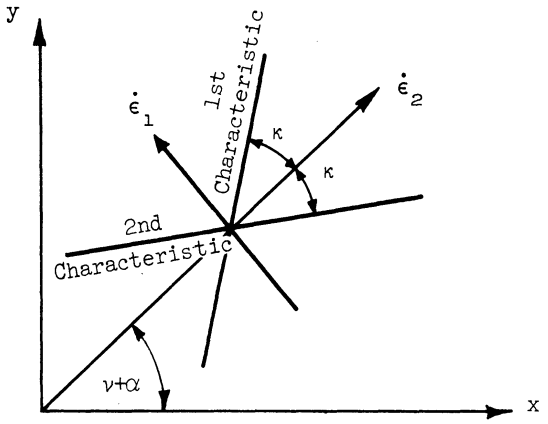

Figure 4-2. Velocity characteristics and principal strain rate directions for plane strain conditions.

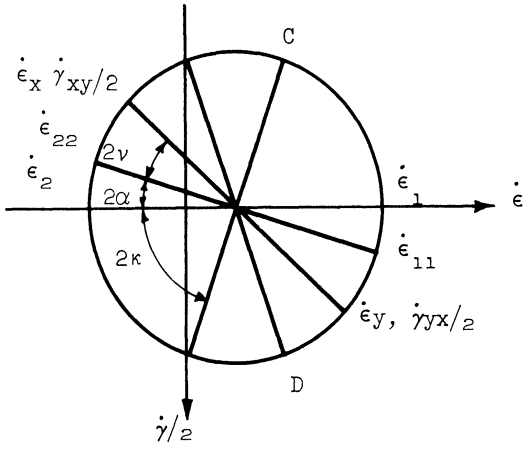

Figure 4-3. Mohr's circle for strain rates for plane strain conditions.

$$\frac{\dot{\gamma}_{xy}}{\dot{\epsilon}_x - \dot{\epsilon}_y} = \tan 2(\alpha+\nu) \tag{4.4a}$$

$$\dot{\epsilon}_x - \dot{\epsilon}_y \tan(\nu+\alpha+\kappa)\tan(\nu+\alpha-\kappa) = 0 \tag{4.4b}$$

where κ is the first quadrant solution of

$$\cos 2\kappa = \frac{\Omega-1}{\Omega+1}\cos 2\alpha = \frac{\sin\beta \cos 2\alpha}{\cos(\phi-\beta)}. \tag{4.4c}$$

The velocity field described by these two equations is hyperbolic. The characteristics are given by

$$\frac{dy}{dx} = \tan(\nu+\alpha+\kappa); \quad \tan(\nu+\alpha-\kappa). \tag{4.5}$$

From Figure 4-3 it can be seen that these are the zero extensional strain rate directions, hence the characteristics are inextensible. The relationship of the velocity characteristics to the stress characteristics depends on e_o, e_1, and β. For the case of perfect plasticity $\beta = \phi$, $\alpha = 0$ and from Eq. (4.4c) $\kappa = \pi/4-\phi/2$. Comparing Figure 4-1 and Figure 4-2 it can be seen that both sets of velocity and stress characteristics coincide. For expansion angles less than ϕ, $\kappa > \pi/4-\phi/2$, and the velocity characteristics will not coincide with the stress characteristics, in general. However, the principal directions can deviate between the limits

$$-\frac{1}{2}(\phi-\beta) \leq \alpha \leq \frac{1}{2}(\phi-\beta).$$

For the lower limit $\kappa = \pi/4-\beta/2$ by Eq. (4.4c), hence the inclination of the first velocity characteristic $\nu+\alpha+\kappa$ becomes

$$\nu + \alpha + \kappa = \nu - \frac{1}{2}(\phi-\beta) + (\pi/4-\beta/2) = \nu + \pi/4 - \phi/2.$$

Comparing Figure 4-1 and Figure 4-2 shows that the first velocity characteristics coincide with the first stress characteristics. Similarly second velocity and stress characteristics coincide for the upper limit. Thus the slip and expansion model allows enough freedom in the principal strain direction such that one set of stress and velocity characteristics can coincide for expansion rates smaller than the perfect plasticity expansion rate.

The velocity discontinuities for plane strain are restricted by the possible strain rates shown in Figure 4-3. From this figure it can be seen that strain rate states corresponding to only normal or to only tangential velocity discontinuities are not permitted for a dilating material. Thus both normal and tangential discontinuities must be occurring simultaneously, implying incipient separation of adjacent particles. As discussed by Shield,[31] this separation requires that the line of discontinuity in the velocity field must be regarded as a thin transition layer.

From geometrical considerations, a tangential velocity discontinuity will create a strain rate state in which the strain rate $\dot{\epsilon}_{tt}$ is negligible compared to the shearing strain rate $\dot{\gamma}_{nt}$ in Figure 4-4.

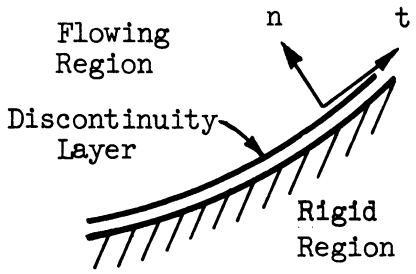

Figure 4-4. Velocity discontinuity for plane strain conditions.

From Figure 4-3, this condition is only satisfied along the velocity characteristics. Therefore, the lines of discontinuity, which are often referred to as "rupture lines," are velocity characteristics. The fact that the rupture lines are frequently observed to be in close coincidence with the computed stress characteristics is good evidence of the deviation of the principal directions.

The shearing strain rate along the discontinuity and the extensional strain normal to the discontinuity are then given by points C or D on Figure 4-3 from which it can be seen that

$$\frac{\dot{\epsilon}_{nn}}{\dot{\gamma}_{nt}} = \cot 2\kappa \qquad (4.6)$$

Writing the strain rates in terms of the velocity jumps V_n and V_t, Eq. (4.6) gives the relationship between the velocity jumps

$$\frac{V_n}{V_t} = \cot 2\kappa \qquad (4.7)$$

B. AXIAL SYMMETRY

1. Group I

Regimes B and E form Group I. In both cases the principal stresses in the r-z plane are equal. Introducing the pure number $\overline{w}$ which has the property

$$\overline{w} = +1 \text{ for regime B}$$

$$-1 \text{ for regime E,}$$

then directly from Eqs. (3.31a) and (3.32a) it can be written that

$$\sigma_1 = \sigma_2 = \sigma_r = \sigma_z, \quad \sigma_\theta = \sigma_r N^{2\overline{w}} - \overline{w} 2cN^{\overline{w}}, \text{ and } \tau_{rz} = 0.$$

The equilibrium Eqs. (4.1) simplify to

$$\frac{\partial \sigma_r}{\partial r} + \frac{\sigma_r - \sigma_\theta}{r} = 0 \text{ and } \frac{\partial \sigma_r}{\partial z} + \gamma = 0.$$

The second of these equations implies

$$\sigma_r = -\gamma z + f(r).$$

Substitution of this equation along with the expression for σ_θ into the first equilibrium equation yields

$$\frac{df}{dr} - (N^{2\overline{w}} - 1)\frac{f}{r} = -\frac{(N^{2\overline{w}} - 1)\gamma z + 2cN^{\overline{w}}\overline{w}}{r}.$$

But no expression for f(r) can satisfy this equation without being a

function of z. Since this violates the definition of f(r), the equilibrium equations do not admit a solution unless $\gamma = 0$. When $\gamma = 0$, the solution is

$$f = C_1 r^{(N^{2\overline{w}}-1)} + \frac{\overline{w}2cN^{\overline{w}}}{N^{2\overline{w}}-1}$$

where C_1 is an arbitrary constant to be evaluated at a boundary. Then the stresses for regime B are,

$$\sigma_r = \sigma_z = C_1 r^{(N^2-1)} + c \cot\phi, \tag{4.9a}$$

$$\sigma_\theta = C_1 N^2 r^{(N^2-1)} + c \cot\phi, \tag{4.9b}$$

$$\tau_{rz} = 0 \tag{4.9c}$$

and for regime E,

$$\sigma_r = \sigma_z = C_1 r^{(N^{-2}-1)} + c \cot\phi, \tag{4.10a}$$

$$\sigma_\theta = C_1 N^{-2} r^{(N^{-2}-1)} + c \cot\phi, \tag{4.10b}$$

$$\tau_{rz} = 0 \tag{4.10c}$$

The principal stress directions are undefined in the meridional plane, hence the velocities are restricted only by the dilatation rule

$$\frac{\partial u}{\partial r} + \frac{\partial w}{\partial z} + \Omega^{\overline{w}} \frac{u}{r} = 0 \tag{4.11a}$$

and by the conditions

$$\bar{w}\,\dot{\epsilon}_\theta \leq 0, \quad \bar{w}\,\dot{\epsilon}_1 \geq 0, \quad \bar{w}\,\dot{\epsilon}_2 \geq 0. \tag{4.11b}$$

2. Group II

The plastic regimes AB and EF of this group are characterized by the vanishing of either one of the principal strain rates in the r-z plane. Let

$$\bar{w} = \begin{cases} +1 \text{ for regime AB} \\ -1 \text{ for regime EF.} \end{cases}$$

Denoting $\dot{\epsilon}_b$ as the zero principal strain rate and $\dot{\epsilon}_a$ as the non-zero principal strain rate the flow rule, Eqs. (3.33b) and (3.34b), can be written

$$\dot{\epsilon}_a = -\Omega\,\bar{w}\dot{\epsilon}_\theta \tag{4.12a}$$

$$\bar{w}\dot{\epsilon}_\theta \leq 0. \tag{4.12b}$$

Introducing ν as the inclination of the $\dot{\epsilon}_a$ direction from the r-axis, then from Figure 4-5 the strain rate components can be written

$$\dot{\epsilon}_{rr} = \dot{\epsilon}_a\cos^2\nu, \quad \dot{\epsilon}_{zz} = \dot{\epsilon}_a\sin^2\nu, \quad \dot{\gamma}_{rz} = \dot{\epsilon}_a\sin 2\nu.$$

Substituting Eqs. (4.12a) and (4.2) into these equations, the velocity field is completely defined by

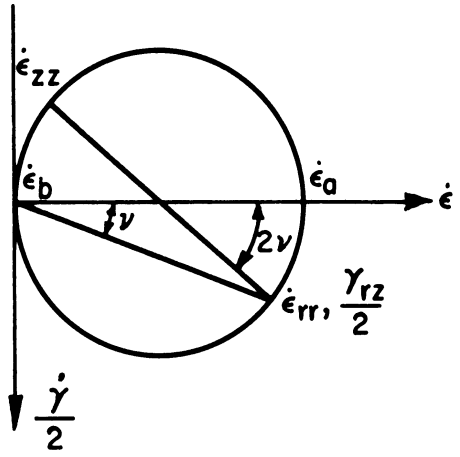

Figure 4-5. Mohr's circle for strain rates of group II.

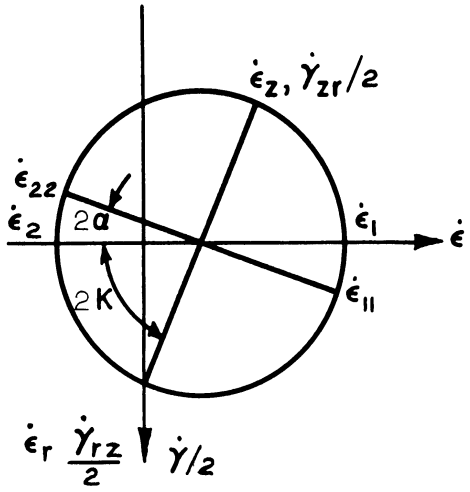

Figure 4-6. Mohr's circle for strain rates of group III.

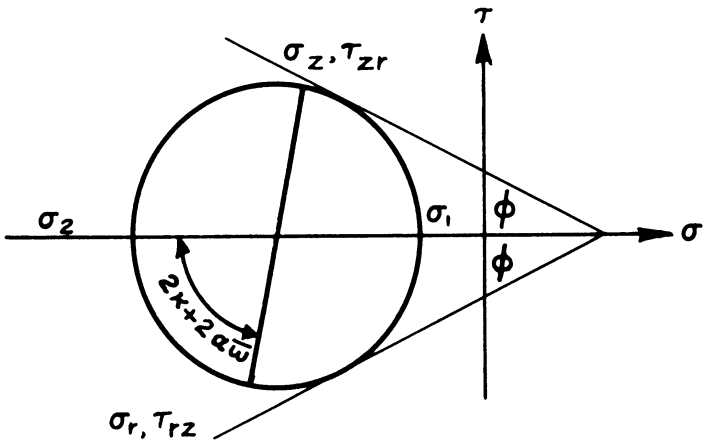

Figure 4-7. Mohr's circle for stress states of group III.

$$\frac{\partial u}{\partial r} + \Omega^{\overline{w}} \frac{u}{r} \cos^2\nu = 0, \tag{4.13a}$$

$$\frac{\partial w}{\partial z} + \Omega^{\overline{w}} \frac{u}{r} \sin^2\nu = 0, \tag{4.13b}$$

$$\frac{\partial u}{\partial z} + \frac{\partial w}{\partial r} + \Omega^{\overline{w}} \frac{u}{r} \sin 2\nu = 0, \tag{4.13c}$$

$$\overline{w}u \leq 0. \tag{4.13d}$$

The velocity field described by Eqs. (4.13) has been shown to be hyperbolic by Cox, Eason, and Hopkins.[20] They found the characteristics to be the principal strain rate directions, i.e.,

$$\frac{dz}{dr} = \tan\nu, \quad \tan(\nu+\pi/2). \tag{4.14}$$

A recent paper by H. Lippmann[36] treats the hyperbolic characteristics of these equations in more detail. For the purposes here, it will just be noted on first characteristics that,

$$\dot{\epsilon}_a = -\Omega^{\overline{w}} \frac{u}{r} \tag{4.15a}$$

and on second characteristics,

$$\dot{\epsilon}_b = 0 \tag{4.15b}$$

After the velocity characteristics have been found, the stress field can be determined from the two equations of equilibrium, the

yield condition, and the condition that the principal axes of stress coincide with the principal axes of strain rate. The slip model analysis has shown that this latter requirement is necessary for these regimes. The yield condition gives the equation

$$\sigma_\theta = \sigma_1 N^2 - 2cN, \quad \sigma_1 > \sigma_2 > \sigma_\theta \text{ for regime AB} \tag{4.16a}$$

$$\sigma_\theta = \sigma_2 N^{-2} + 2cN^{-1}, \sigma_\theta > \sigma_1 > \sigma_2 \text{ for regime EF.} \tag{4.16b}$$

The condition of coincidence of the directions of principal stress and strain rate is satisfied by the cartesian stress components

$$\sigma_r = \frac{1}{2}(\sigma_1+\sigma_2) + \frac{1}{2}(\sigma_1-\sigma_2)\cos 2\nu \tag{4.17a}$$

$$\sigma_z = \frac{1}{2}(\sigma_1+\sigma_2) - \frac{1}{2}(\sigma_1-\sigma_2)\cos 2\nu \tag{4.17b}$$

$$\tau_{zr} = \frac{1}{2}(\sigma_1-\sigma_2)\sin 2\nu \tag{4.17c}$$

Substituting these stress components into the equilibrium equations yields

$$\frac{\partial}{\partial r}\left(\frac{\sigma_1+\sigma_2}{2}\right) + \cos 2\nu \frac{\partial}{\partial r}\left(\frac{\sigma_1-\sigma_2}{2}\right) + \sin 2\nu \frac{\partial}{\partial z}\left(\frac{\sigma_1-\sigma_2}{2}\right)$$

$$+ (\sigma_1-\sigma_2)\left(\cos 2\nu \frac{\partial \nu}{\partial z} - \sin 2\nu \frac{\partial \nu}{\partial r}\right) + \frac{1}{r}\left[\left(\frac{\sigma_1+\sigma_2}{2}\right) + \left(\frac{\sigma_1-\sigma_2}{2}\right)\cos 2\nu - \sigma_\theta\right] = 0 \tag{4.18a}$$

$$\frac{\partial}{\partial z}\left(\frac{\sigma_1+\sigma_2}{2}\right)-\cos 2\nu\ \frac{\partial}{\partial z}\left(\frac{\sigma_1-\sigma_2}{2}\right)+\sin 2\nu\ \frac{\partial}{\partial r}\left(\frac{\sigma_1-\sigma_2}{2}\right)$$

$$+\ (\sigma_1-\sigma_2)\left(\sin 2\nu\ \frac{\partial \nu}{\partial z}+\cos 2\nu\ \frac{\partial \nu}{\partial r}+\frac{1}{2r}\sin 2\nu\right)+\gamma\ =\ 0. \tag{4.18b}$$

The stress field described by Eqs. (4.16) and (4.18) is hyperbolic; the stress characteristics are the same as the velocity characteristics, Eq. (4.14). The equations relating the stresses along the first characteristics are,

$$d(\sigma_1+\sigma_2)+d(\sigma_1-\sigma_2)+\left[(\sigma_1-\sigma_2)\ \frac{\sin 2\nu}{r}+2\gamma\right]dz+\left[(\sigma_1+\sigma_2)+(\sigma_1-\sigma_2)\cos 2\nu-2\sigma_\theta\right]\frac{dr}{r}$$

$$+\ 2(\sigma_1-\sigma_2)\left[\frac{\partial \nu}{\partial z}\,dr-\frac{\partial \nu}{\partial r}\,dz\right]\ =\ 0 \tag{4.19a}$$

and on the second characteristics,

$$d(\sigma_1+\sigma_2)-d(\sigma_1-\sigma_2)+\left[(\sigma_1-\sigma_2)\ \frac{\sin 2\nu}{r}+2\gamma\right]dz+\left[(\sigma_1+\sigma_2)+(\sigma_1-\sigma_2)\cos 2\nu-2\sigma_\theta\right]\frac{dr}{r}$$

$$-\ 2(\sigma_1-\sigma_2)\left[\frac{\partial \nu}{\partial z}\,dr-\frac{\partial \nu}{\partial r}\,dz\right]\ =\ 0 \tag{4.19b}$$

3. Group III

On Side AF, $\dot{\epsilon}_{11} \geq 0$, $\dot{\epsilon}_{22} \leq 0$, and $\dot{\epsilon}_\theta = u/r = 0$ from Eq. (3.35b). Hence $u = 0$ and $\dot{\epsilon}_r = \partial u/\partial r = 0$ also. Let κ be the absolute value of the inclination of the $\dot{\epsilon}_2$ direction from the r-axis and define $\overline{w}$ as

$$\bar{w} = \text{sign } \gamma_{rz}.$$

Using Eq. (3.35b) and Figure 4-6, the value of κ is given by

$$\cos 2\kappa = \frac{\Omega-1}{\Omega+1} \cos 2\alpha \tag{4.20}$$

The description of the velocity field is completed by writing

$$\bar{w} \frac{\dot{\gamma}_{rz}}{\dot{\epsilon}_z} = \tan 2\kappa$$

which becomes upon substitution of the velocity expressions

$$\bar{w} \frac{\partial w}{\partial r} - \tan 2\kappa \frac{\partial w}{\partial z} = 0. \tag{4.21}$$

The characteristics for this first-order equation are the straight lines

$$\frac{dz}{dr} = - \bar{w} \tan 2\kappa \tag{4.22}$$

and the velocities along the characteristics are simply

$$dw = 0. \tag{4.23}$$

Once the principal strain rate directions have been determined, the principal stress directions can be determined at any point for any deviation α and the stress field can then be found from the equilibrium equations and the yield condition. From Figure 4-7 stress components satisfying the yield criterion are

$$\sigma_z = \sigma+(c\cos\phi-\sigma\sin\phi)\cos 2(\kappa+\bar{w}\alpha) \tag{4.24a}$$

$$\sigma_r = \sigma-(c\cos\phi-\sigma\sin\phi)\cos 2(\kappa+\bar{w}\alpha) \tag{4.24b}$$

$$\tau_{zr} = \bar{w}(c\cos\phi-\sigma\sin\phi)\sin 2(\kappa+\bar{w}\alpha), \tag{4.24c}$$

where

$$\sigma = \frac{1}{2}(\sigma_1+\sigma_2).$$

With some loss in generality, it will be assumed that α is a constant throughout. Then from the equations of equilibrium

$$\sigma_\theta = \sigma_r + r\frac{\partial\sigma}{\partial r}[1+\sin\phi\cos 2(\kappa+\bar{w}\alpha)]-r\frac{\partial\sigma}{\partial z}\sin\phi\sin 2(\kappa+\bar{w}\alpha) \tag{4.25a}$$

$$\frac{\partial\sigma}{\partial z}[1-\sin\phi\cos 2(\kappa+\bar{w}\alpha)]-\frac{\partial\sigma}{\partial r}\bar{w}\sin\phi\sin 2(\kappa+\bar{w}\alpha)$$

$$+\frac{\bar{w}}{r}(c\cos\phi-\sigma\sin\phi)\sin 2(\kappa+\bar{w}\alpha)+\gamma = 0. \tag{4.25b}$$

Equation (4.25b) has one set of characteristics given by the family of lines

$$\frac{dz}{dr} = -\bar{w}\frac{[1-\sin\phi\cos 2(\kappa+\bar{w}\alpha)]}{\sin\phi\sin 2(\kappa+\bar{w}\alpha)} \tag{4.26}$$

and the variation of σ along these lines is given by

$$\frac{d\sigma}{dr} + \frac{\sigma}{r} = \frac{c\ \cot\phi}{r} + \bar{w}\gamma\ \csc\phi\ \csc 2(\kappa+\bar{w}\alpha).$$

The solution to this equation is

$$\sigma = \frac{A}{r} + c\ \cot\phi + \frac{\bar{w}}{2}\gamma r\ \csc\phi\ \csc 2(\kappa+\bar{w}\alpha)$$

where A is an arbitrary constant to be evaluated on some curve intersecting the characteristics. Then the stresses can be written

$$\sigma_z = \left[\frac{A}{r} + \frac{\bar{w}\gamma r}{2}\csc\phi\ \csc 2(\kappa+\bar{w}\alpha)\right][1-\sin\phi\ \cos 2(\kappa+\bar{w}\alpha)] + c\ \cot\phi, \tag{4.27a}$$

$$\sigma_r = \left[\frac{A}{r} + \frac{\bar{w}\gamma r}{2}\csc\phi\ \csc 2(\kappa+\bar{w}\alpha)\right][1+\sin\phi\ \cos 2(\kappa+\bar{w}\alpha)] + c\ \cot\phi, \tag{4.27b}$$

$$\tau_{zr} = -\bar{w}\frac{A}{r}\sin\phi\ \sin 2(\kappa+\bar{w}\alpha) - \frac{\gamma r}{2}. \tag{4.27c}$$

Finally, it should be verified that the stresses satisfy the inequalities from Eq. (3.35a)

$$\sigma_1 > \sigma_\theta > \sigma_2.$$

4. Group IV

Regimes A and F comprise this group. In both cases one of the principal stresses in the r-z plane is equal to the circumferential stress σ_θ. Introducing the variables η and σ_o where η is the angle

which the plane of the positive critical shear stress forms with the r-axis (Figure 4-8) and where σ_o is the radius of the Mohr's circle for stress then, from Figure 4-9, stress components satisfying the Coulomb yield criterion are

$$\sigma_r = (c\ \cot\phi - \sigma_o \csc\phi) - \sigma_o \sin(\phi+2\eta), \tag{4.28a}$$

$$\sigma_z = (c\ \cot\phi - \sigma_o \csc\phi) + \sigma_o \sin(\phi+2\eta), \tag{4.28b}$$

$$\tau_{zr} = (c\ \cot\phi - \sigma_o \csc\phi)\cos(\phi+2\eta), \tag{4.28c}$$

$$\sigma_\theta = (c\ \cot\phi - \sigma_o \csc\phi) + \bar{w}\sigma_o, \tag{4.28d}$$

where

$$\bar{w} = +1 \text{ for regime F}$$

$$-1 \text{ for regime A.}$$

Substituting Eqs. (4.28) into the equilibrium equations

$$\frac{\partial \sigma_r}{\partial r} + \frac{\partial \tau_{zr}}{\partial z} + \frac{\sigma_r - \sigma_\theta}{r} = 0 \text{ and } \frac{\partial \tau_{zr}}{\partial r} + \frac{\partial \sigma_z}{\partial z} + \frac{\tau_{zr}}{r} + \gamma = 0,$$

yields

$$[\csc\phi + \sin(\phi+2\eta)]\frac{\partial \sigma_o}{\partial r} - \cos(\phi+2\eta)\frac{\partial \sigma_o}{\partial z} + 2\sigma_o\cos(\phi+2\eta)\frac{\partial \eta}{\partial r} \tag{4.29a}$$

$$+ 2\sigma_o \sin(\phi+2\eta)\frac{\partial \eta}{\partial z} + \frac{\sigma_o}{r}[\bar{w} + \sin(\phi+2\eta)] = 0$$

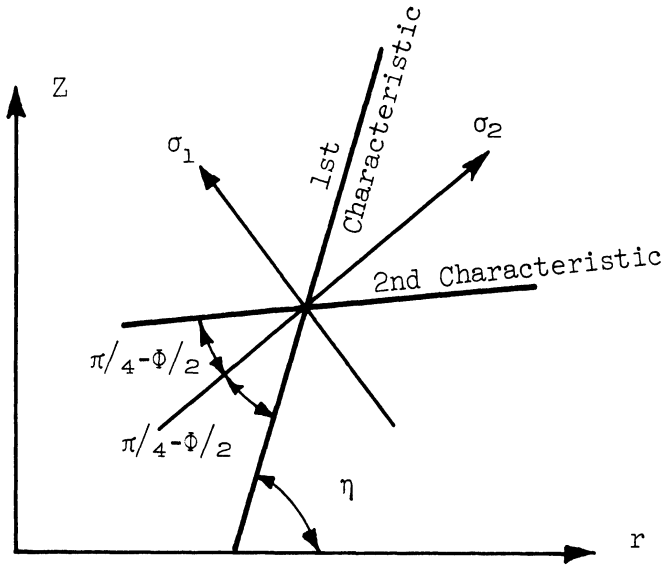

Figure 4-8. Stress characteristics and principal stress directions for group IV.

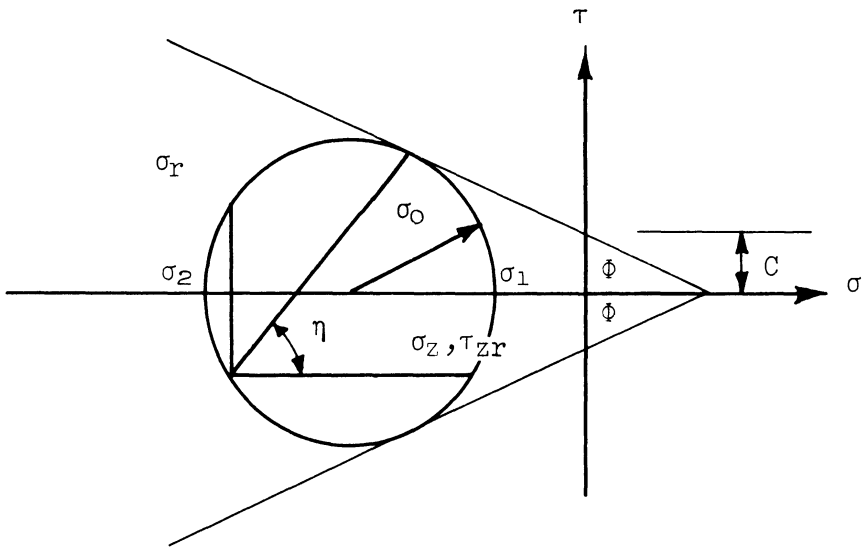

Figure 4-9. Mohr's circle for stress states of group IV.

$$\cos(\phi+2\eta)\,\frac{\partial\sigma_o}{\partial r} - [\csc\phi-\sin(\phi+2\eta)]\,\frac{\partial\sigma_o}{\partial z} - 2\sigma_o\sin(\phi+2\eta)\,\frac{\partial\eta}{\partial r}$$

(4.29b)

$$+ 2\sigma_o\cos(\phi+2\eta)\,\frac{\partial\eta}{\partial z} + \frac{\sigma_o}{r}\cos(\phi+2\eta)+\gamma \;=\; 0.$$

These two Eqs. (4.29) together with the equations

$$d\sigma_o \;=\; \frac{\partial\sigma_o}{\partial r}\,dr + \frac{\partial\sigma_o}{\partial z}\,dz, \qquad (4.30a)$$

$$d\eta \;=\; \frac{\partial\eta}{\partial r}\,dr + \frac{\partial\eta}{\partial z}\,dz, \qquad (4.30b)$$

can be used to find the variation of σ_o and η along any chosen direction. The most convenient or characteristic directions are found from

$$\left(\frac{dz}{dr}\right)^2 + (\cot(\phi+\eta)-\tan\eta)\,\frac{dz}{dr} - \cot(\phi+\eta)\tan\eta \;=\; 0.$$

Solutions are

$$\frac{dz}{dr} \;=\; \begin{cases} \tan\eta \text{ which are called the first characteristic directions and} \\ \tan(\eta+\pi/2+\phi) \text{ which are the second characteristic directions.} \end{cases}$$

(4.31a)

Hence it is seen that the characteristics are the lines of critical Coulomb shear stress. The variation of the dependent variables σ_o and η along the first characteristic directions is given by

$$d\sigma_o+2\tan\phi\sigma_o d\eta + \frac{\sigma_o\tan\phi}{r}\,[\bar{w}\cos\phi dr+(1-\bar{w}\sin\phi)dz]-\tan\phi(\sin\phi dr+\cos\phi dz)\gamma = 0$$

(4.32a)

and on the second characteristics by,

$$d\sigma_o - 2\tan\phi\sigma_o d\eta + \frac{\sigma_o \tan\phi}{r}[\bar{w}\cos\phi dr - (1-\bar{w}\sin\phi)dz] + \tan\phi(\sin\phi dr - \cos\phi dz)\gamma = 0. \tag{4.32b}$$

For regimes A and F, $\dot{\epsilon}_{11} \geq 0$ and $\dot{\epsilon}_{22} \leq 0$, and the principal directions of stress and strain rate do not necessarily coincide but can deviate by α. One of the independent relationships involving the strain rates is the relationship between the directions of principal stress and strain rate. Noting Figures 4-10 and 4-11 this can be expressed by

$$\frac{\dot{\gamma}_{rz}}{\dot{\epsilon}_r - \dot{\epsilon}_z} = \tan 2\nu, \text{ where } \nu = \eta - (\pi/4 - \phi/2) + \alpha \tag{4.33}$$

The angle η is the inclination of the first stress characteristic and it must be determined from stress considerations. Hence ν is considered as known for any α. The second independent relationship on the strain rates is given by Eqs. (3.36b) and (3.37b)

$$\dot{\epsilon}_{11} + \Omega\,\dot{\epsilon}_{22} + \dot{\epsilon}_\theta = 0 \text{ for regime F} \tag{3.36b}$$

and

$$\Omega^{-1}\,\dot{\epsilon}_{11} + \dot{\epsilon}_{22} + \dot{\epsilon}_\theta = 0 \text{ for regime A.} \tag{3.37b}$$

From Figure 4-11 strain rates in the principal stress directions are

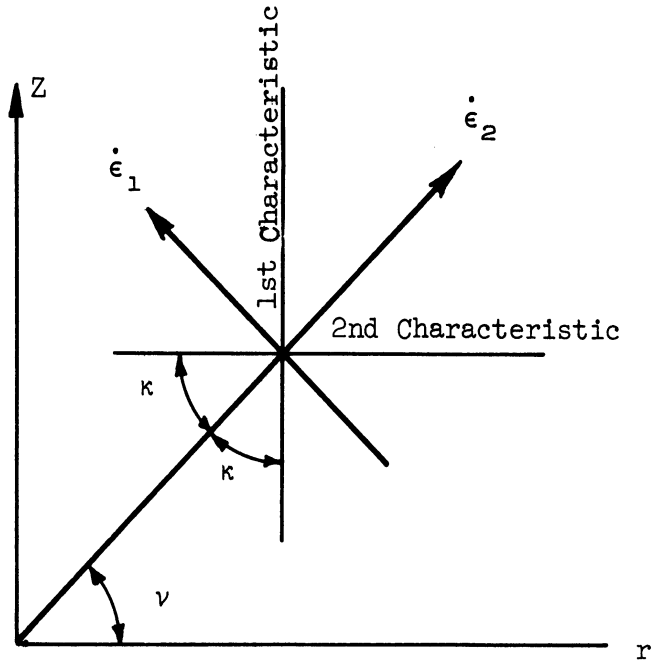

Figure 4-10. Velocity characteristics and principal strain rate directions for group IV.

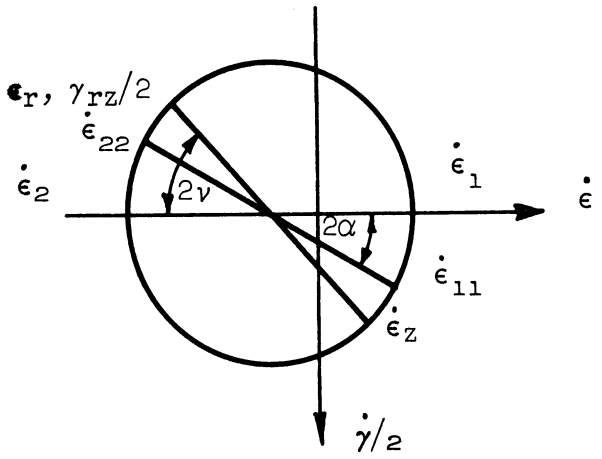

Figure 4-11. Mohr's circle for strain rates of group IV.

$$\dot{\epsilon}_{11} = \frac{1}{2}(\dot{\epsilon}_z+\dot{\epsilon}_r) + \frac{1}{2}(\dot{\epsilon}_z-\dot{\epsilon}_r)\frac{\cos 2\alpha}{\cos 2\nu}, \tag{4.34a}$$

$$\dot{\epsilon}_{22} = \frac{1}{2}(\dot{\epsilon}_z+\dot{\epsilon}_r) - \frac{1}{2}(\dot{\epsilon}_z-\dot{\epsilon}_r)\frac{\cos 2\alpha}{\cos 2\nu}. \tag{4.34b}$$

Then letting

$$\cos 2\kappa = \frac{\Omega-1}{\Omega+1}\cos 2\alpha = \frac{\sin\beta}{\cos(\phi-\beta)}\cos 2\alpha \tag{4.35}$$

the second independent relationship can be written

$$\dot{\epsilon}_r - \dot{\epsilon}_z \tan(\nu+\kappa)\tan(\nu-\kappa) + \frac{\cos 2\nu \dot{\epsilon}_\theta}{\cos(\nu+\kappa)\cos(\nu-\kappa)(1+\Omega^{\overline{w}})} = 0. \tag{4.36}$$

Writing these two equations in terms of the velocities, it can be seen that the velocity field so described is hyperbolic, with characteristics defined by

$$\frac{dz}{dr} = \begin{cases} \tan(\nu+\kappa) & \text{which are the first velocity characteristics and} \\ \tan(\nu-\kappa) & \text{which are the second velocity characteristics.} \end{cases} \tag{4.37}$$

Along the characteristics, the velocities for the first velocity characteristics are given by

$$du+\tan(\nu+\kappa)dw + \left[\frac{dr}{(1+\Omega^{\overline{w}})\cos^2(\nu+\kappa)}\right]\frac{u}{r} = 0 \tag{4.38a}$$

and on the second velocity characteristics by,

$$du+\tan(\nu-\kappa)dw+\left[\frac{dr}{(1+\bar{\Omega}^{w})\cos^{2}(\nu-\kappa)}\right]\frac{u}{r} = 0. \qquad (4.38b)$$

The relationship of the velocity characteristics to the stress characteristics is a function of the dilatation rate and of the deviation angle α. In general the velocity characteristics will not coincide with the stress characteristics since in all but the perfect plasticity case, the angle between the velocity characteristics 2κ is greater than the corresponding angle between the stress characteristics $\pi/2-\phi$ (compare Figure 4-8 and Figure 4-10). However, the principal stress and strain rate directions can deviate so that there is the possibility that one set of velocity and stress characteristics can coincide. This deviation is limited by

$$-\frac{1}{2}(\phi-\beta) \leq \alpha \leq \frac{1}{2}(\phi-\beta).$$

For the upper limit of this inequality, Eq. (4.35) gives the angle

$$\kappa = \pi/4 - \beta/2.$$

Hence the inclination of the second velocity characteristic

$$\eta-(\pi/4-\phi/2)+\alpha-\kappa = \eta-(\pi/4-\phi/2)+(\phi/2-\beta/2)-(\pi/4-\beta/2) = \eta-(\pi/2-\phi)$$

is also the inclination of the second stress characteristic from Figure 4-10. Similarly first velocity and stress characteristics coincide for the lower limit of the inequality. Hence just as in the plane

strain case, the slip-expansion model allows enough freedom in the possible directions of the principal strain rates so that one set of stress and velocity characteristics can coincide for expansion rates smaller than that required by perfect plasticity. Again it is interesting to note that for the perfect plasticity condition $\beta = \phi$, then $\alpha = 0$ and $\kappa = \pi/4-\phi/2$ and both sets of velocity and stress characteristics coincide.

5. Summary

Summing up the results of the investigation of the axially symmetric velocity and stress fields for each of the regimes of the Coulomb yield surface, it can be seen that the regimes of Groups I and III admit only trivial stress or velocity solutions and hence will be of very limited importance. The regimes of Group II produce kinematically determinate velocity fields in the sense that there are sufficient equations to determine the velocities if sufficient velocity boundary conditions are known. The stress field is not statically determinate since it requires the determination of the principal strain rate directions and hence the principal stress directions by the velocity analysis. The regimes of Group IV are statically determinate in the same sense as given above. The velocity field is indeterminate and can be found only after the stress field has been determined.

CHAPTER V

SPECIFIC SOLUTIONS

Adopting the generalized Coulomb yield criterion, an associated flow rule with a reasonably arbitrary dilatation rate has been derived. Next, a study of the stress and velocity solutions for the various sides and corners of the yield surface has shown that only the regimes of Groups II and IV are important. Of these two groups, the statically determinate Group IV has been the more popular and although the suitability of both groups should be checked for each problem, Group IV will probably be the more important. However, the flow rule is not sufficiently restricted for the regimes of this group as the relationship between the directions of principal stress and strain rate is undetermined. Thus the velocity field contains a degree of freedom which can be varied to correlate with experimental results. In this chapter a problem will be sought in which some feature of the velocity field provides an observable from which an estimate of the deviation of the principal directions can be made.

A. THE TRIAXIAL TEST

Since the most common axially symmetric test in soil mechanics is the triaxial test, it is a logical first choice in the search for a velocity observable. The discussion here will be restricted to the

standard compression test.

Let the specimen have the dimensions and coordinate systems as shown in Figure 5-1. In the standard compression test the loading is an ambient pressure plus an additional vertical load applied through relatively rigid end caps. If it is assumed that the end caps are sufficiently rough that radial slippage is prevented, then the boundary conditions may be completely stated as

$$\left.\begin{aligned} \tau_{zr} &= 0 \\ \sigma_r &= -p \end{aligned}\right\} \quad \text{at } r = D/2, \quad L/2 \geq z \geq -L/2, \tag{5.1}$$

$$\left.\begin{aligned} w &= \text{constant} \\ u &= 0 \end{aligned}\right\} \quad \text{at } z = \pm L/2, \quad D/2 \geq r \geq 0. \tag{5.2}$$

It seems likely that the negative vertical stress is larger in magnitude than either the radial or circumferential stresses, hence regime F is applicable. Further, let it be assumed that effects of material weight are negligible so that γ may be set zero. Then using Eqs. (4.31) and (4.32) the characteristics and the stresses are uniquely determined in the region shown in Figure 5-2 from the boundary values of Eq. (5.1). The stresses in this region are

$$\sigma_r = \sigma_\theta = -p \tag{5.3a}$$

$$\sigma_z = -p\tan^2(\pi/4+\phi/2)-2c\tan(\pi/4+\phi/2). \tag{5.3b}$$

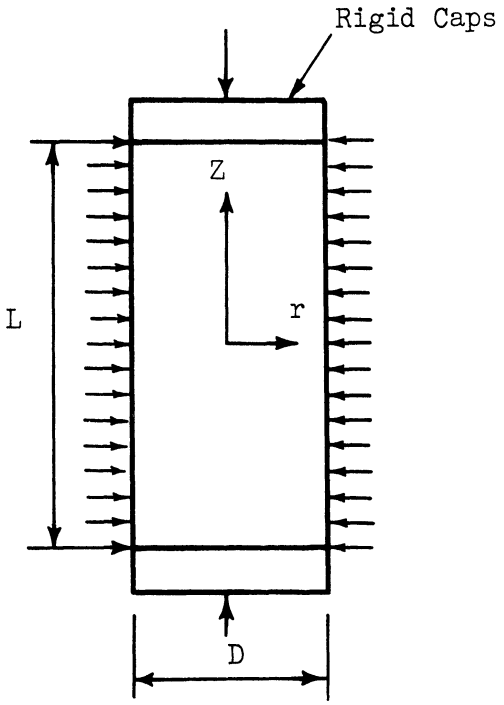

Figure 5-1. Triaxial specimen.

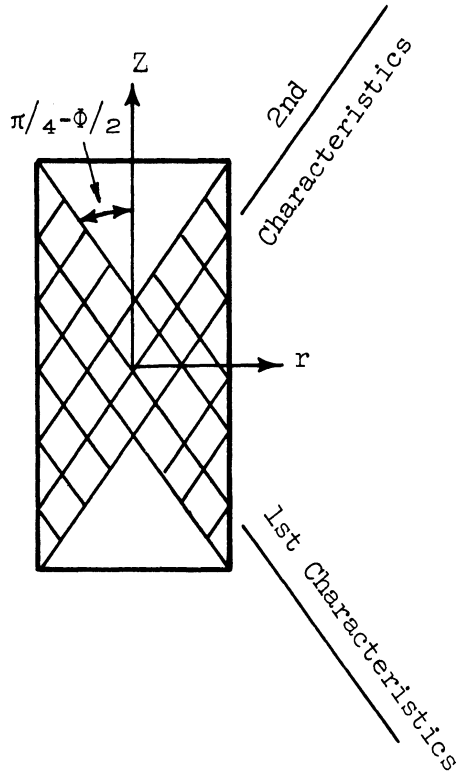

Figure 5-2. Stress Characteristics determined from the lateral boundary conditions.

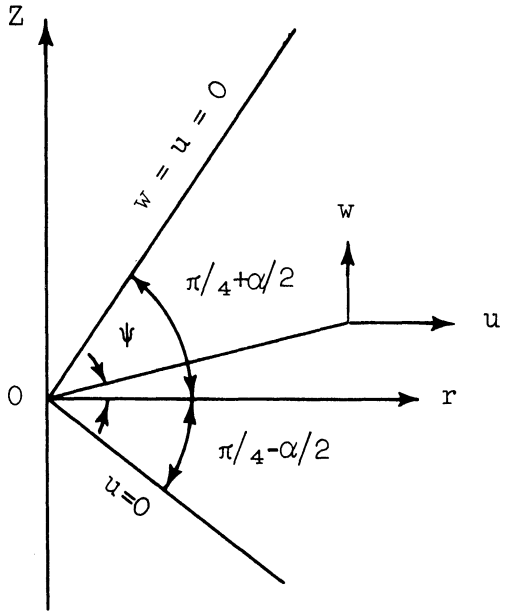

Figure 5-3. Velocity zones for a triaxial specimen.

The stresses in the conical zones adjacent to the caps cannot be uniquely determined due to the lack of sufficient stress boundary conditions.

A theoretical and experimental investigation of the velocity fields of triaxial specimens was made by Haythornthwaite.[29] He measured the length of the velocity field during two stages of the total deformation to failure. During the initial stage, the deformation occurred over almost the entire length of the specimen. At a later stage, the length of the deforming zone was very nearly equal to the diameter. Unfortunately, the variety of the theoretically possible velocity fields makes definite correlation with the experimental results nearly impossible. As an example of one of these fields, a somewhat new velocity field will be found, and its significance with respect to the test results and to determining the relationship between the principal stress and strain rate directions will be discussed.

The velocities in the statically determined region shown in Figure 5-2 can be found from Eqs. (4.38). However, in this case it is simpler to obtain them directly from Eqs. (4.33) and (3.36b). Assuming in this case that the dilatation rate is small enough to be neglected, then

$$\frac{\partial u}{\partial z} + \frac{\partial w}{\partial r} = \left(\frac{\partial u}{\partial r} - \frac{\partial w}{\partial z}\right) \tan 2\alpha \qquad (5.4a)$$

$$\frac{\partial u}{\partial r} + \frac{\partial w}{\partial z} + \frac{u}{r} = 0. \tag{5.4b}$$

Haythornthwaite[29] obtained a solution to these equations by assuming that the velocity components u and w at a point are functions of only the angle between the r-axis and a line from the origin to the point. Hence using the notation of Figure 5-3

$$u = u(\psi) \text{ and } w = w(\psi) \text{ where } \tan\psi = z/r.$$

Then velocities satisfying the boundary conditions

$$w = u = 0 \text{ when } \psi = \pi/4 + \alpha, \tag{5.5a}$$

$$w = 1 \text{ when } \psi = 0, \tag{5.5b}$$

are given by

$$u = \frac{\cos^2 2\alpha \sqrt{1+2\tan 2\alpha \tan\psi - \tan^2\psi}}{\frac{\pi}{2} + \frac{1}{2}\sin 4\alpha + 2\alpha} \tag{5.6a}$$

$$w = \frac{\frac{\pi}{2} + \frac{1}{2}\sin 4\alpha \sqrt{1+2\tan 2\alpha \tan\psi - \tan^2\psi - \sin^{-1}(\tan\psi \cos 2\alpha - \sin 2\alpha)}}{\frac{\pi}{2} + \frac{1}{2}\sin 4\alpha + 2\alpha} \tag{5.6b}$$

Another interesting boundary condition satisfied by Eqs. (5.6) is that

$$u = 0 \text{ when } \psi = -(\pi/4 - \alpha). \tag{5.7}$$

Using this fact, a complete velocity field satisfying the velocity boundary conditions required by Eq. (5.2) is as follows: (1) the velocities in the region above the line $\psi = \pi/4+\alpha$ are identically zero; (2) the region below the line $\psi = -\pi/4+\alpha$ is moving vertically as a rigid body; (3) the velocities in the intermediate region are given by Eqs. (5.6). Figure 5-4 shows the deformation of a grid resulting from this velocity field being maintained for a finite deformation.

Since Haythornthwaite sought to determine α from the measurements of the sizes of actual triaxial velocity fields, it is important to investigate the changes in the size of this new field for various values of α. From Figure 5-3, the length of the deforming zone is simply

$$L = \frac{D}{2}\left[\tan(\pi/4+\alpha) + \tan(\pi/4-\alpha)\right]$$

which reduces to the simple expression

$$L = D\sec 2\alpha. \qquad (5.8)$$

Hence this velocity solution could well explain the short deformation zone observed by Haythornthwaite during the later stages of failure. However, recalling that $-\phi/2 \leq \alpha \leq \phi/2$, the length of the deforming region given by Eq. (5.8) for an angle of friction of, say 35°, varies at most by only some 22% between the largest

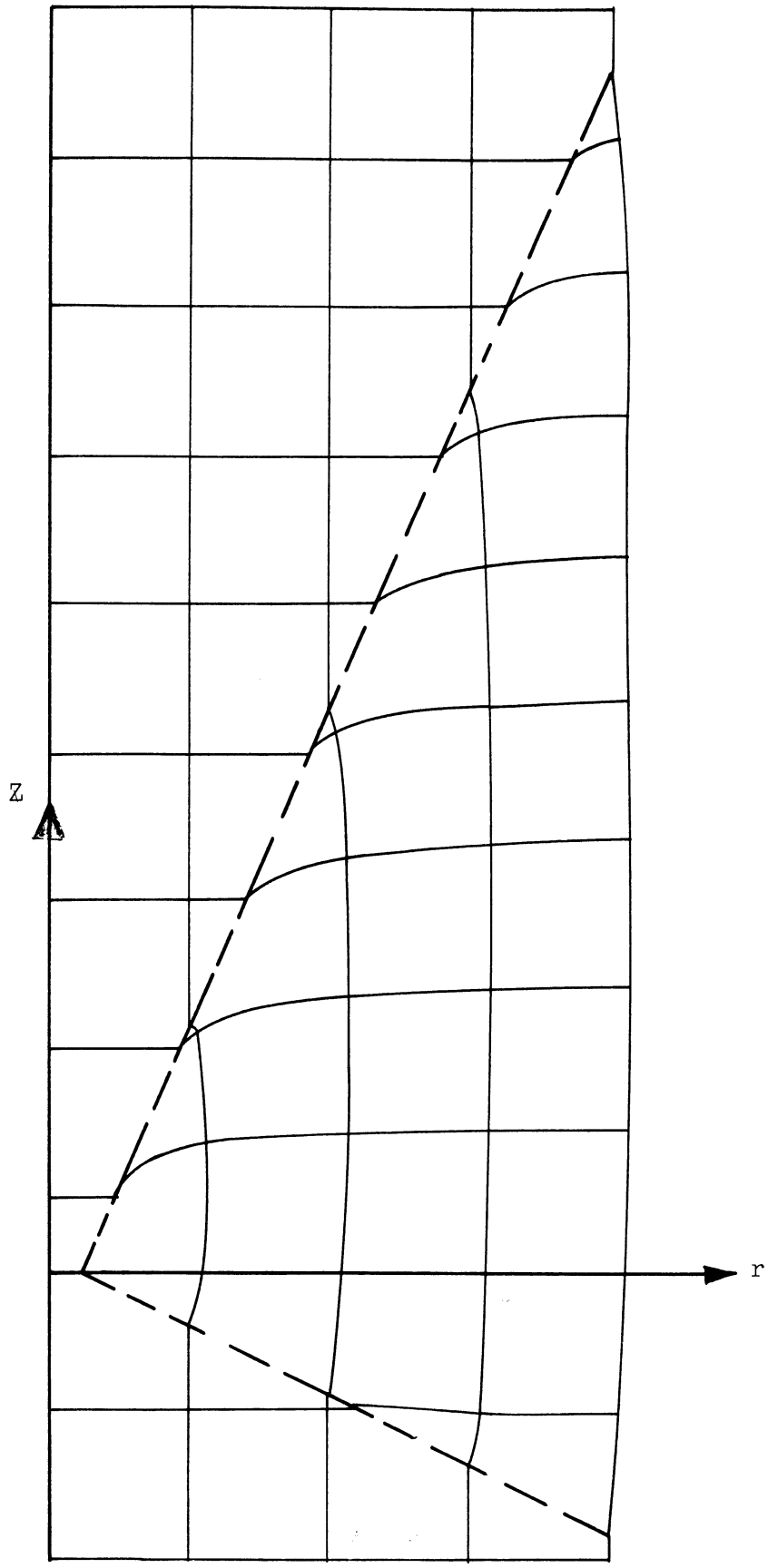

Figure 5-4. Deformation of a grid resulting from maintaining a triaxial velocity field for a finite deformation, (α = 20°).

absolute value of the deviation and zero deviation. Since this particular velocity field shows that the length of the deforming zone is not sufficiently sensitive to α, the triaxial test was abandoned as a means of determining α.

B. THE PROBLEM OF THE RIGID CIRCULAR PUNCH INDENTING A SEMI-INFINITE REGION

A punching type of test was considered next because an easily perceived and readily measured velocity observable, the extent of the deforming zone at the surface, exists for this type of test. Furthermore, the amount of material deforming and the type of velocity field occurring are such that the observable is quite sensitive to any predominance of a certain angle of deviation between the principal stress and strain rate directions. For example, in the plane strain problem of the identation of a weightless Coulomb material by a smooth, rigid, flat-ended punch deforming according to the velocity field due to Hill,[37] shown in Figure 5-5, the three cases where the deviation is exclusively at one extreme, at zero, and at the other extreme are shown in Table II.

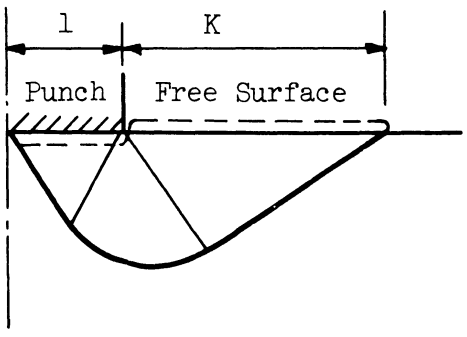

Figure 5-5. Deformation of a weightless Coulomb material by a strip punch.

TABLE II

RADIUS OF THE DEFORMING REGION FOR PLANE STRAIN INDENTATION OF A WEIGHTLESS COULOMB MATERIAL

α(deviation)	K	K($\phi = 30°$)
$\phi/2$	$\cot(\pi/4-\phi/2)e^{(\pi\tan\phi)/2}$	4.29
0	$e^{\pi/2}\tan\phi/2$	1.56
$-\phi/2$	$\tan(\pi/4-\phi/2)$	.577

If the extent of the deforming region corresponding to $\alpha = \phi/2$ or $\alpha = -\phi/2$ is observed, it can be concluded that the principal stress and strain directions are deviating by the corresponding amount throughout the deforming zone. However, the observation of a field corresponding to perfect coincidence can only indicate that the material may be deforming in this manner throughout since an infinity of combinations of varying deviations can be constructed to give the same intersection point of the deforming zone with the free surface.

The axially symmetric punch problem has been the subject of several investigations. Shield[34] has presented a detailed discussion and a numerical solution of the problem for materials which obey the Tresca yield criterion. This analysis was extended to materials yielding according to the Coulomb criterion by Cox, Eason, and Hopkins[20] for the case of weightless materials and by Cox[38] for the material with weight. However, the stress fields for the latter two investigations were computed including a surcharge of atmospheric pressure. This

case is not normally realized in practice and in this study the stress fields are computed for the more usual circumstance of zero surcharge.

1. Stress Field

A necessary preliminary to the use of the circular punch test to identify deviations between the principal stress and strain directions is an analysis of the stress distribution. The problem is statically determinate if the actual friction occurring on the punch face (not necessarily the maximum angle of friction) during plastic flow is known. The case of zero friction was chosen. The problem must be statically determinate so that the stress field can be found independently of any assumptions regarding the nature of the flow rule.

Let the material occupy the region $z \geq 0$ with the origin of coordinates located at the center of the punch. Let the radius of the punch be R. Assume that the cylindrical punch is rigid, flat ended, and perfectly smooth. The boundary conditions under the punch are then

$$\left.\begin{aligned} \tau_{zr} &= 0 \qquad (5.9a) \\ w &= w_o = \text{constant} \qquad (5.9b) \end{aligned}\right\} \text{ on } 0 \leq r < R, \quad z = 0.$$

Let the surface outside the punch be stress free. This boundary condition is normally realized in practice since most granular media are not impervious and the atmospheric pressure is within the material. The boundary conditions expressing this situation are

$$\tau_{zr} = \sigma_z = 0 \text{ on } r > R, \quad z = 0. \tag{5.10}$$

Since the material is cohesionless and no surcharge acts on the surface, the strength of the material is dependent on its weight. This suggests that Eqs. (4.32) may be put into nondimensional form most simply and conveniently by expressing each length in terms of the punch radius R and by replacing the radius of the Mohr's circle, σ_o, by the parameter $F = \frac{\sigma_o}{\gamma R}$. Thus Eqs. (4.32) on the first characteristics become,

$$dF + 2\tan\phi F d\eta + \frac{F\tan\phi}{r}\left[\bar{w}\cos\phi dr+(1-\bar{w}\sin\phi)dz\right]-\tan\phi(\sin\phi dr+\cos\phi dz) = 0 \tag{5.11a}$$

and on the second characteristics become

$$dF - 2\tan\phi F d\eta + \frac{F\tan\phi}{r}\left[\bar{w}\cos\phi dr-(1-\bar{w}\sin\phi)dz\right]+\tan\phi(\sin\phi dr-\cos\phi dz) = 0 \tag{5.11b}$$

Considering stresses only, the corner regimes A and F are distinguished by comparing the relative magnitude of the unequal principal stress with that of the two equal ones. At A the unequal principal stress is larger and at F it is smaller than the two equal stresses. It seems reasonable to suppose that the vertical stress under the punch is smaller (larger negatively) than the radial or circumferential stresses. At or near the free surface, the radial stress is probably smaller than the vertical stress, which becomes zero at the surface,

and it might well be smaller than the circumferential stress. This suggests the use of regime F throughout and consequently $\overline{w} = +1$ will be used in Eqs. (5.11).

With the help of Figures 5-6 and 5-7 the boundary conditions can be written in terms of the dependent variables F and η. Taking first the conditions at the free boundary, Figure 5-6 shows the state of stress satisfying Eq. (5.10). From this it can be shown that

$$\left.\begin{aligned} F &= \frac{c}{R\gamma}\cot(\pi/4-\phi/2) \\ \eta &= \pi/4-\phi/2 \end{aligned}\right\} \quad \text{on } r > R, \quad z = 0. \qquad (5.12)$$

For a cohesionless material F vanishes and the direction of the characteristics is undetermined, but if a cohesionless material is considered as the limiting state as the cohesion c approaches zero, then it is seen that

$$\left.\begin{aligned} F &= 0 \\ \eta &= \pi/4-\phi/2 \end{aligned}\right\} \quad \text{on } r > R, \quad z = 0. \qquad (5.13)$$

Similarly from Figure 5-7 it can be seen that Eq. (5.9a) is satisfied by the expression

$$\eta = \frac{3}{4}\pi - \frac{\phi}{2} \quad \text{on } 0 \leq r < R, \quad z = 0, \qquad (5.14a)$$

and that the normal punch pressure can be found from

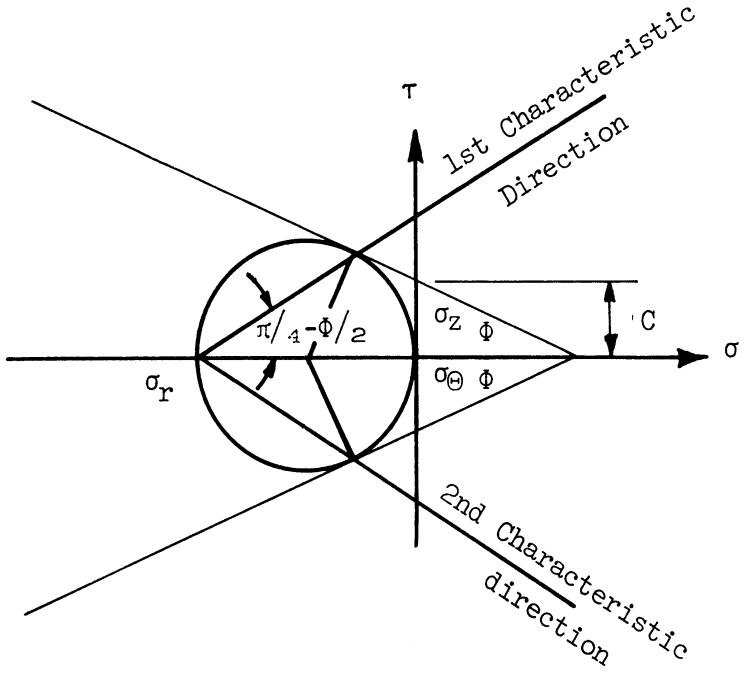

Figure 5-6. State of stress at the free boundary.

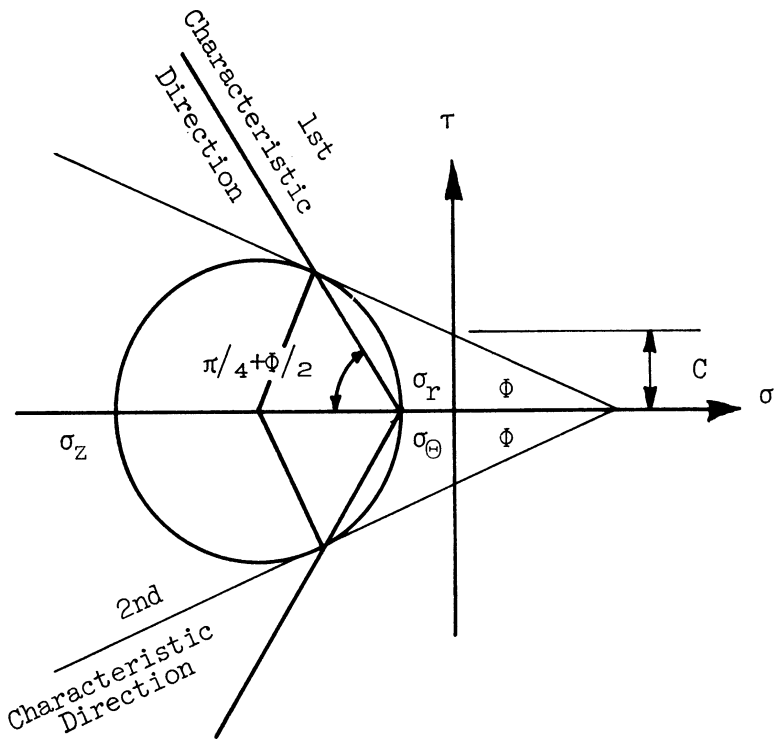

Figure 5-7. State of stress under the punch.

$$\frac{\sigma_z}{R\gamma} = -[F(1+\csc\phi) - \frac{c}{R\gamma}\cot\phi] \quad \text{on } 0 \leq r < R, \quad z = 0. \tag{5.14b}$$

From the boundary conditions, Eqs. (5.13) and (5.14a), it can be seen that the characteristics must change their angle rapidly in going from the stress free boundary to the flat punch boundary. This suggests a field of characteristics as shown in Figure 5-8 in which a fan of characteristics centered at the edge of the punch accomplishes the required change in angle. Such a type of field is to be expected from the solution of the analogous plane strain problem. The fan center, point A, is the point of intersection for all of the first characteristics in the fan; therefore, the inclination of the first characteristic takes on many values here. Just to the right of A the boundary conditions are given by Eq. (5.13) and so the characteristic at the edge of the fan, AC, is initially inclined at $\pi/4-\phi/2$ to the r-axis. The conditions just to the left of A are given by Eqs. (5.14) and hence the characteristic AD starts out at $3/4\pi-\phi/2$ to the r-axis. This limits the included angle of the fan to $\pi/2$.

The variation of the stress parameter around the singular point A can be found by considering the point to be a degenerate second characteristic of zero length, then Eq. (5.11b) becomes

$$d(\cot\phi \ln F) - 2d\eta = 0.$$

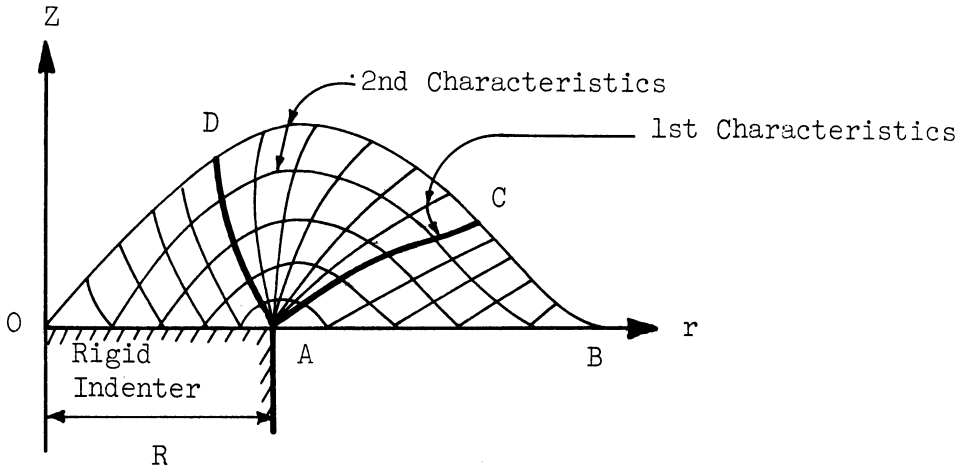

Figure 5-8. Field of stress characteristics for circular punch indentation.

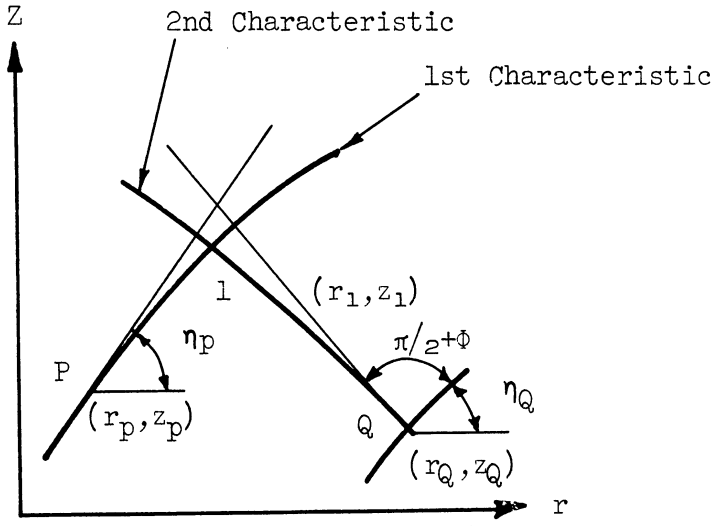

Figure 5-9. Illustration of typical calculation situation.

Integrating and imposing the known conditions at the free boundary, Eqs. (5.12), the variation of the stress parameter around the singularity becomes

$$\ln\left[\frac{F}{\frac{c}{R\gamma}\frac{\cos\phi}{1-\sin\phi}}\right] = 2[\eta-(\pi/4-\phi/2)]\tan\phi \qquad (5.15)$$

For the case of a cohesionless material, the logarithmic term becomes indefinitely large and the only way to preserve the equality is to set F = 0. Hence all the stress components are zero if the singularity is approached from any direction.

The field of characteristics and the stress distribution can be obtained by the integration of the differential equations involving F and η along the characteristics simultaneously with the differential equations of the characteristics themselves. The solution of these equations usually involves a numerical procedure because of the difficulties in obtaining an analytical solution. The numerical procedure is based on a finite difference approximation of Eqs. (4.31) and (5.11). These finite difference equations are in turn used to extend the solution from the boundary values.

In the usual situation F, η, r, and z are known at two intersections P, Q of the characteristics as in Figure 5-9. It is desired to extend the solution to point 1. The unknown coordinates (r_1,z_1) can be initially approximated by finding the intersection of the two characteristics if they are extended at their initial inclination. This

means solving the equations

$$\frac{z_1-z_p}{r_1-r_p} = \tan\eta_p \text{ and } \frac{z_1-z_Q}{r_1-r_Q} = \tan(\eta_Q+\pi/2+\phi) \text{ for } r_1 \text{ and } z_1.$$

However, subsequent approximations for r_1 and z_1 can be made more accurately by extending each characteristic one-half its projection at the initial angle and one-half its projection at the approximated angle of the characteristic at the point being determined. Hence for the first characteristic

$$\frac{z_{1/2}-z_p}{r_{1/2}-r_p} = \tan\eta_p \text{ and } \frac{z_1-z_{1/2}}{r_1-r_{1/2}} = \tan\eta_1.$$

If one-half the vertical projections are used, then $r_{1/2}$ and $z_{1/2}$ can be eliminated for the first characteristics to give,

$$\frac{r_1-r_p}{z_1-z_p} = \frac{\cot\eta_p+\cot\eta_1}{2} \qquad (5.16a)$$

and for the second characteristics to give,

$$\frac{r_1-r_Q}{z_1-z_Q} = \frac{\cot(\eta_Q+\pi/2+\phi)+\cot(\eta_1+\pi/2+\phi)}{2}$$

Solving these in turn for r_1 and z_1

$$z_1 = \frac{z_p(\cot\eta_p+\cot\eta_1)+z_Q[\cot(\eta_Q+\pi/2+\phi)+\cot(\eta_1+\pi/2+\phi)]+2(r_Q-r_p)}{[\cot\eta_p+\cot\eta_1-\cot(\eta_Q+\pi/2+\phi)-\cot(\eta_1+\pi/2+\phi)]} \tag{5.17a}$$

$$r_1 = \frac{\left[r_Q(\cot\eta_p+\cot\eta_1)-r_p[\cot(\eta_Q+\pi/2+\phi)+\cot(\eta_1+\pi/2+\phi)]\right.}{\left.+\frac{1}{2}(z_p-z_Q)(\cot\eta_p+\cot\eta_1)[\cot(\eta_Q+\pi/2+\phi)+\cot(\eta_1+\pi/2+\phi)]\right]}{[\cot\eta_p+\cot\eta_1-\cot(\eta_Q+\pi/2+\phi)-\cot(\eta_1+\pi/2+\phi)]} \tag{5.17b}$$

The equations on the dependent variables f and η along the characteristics are approximated by the finite difference equations on the first characteristic,

$$F_1-F_p+\tan\phi(F_1+F_p)(\eta_1-\eta_p)+\left(\frac{F_1+F_p}{r_1+r_p}\right)\tan\phi[\bar{w}\cos\phi(r_1-r_p)$$

$$+(1-\bar{w}\sin\phi)(z_1-z_p)]-\tan\phi[\sin\phi(r_1-r_p)+\cos\phi(z_1-z_p)] = 0 \tag{5.18a}$$

and on the second characteristic,

$$F_1-F_Q-\tan\phi(F_1+F_Q)(\eta_1-\eta_Q)+\left(\frac{F_1+F_Q}{r_1+r_Q}\right)\tan\phi[\bar{w}\cos\phi(r_1-r_Q)$$

$$-(1-\bar{w}\sin\phi)(z_1-z_Q)]+\tan\phi[\sin\phi(r_1-r_Q)-\cos\phi(z_1-z_Q)] = 0 \tag{5.18b}$$

Then F_1 and η_1 are

$$F_1 = \frac{1}{D}\left\{ F_p+F_Q-\tan\phi\left[F_p(\eta_1-\eta_p)-F_Q(\eta_1-\eta_Q)+\bar{w}\cos\phi\left(F_p\left(\frac{r_1-r_p}{r_1+r_p}\right)+F_Q\left(\frac{r_1-r_Q}{r_1+r_Q}\right)\right)\right.\right.$$
$$\left.\left. + (1-\bar{w}\sin\phi)\left(F_p\left(\frac{z_1-z_p}{r_1+r_p}\right)-F_Q\left(\frac{z_1-z_Q}{r_1+r_Q}\right)\right)-\sin\phi(r_Q-r_p)-\cos\phi(2z_1-z_p-z_Q)\right]\right\} \quad (5.19a)$$

where

$$D = 2 + \tan\phi\left[\eta_Q-\eta_p+\bar{w}\cos\phi\left(\frac{r_1-r_p}{r_1+r_p}+\frac{r_1-r_Q}{r_1+r_Q}\right)+(1-\bar{w}\sin\phi)\left(\frac{z_1-z_p}{r_1+r_p}-\frac{z_1-z_Q}{r_1+r_Q}\right)\right]$$

$$\eta_1 = \frac{1}{2}\left[\eta_p+\eta_Q-\bar{w}\cos\phi\left(\frac{r_1-r_p}{r_1+r_p}-\frac{r_1-r_Q}{r_1+r_Q}\right)-(1-\bar{w}\sin\phi)\left(\frac{z_1-z_p}{r_1+r_p}+\frac{z_1-z_Q}{r_1+r_Q}\right)\right.$$
$$\left. + \cos\phi\left(\frac{z_1-z_p}{F_1+F_p}-\frac{z_1-z_Q}{F_1+F_Q}\right)+\sin\phi\left(\frac{r_1-r_p}{F_1+F_p}+\frac{r_1-r_Q}{F_1+F_Q}\right)-\cot\phi\left(\frac{F_1-F_p}{F_1+F_p}-\frac{F_1-F_Q}{F_1+F_Q}\right)\right] \quad (5.19b)$$

After the initial approximations for r_1 and z_1 are calculated, η_1 is estimated and a new F_1 and η_1 can be calculated from Eqs. (5.19). Subsequently a new r_1 and z_1 can be calculated from Eq. (5.17) and the iteration performed until successive values become sufficiently unchanged.

In this manner the characteristics and stresses in field ABC are uniquely determined from the known boundary AB and from the boundary values of F and η along it. Following the same procedure the stresses and characteristics are uniquely determined in the fan CAD from the computed values along the characteristic AC and from the boundary values

at the singularity A. Finally, the region ADO is uniquely computed starting from computed values on the first characteristic AD and knowing that the second characteristics terminate on the line z = 0 at the inclination of $\pi/4+\phi/2$ to the r-axis. The radius at which this occurs can be found from Eq. (5.16b)

$$\frac{r_1-r_Q}{0-z_Q} = \frac{\cot(\eta_Q+\pi/2+\phi)+\cot(5\pi/4+\phi 2)}{2} . \qquad (5.20)$$

Simply solving for r_1

$$r_1 = -\frac{z_Q}{2}\left[\cot(\eta_Q+\pi/2+\phi)+\cot(5/4\pi+\phi/2)+r_Q\right.$$

The equation on the dependent variables F and η along the second characteristic is

$$F_1-F_Q-\tan\phi(F_1+F_Q)(3/4\pi-\phi/2-\eta_Q)$$

$$+\frac{\tan\phi(F_1+F_Q)}{(r_1+r_Q)}\left[\bar{w}\cos\phi(r_1-r_Q)-(1-\bar{w}\sin\phi)(z_1-z_Q)\right]$$

$$+\tan\phi[\sin\phi(r_1-r_Q)-\cos\phi(z_1-z_Q)] = 0.$$

Then F on the punch surface is found to be

$$F_1 = \frac{F_Q\left[1+\tan\phi(3/4\pi-\phi/2-\eta_Q)-\bar{w}\sin\phi\left(\frac{r_1-r_Q}{r_1+r_Q}\right)+\tan\phi(1-\bar{w}\sin\phi)\left(\frac{z_1-z_Q}{r_1+r_Q}\right)\right]}{1-(3/4\pi-\phi/2-\eta_Q)\tan\phi+\bar{w}\sin\phi\left(\frac{r_1-r_Q}{r_1+r_Q}\right)-\tan\phi(1-\bar{w}\sin\phi)\left(\frac{z_1-z_Q}{r_1+r_Q}\right)}$$

$$-\tan\phi[\sin\phi(r_1-r_Q)-\cos\phi(z_1-z_Q)] \qquad (5.21)$$

and the normal pressure under the punch can be found from Eq. (5.14b).

The above procedure was programmed on the IBM 7090 digital computer at The University of Michigan. The iteration at each point was terminated when the change in every variable (r,z,F, and η) fell below 10^{-5} of its previous value. The number of iterations required to attain this accuracy was usually five. Whenever a characteristic experienced a change in angle of more than 6° from point to point, the mesh size was decreased locally until this requirement was satisfied. As a result, the mesh size became very small near the singularity point due to the large curvature of the characteristic AD at the singularity. In order to keep the required mesh size from becoming prohibitively small, a slight surface pressure of the order of $10^{-2}R\gamma$ was assumed along the surface AB. This was considered to be a reasonable step, because in the physical problem the boundary conditions given by Eq. (5.13) will be perturbed by the initial preflow sinkage of the punch, and the slight overburden then added along AB will provide a source for this pressure. The pressure assumed corresponds to an initial sinkage of the order of $10^{-2}R$ where the thin overburden has no strength. The resulting fields of characteristics and pressure distributions under the punch for angles of friction varying from 20°-45° are shown in Figures 5-10 through 5-15. The computer program as written in the Michigan Algorithm Decoder (MAD) language, is given in a previous report.[39]

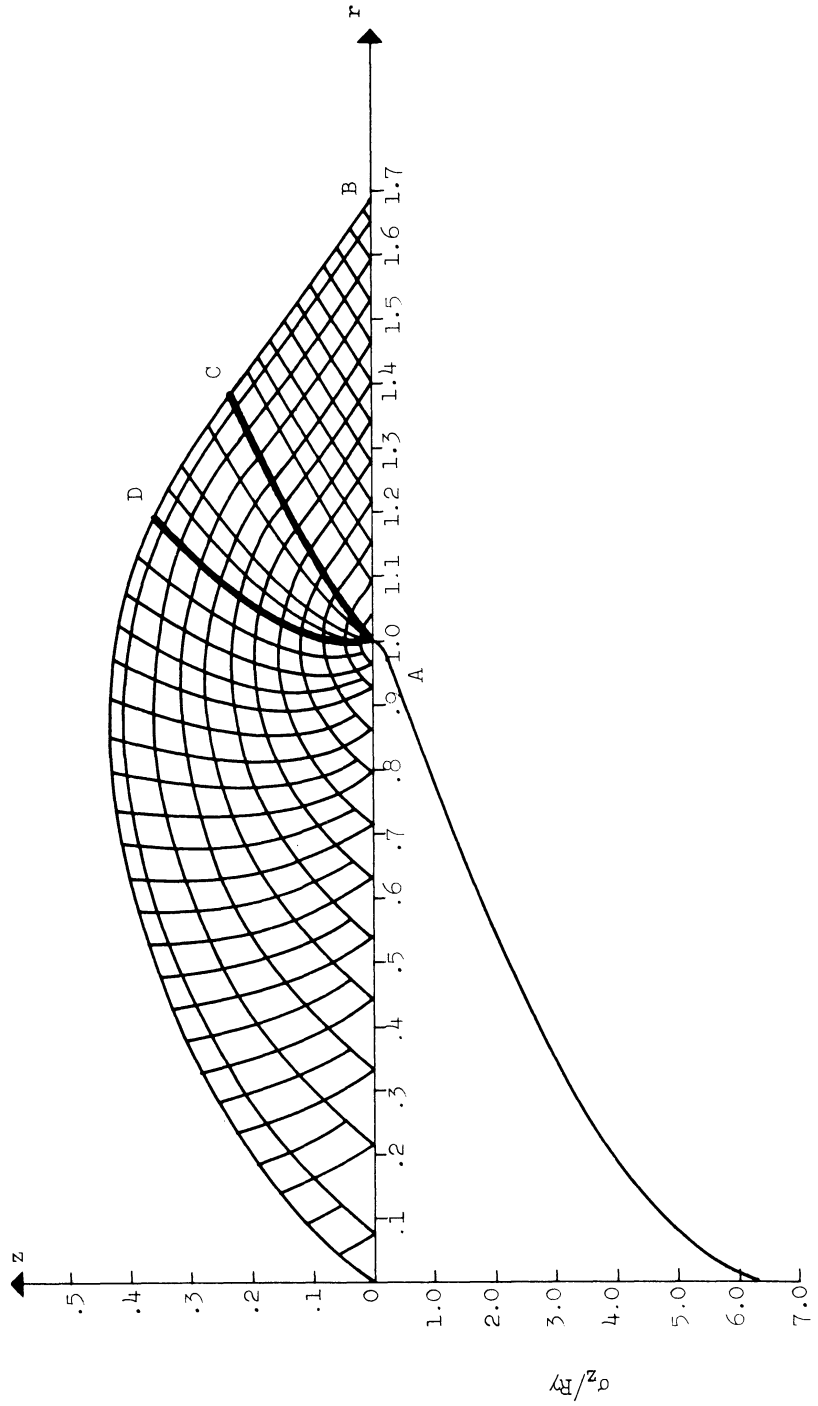

Figure 5-10. Stress characteristics and punch pressure distribution for $\phi = 20°$.

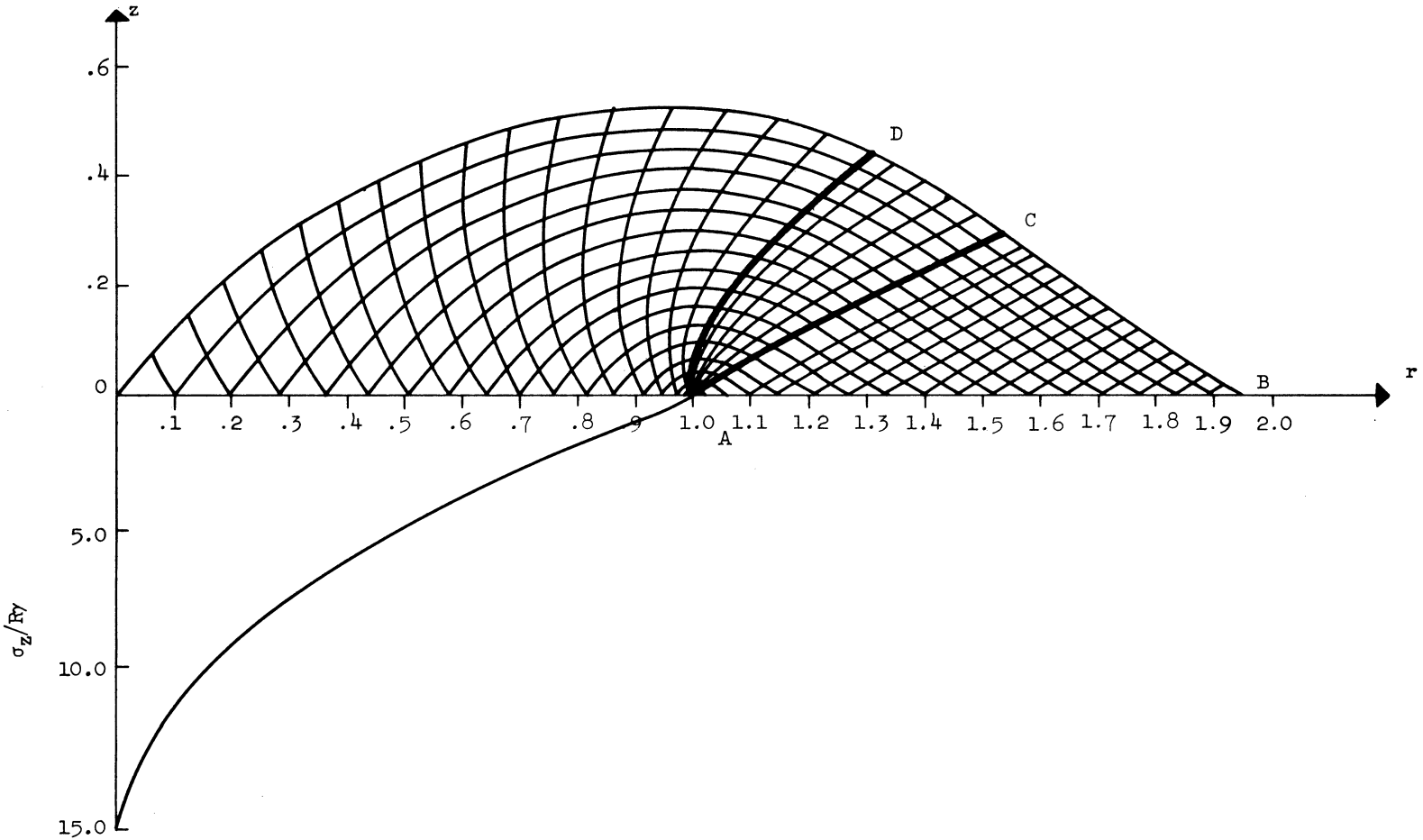

Figure 5-11. Stress characteristics and punch pressure distribution for $\phi = 25°$.

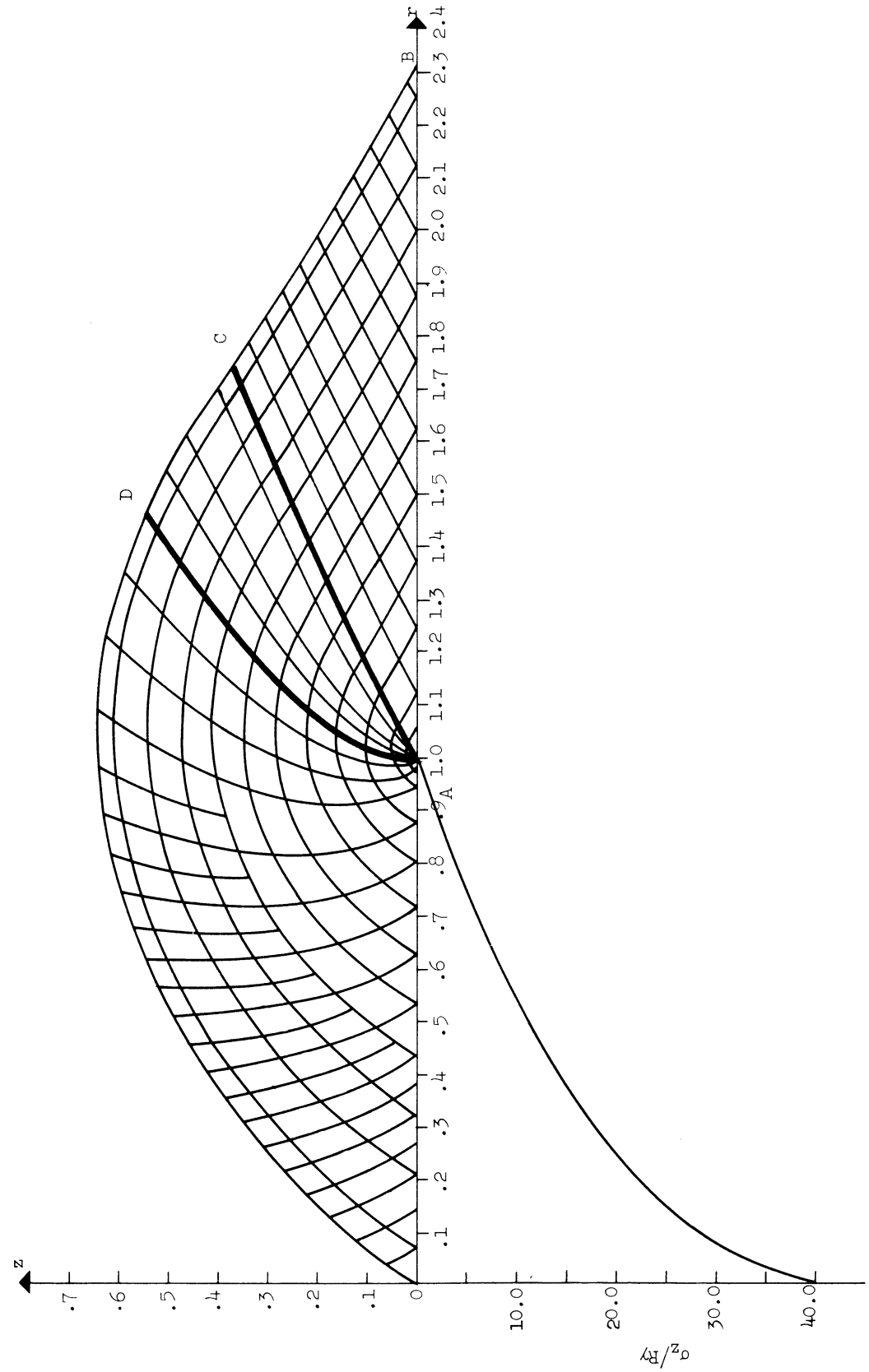

Figure 5-12. Stress characteristics and punch pressure distribution for $\phi = 30°$.

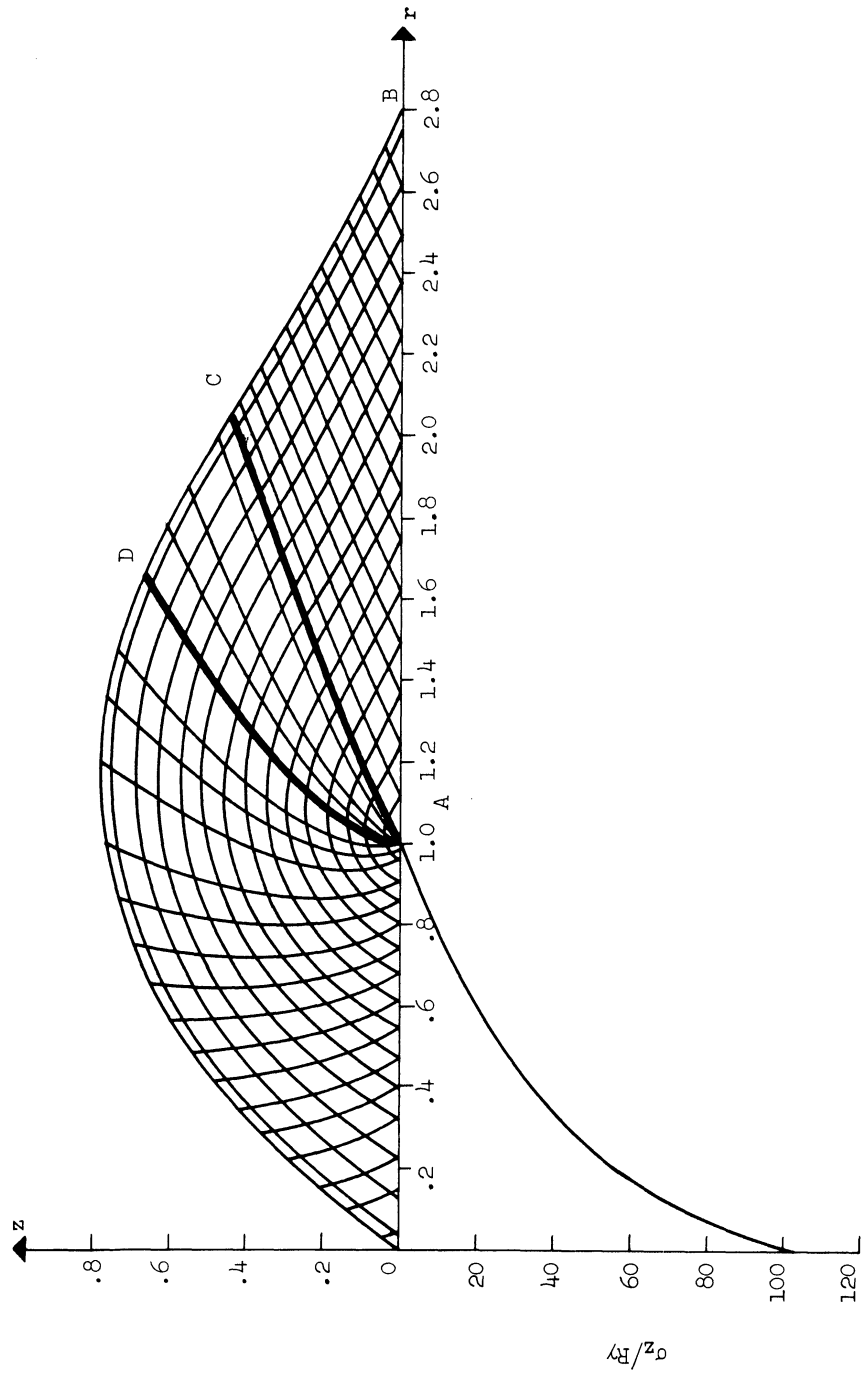

Figure 5-13. Stress characteristics and punch pressure distribution for $\phi = 35°$.

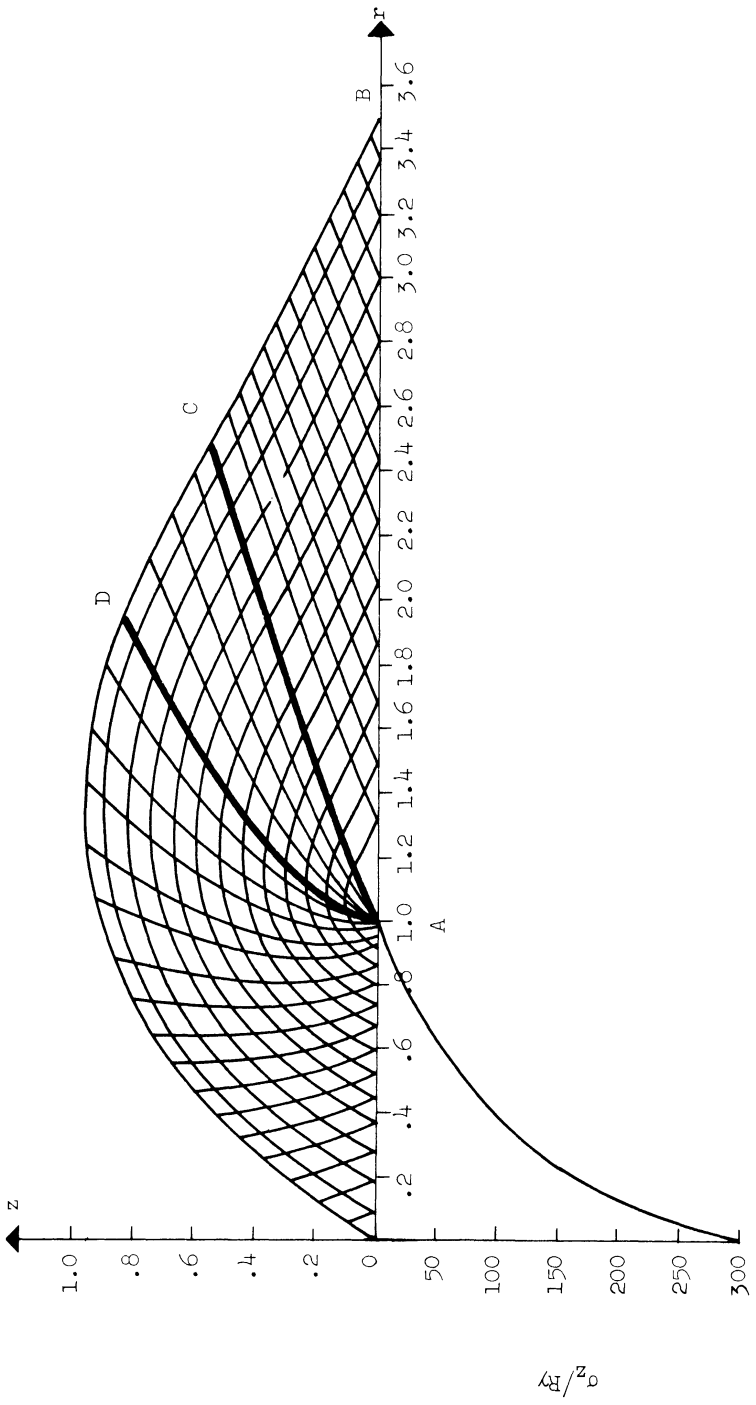

Figure 5-14. Stress characteristics and punch pressure distribution for $\phi = 40°$.

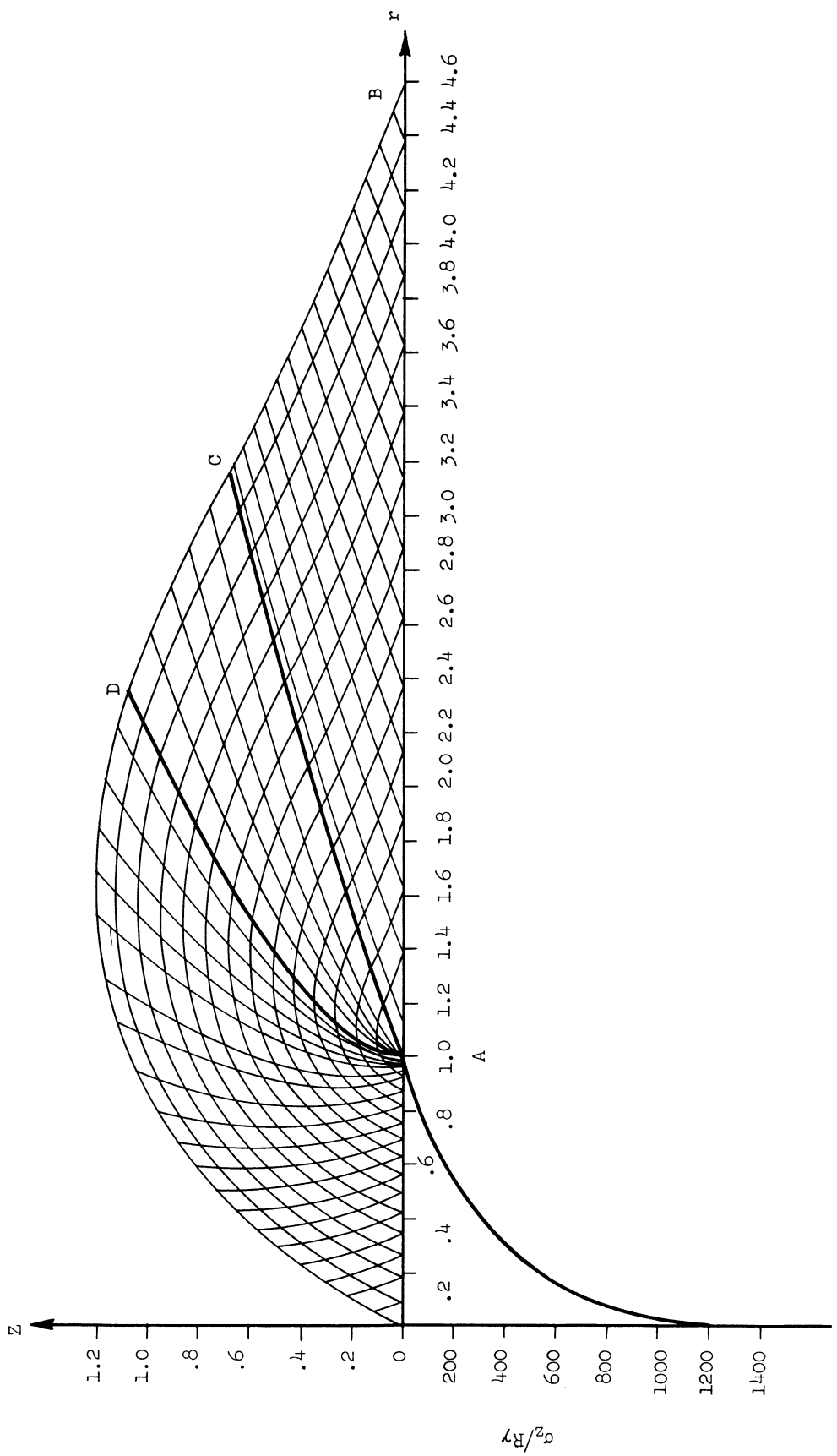

Figure 5-15. Stress characteristics and punch pressure distribution for $\phi = 45°$.

An overall equilibrium check equating the resisting forces acting on the outer second characteristic to the combined forces from the soil weight and from the punch pressure was made for the $\phi = 30°$ case. The error in vertical equilibrium amounted to less than 0.4% of the punch load.

2. Velocity Field

As a first step in finding a possible velocity field, the extent of the deforming region must be assumed. The boundary line separating the deforming region from the rigid region must be determined from the strain rate state in the material adjacent to the rigid region. Using the notation of Figure 5-16, the occurrence of a tangential velocity

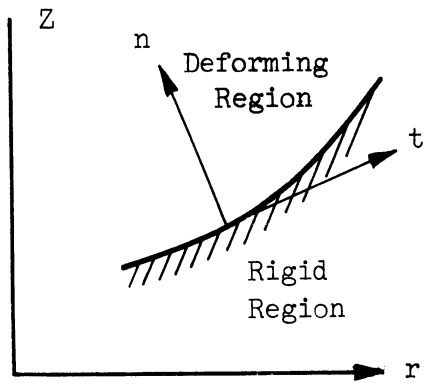

Figure 5-16. Boundary of rigid and deforming regions.

discontinuity will cause a strain rate state in which $\dot{\epsilon}_{tt}$ and $\dot{\epsilon}_{\theta}$ are both negligible compared to $\dot{\gamma}_{nt}$. If no velocity discontinuities occur, then the continuity requires

$$\dot{\epsilon}_{\theta} = \dot{\epsilon}_{tt} = 0$$

in the region immediately adjacent to the rigid zone; but it can be seen that $\dot{\epsilon}_{nn}$ and $\dot{\gamma}_{nt}$ can be nonzero. Therefore, whether a velocity discontinuity is occurring or not, plane strain conditions occur in the material adjacent to the rigid region, and the strain rate state is identical to that occurring along a velocity characteristic in the plane strain case. Hence the rigid and deforming regions are separated by a velocity characteristic, and the velocity discontinuities are related by Eq. (4.7). Since the deforming region must extend the full width of the punch, the smallest deforming region is that contained within the r-axis and the second velocity characteristic which passes through the origin. This is the axially symmetric analogy to Hill's velocity field for the same problem for the plane strain case.[37]

The velocity characteristics are uniquely determined in this deforming region from the stress characteristics by Eq. (4.37) for any permissible values of Ω and α. Three such fields of velocity characteristics are shown in Figures 5-17 through 5-19 for the case of $\phi = 30°$, zero dilatation ($\Omega = 1$, $\kappa = \pi/4$) and different values of α. These fields of velocity characteristics were constructed graphically from the stress characteristics.

As anticipated, the extent of the deforming zone is quite sensitive to α, as can be seen in Figures 5-17, 5-18, and 5-19. Similar velocity fields were drawn from the stress characteristics shown in Figures 5-10 through 5-15. The resulting ratios of OB'/OA, OB"/OA,

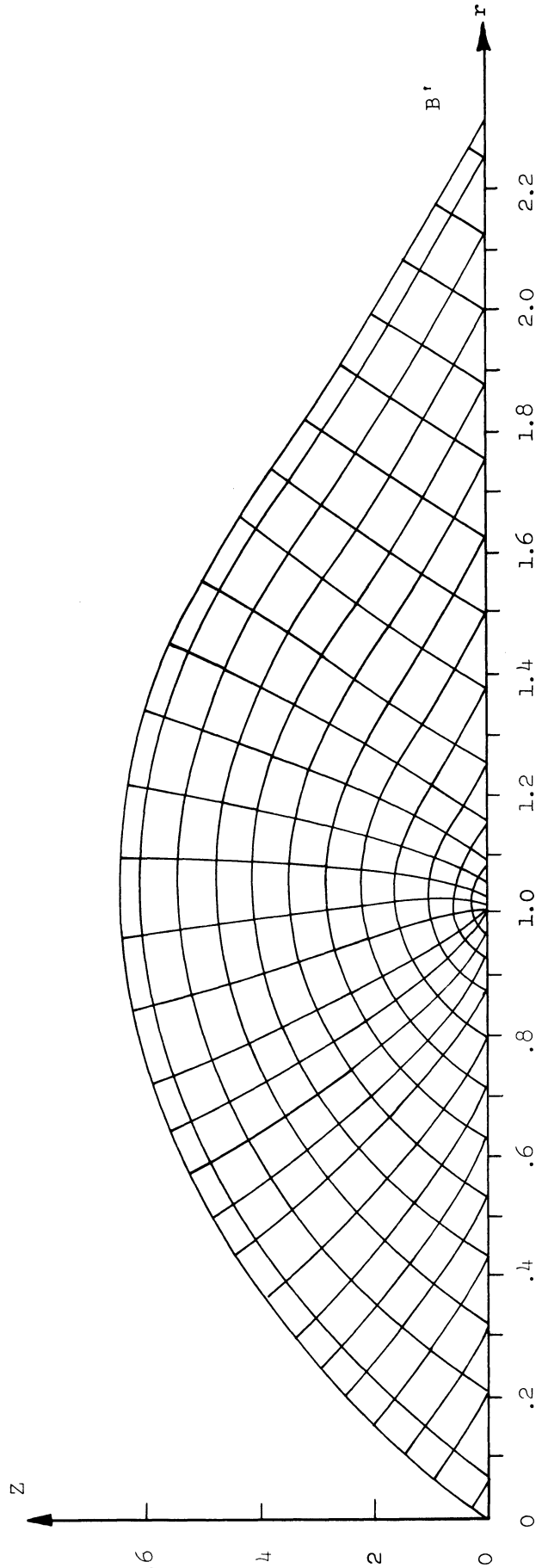

Figure 5-17. Velocity characteristics for $\phi = 30°$, zero dilatation rate, and coincidence of second stress and velocity characteristics.

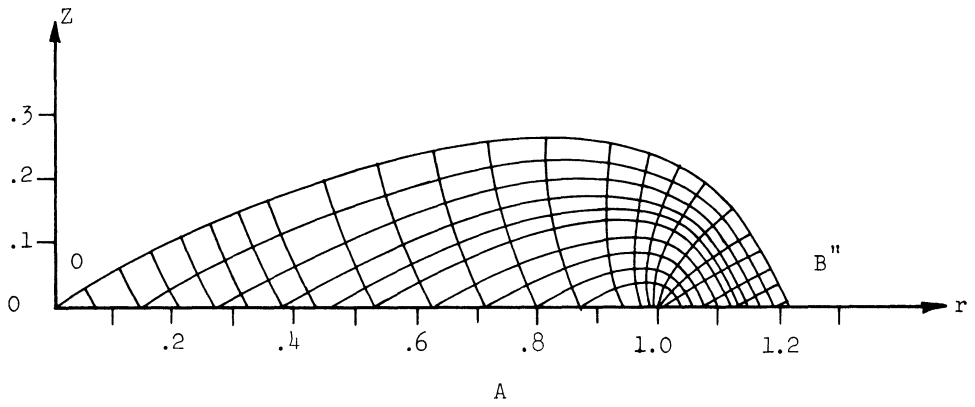

Figure 5-18. Velocity characteristics for $\phi = 30°$, zero dilatation rate, and coincidence of first stress and velocity characteristics.

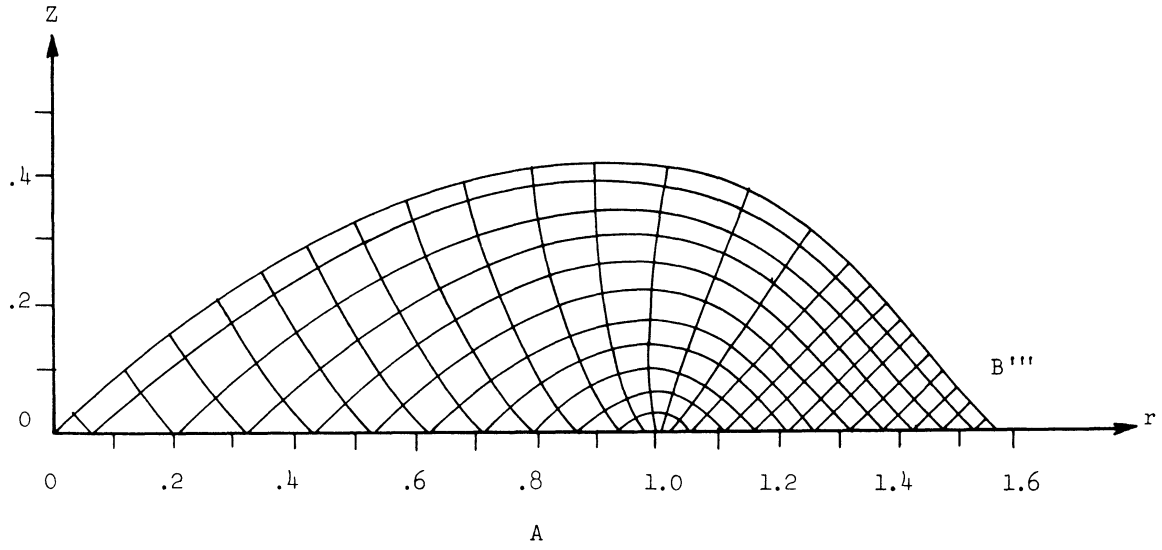

Figure 5-19. Velocity characteristics for $\phi = 30°$, zero dilatation rate, and coincidence of the principal directions of stress and strain rate.

and OB"'/OA were plotted in Figure 5-20 and a smooth curve was drawn through the points. In like manner, the average punch pressure was computed and presented in Figure 5-21. As noted in Figure 5-20, OB'/OA will not change for dilatation rates within the restrictions of Eq. (4.8a) because the second velocity characteristic, which forms the boundary of the deforming region, coincides with the second stress characteristic for this case. However, the ratios OB"/OA and OB"'/OA will change with the dilatation rate. For the usual case of a positive dilatation rate it can be seen from Figures 5-18 and 5-19 that both of these ratios will increase.

When the velocity characteristics have been found, the velocities in the deforming region can be determined by integrating Eqs. (4.38) along the velocity characteristics. The boundary conditions on the velocity field require constant normal velocity directly under the punch, by Eq. (5.9b). In addition, the velocities along the outer second characteristic are related by Eq. (4.7) since plane strain flow occurs along this characteristic. Written in terms of the velocity components u and w, Eq. (4.7) requires that

$$\frac{u}{w} = -\tan(\nu+\kappa) \tag{5.22}$$

along the outer velocity characteristic. Substitution of Eq. (5.22) into Eq. (4.38b) yields

Curve A: Coincidence of second stress and velocity characteristics.
Curve B: Coincidence of principal stress and strain rate directions.
Curve C: Coincidence of first stress and velocity characteristics.

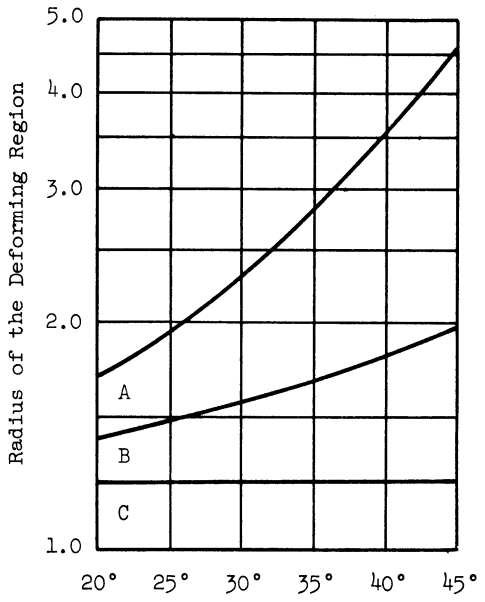

Figure 5-20. Variation of the deforming region with angle of friction.

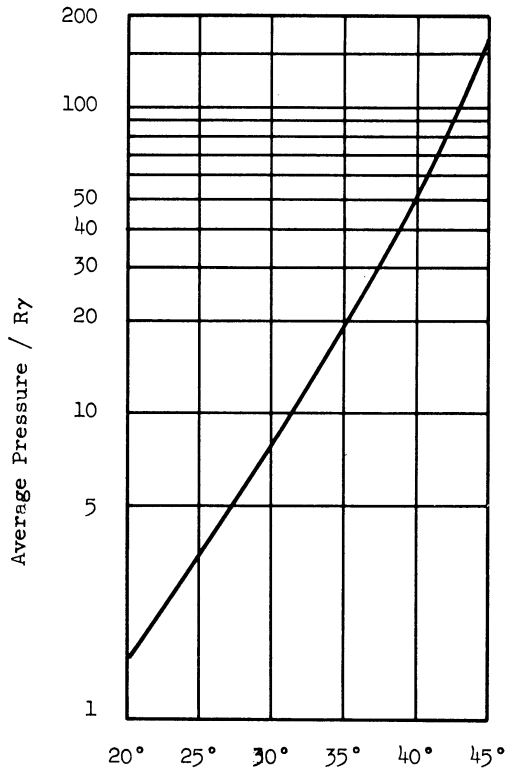

Figure 5-21. Variation of the average pressure with angle of friction.

$$\frac{dw}{dr}\sin 2\kappa + w\left[\frac{d\nu}{dr}\frac{\cos(\nu-\kappa)}{\cos(\nu+\kappa)} + \frac{1}{r(1+\Omega^{\overline{w}})}\frac{\sin(\nu+\kappa)}{\cos(\nu-\kappa)}\right] = 0 \qquad (5.23)$$

It is seen that when $w \neq 0$ the second term approaches positive infinity as the origin of the coordinates is approached. This means that dw/dr must correspondingly approach negative infinity. This will require w to be infinity at the origin, approached along the outer characteristic. In order to avoid this, u and w are set equal to zero along the characteristic separating the rigid and deforming regions.

Since dilatation is expected to occur in the actual tests, some theoretical velocity solutions are necessary in order to estimate the degree of dilatation. For comparison purposes the velocity field for the perfect plasticity case will be computed. For this case $\Omega = \tan^2(\pi/4+\phi/2)$ from Eq. (3.27) and hence $\kappa = \pi/4-\phi/2$ from Eq. (4.35). The velocity characteristics coincide with the stress characteristics by Eq. (4.37) and Eqs. (4.38) on the first characteristics become,

$$\cos\eta\, du + \sin\eta\, dw + \frac{(1-\sin\phi)}{\cos\eta}\, u\, \frac{dr}{2r} = 0 \qquad (5.24a)$$

and on second characteristics,

$$\sin(\eta+\phi)du - \cos(\eta+\phi)dw + \frac{(1-\sin\phi)}{\sin(\phi+\eta)}\, u\, \frac{dr}{2r} = 0 \qquad (5.24b)$$

A numerical integration of these equations can be accomplished by approximating them by finite difference equations. Similar to the

method of computing the stress characteristics, the solution is marched out from a known boundary. The usual stiuation is shown in Figure 5-9. The characteristics themselves are known from the stress solution and the velocities u and w are known at two intersections P, Q of the characteristics. It is desired to find the velocities at the point 1. The two differential equations are approximated by the finite difference equations

$$\cos\left(\frac{\eta_1+\eta_p}{2}\right)(u_1-u_p)+\sin\left(\frac{\eta_1+\eta_p}{2}\right)(w_1-w_p) + \frac{(1-\sin\phi)}{2\cos\left(\frac{\eta_1+\eta_p}{2}\right)}(u_1+u_p)\left(\frac{r_1-r_p}{r_1+r_p}\right) = 0 \tag{5.25a}$$

$$\sin\left(\phi+\frac{\eta_1+\eta_Q}{2}\right)(u_1-u_Q)-\cos\left(\phi+\frac{\eta_1+\eta_Q}{2}\right)(w_1-w_Q)$$

$$+ \frac{(1-\sin\phi)}{2\sin\left(\phi+\frac{\eta_1+\eta_Q}{2}\right)}(u_1+u_Q)\left(\frac{r_1-r_Q}{r_1+r_Q}\right) = 0. \tag{5.25b}$$

These equations are then solved for u_1 and w_1

$$u_1 = \frac{\begin{array}{l} w_p - w_Q + u_p\left[\cot\left(\frac{\eta_1+\eta_p}{2}\right) - \frac{(1-\sin\phi)}{\sin 2\left(\frac{\eta_1+\eta_p}{2}\right)}\left(\frac{r_1-r_p}{r_1+r_p}\right)\right] \\ +u_Q\left[\tan\left(\phi+\frac{\eta_1+\eta_Q}{2}\right) - \frac{(1-\sin\phi)}{\sin 2\left(\phi+\frac{\eta_1+\eta_Q}{2}\right)}\left(\frac{r_1-r_Q}{r_1+r_Q}\right)\right] \end{array}}{\cot\left(\frac{\eta_1+\eta_p}{2}\right) + \tan\left(\phi+\frac{\eta_1+\eta_Q}{2}\right) + \frac{(1-\sin\phi)}{\sin 2\left(\frac{\eta_1+\eta_p}{2}\right)}\left(\frac{r_1-r_p}{r_1+r_p}\right) + \frac{(1-\sin\phi)}{\sin 2\left(\phi+\frac{\eta_1+\eta_Q}{2}\right)}\left(\frac{r_1-r_Q}{r_1+r_Q}\right)} \tag{5.26a}$$

$$w_1 = \frac{1}{\tan\left(\frac{\eta_1+\eta_p}{2}\right)+\cot\left(\phi+\frac{\eta_1+\eta_Q}{2}\right)}\left[w_p\tan\left(\frac{\eta_1+\eta_p}{2}\right)+w_Q\cot\left(\phi+\frac{\eta_1+\eta_Q}{2}\right)\right.$$

$$+ u_1\left[\frac{(1-\sin\phi)}{2\sin^2\left(\phi+\frac{\eta_1+\eta_Q}{2}\right)}\left(\frac{r_1-r_Q}{r_1+r_Q}\right)-\frac{(1-\sin\phi)}{2\cos^2\left(\frac{\eta_1+\eta_p}{2}\right)}\left(\frac{r_1-r_p}{r_1+r_p}\right)\right]$$

$$+u_p\left[1-\frac{(1-\sin\phi)}{2\cos^2\left(\frac{\eta_1+\eta_p}{2}\right)}\left(\frac{r_1-r_p}{r_1+r_p}\right)\right]$$

$$\left.- u_Q\left[1-\frac{(1-\sin\phi)}{2\sin^2\left(\phi+\frac{\eta_1+\eta_Q}{2}\right)}\left(\frac{r_1-r_Q}{r_1+r_Q}\right)\right]\right]. \qquad (5.26b)$$

The numerical solution begins by setting the velocity components to zero along the outer second characteristic in accordance with the boundary conditions. Then the computations are stated at the straight boundary OA under the punch. Along this boundary the vertical velocity is the constant w_o from Eq. (5.9b). The radial velocity must be found by integrating along a first characteristic. This is done numerically by solving Eq. (5.25a) for u_1

$$u_1 = \frac{u_p\left[1-\frac{(1-\sin\phi)}{2\cos^2\left(\frac{\eta_1+\eta_p}{2}\right)}\left(\frac{r_1-r_p}{r_1+r_p}\right)\right]-(w_o-w_p)\tan\left(\frac{\eta_1+\eta_p}{2}\right)}{1+\frac{(1-\sin\phi)}{2\cos^2\left(\frac{\eta_1+\eta_p}{2}\right)}\left(\frac{r_1-r_p}{r_1+r_p}\right)} .$$

After this step, the velocities are computed along the entire second characteristic by repeated use of Eqs. (5.26). This procedure is continued until the velocity field is completely determined. This numerical integration technique was programmed on the digital computer. The vertical surface velocities for the cases of ϕ = 20° and 30° are shown in Figures 5-22 and 5-23, respectively. The very large velocities predicted casts further doubt on the validity of the perfect plasticity theory even for initial plastic flow. The volume change per unit punch displacement for three angles of friction are shown in Table III.

TABLE III

VOLUME CHANGE PER UNIT PUNCH DISPLACEMENT FOR PERFECT PLASTICITY

ϕ	$\frac{\Delta Vol}{R^2 w_o}$
20°	39
30°	190
41°	2400

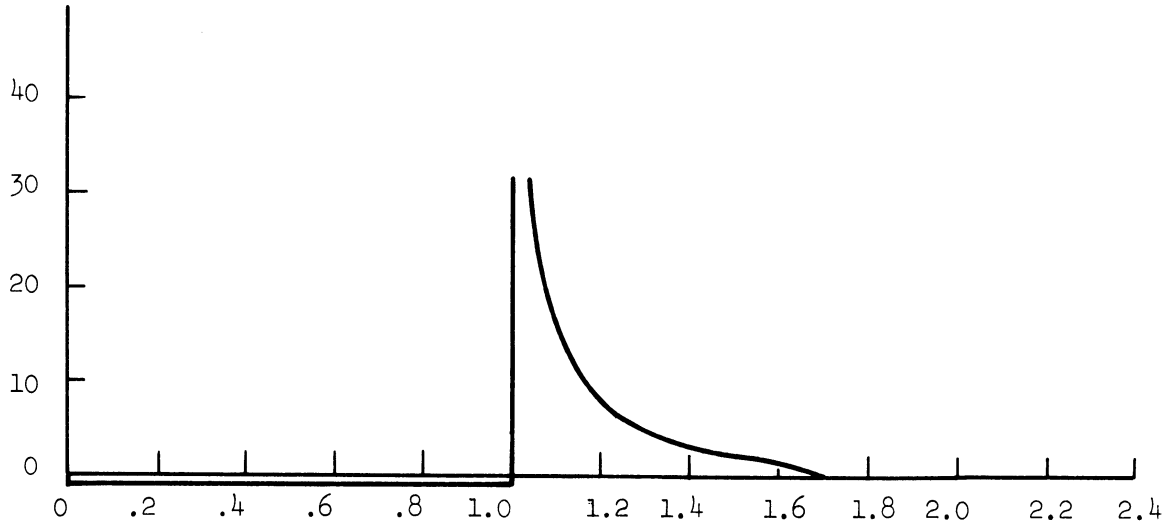

Figure 5-22. Vertical surface velocities by perfect plasticity theory (ϕ = 20°).

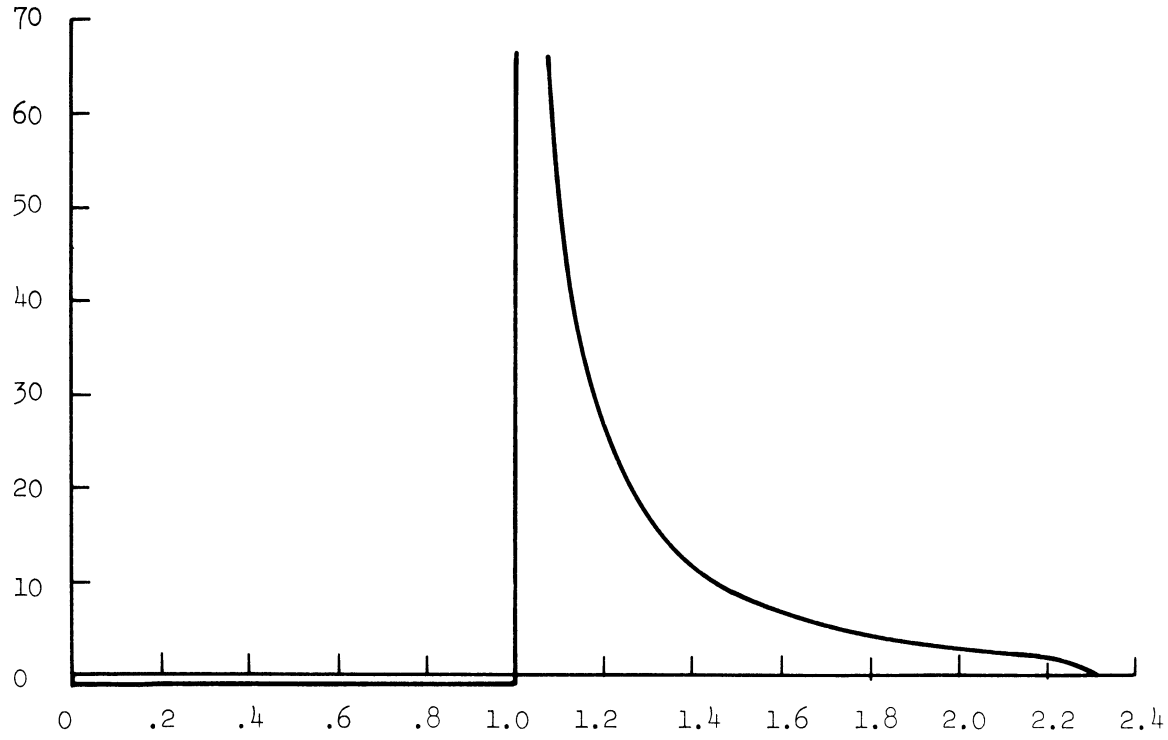

Figure 5-23. Vertical surface velocities by perfect plasticity theory (ϕ = 30°).

CHAPTER VI

THE EXPERIMENTAL INVESTIGATION

Having selected a problem with an appropriate velocity observable and having made certain theoretical predictions from which the experimental data can be interpreted, the next step in order is to reproduce this test as accurately as possible in the laboratory. Although the circular surface footing test is of great practical interest and the load-sinkage relation has been investigated in many experimental programs, little or no attention has been given to velocity fields. For this reason, a review of the experimental work of previous investigators will not be included.

The material tested was a uniform Ottawa sand in the air dry condition. The material was graded such that 98% passed the No. 20 sieve and 97% was retained on the No. 40 sieve (ASTM). The material was primarily quartz, so a nominal specific gravity of 2.65 was chosen for use in the calculations. A series of standard triaxial tests were performed to determine the maximum angle of friction of the material. The test points and the smooth curve drawn through them are shown in Figure 6-1 where the angle of friction is plotted as a function of the initial void ratio. The low void ratios were achieved by dropping the sand into the specimen mold from a height of about 14 inches. The other

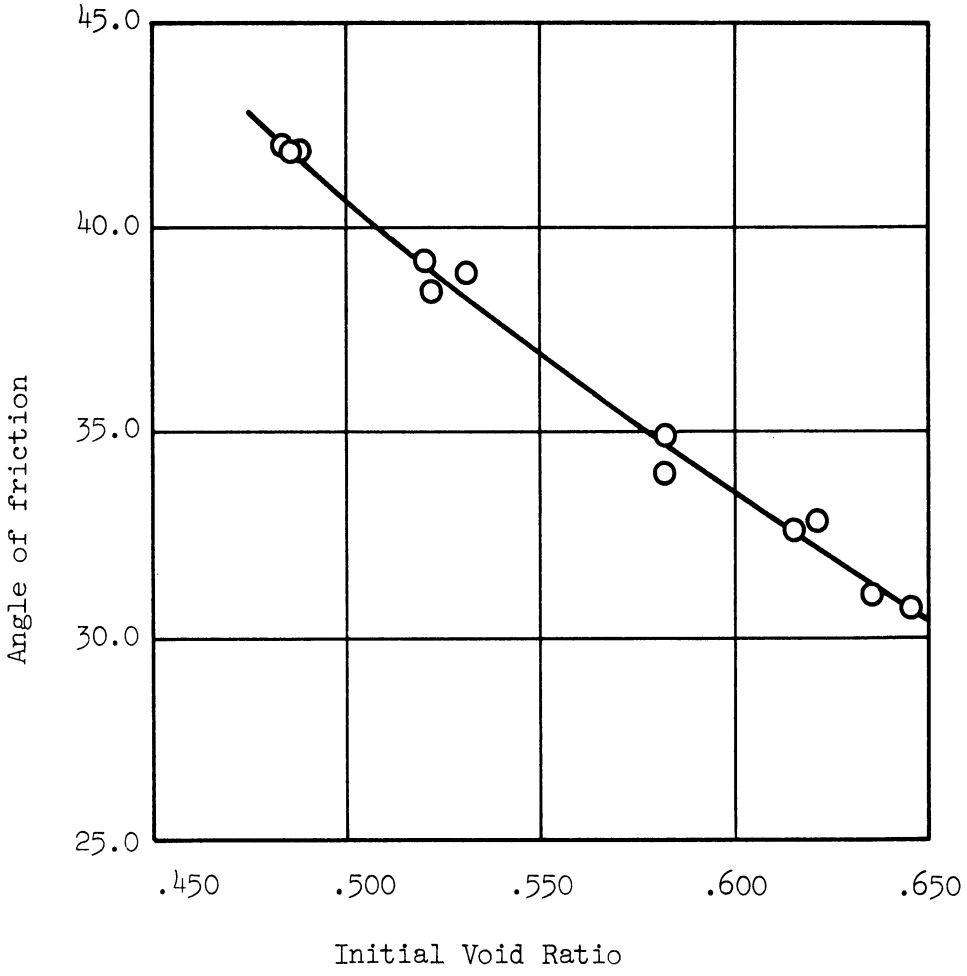

Figure 6-1. Angle of friction as a function of the initial void ratio.

void ratios were obtained by depositing the material in layers under essentially zero drop height conditions and compacting each layer with a piston-like tamper.

The test bin for the footing or punching tests measured 12 inches inside diameter and 4 inches in depth. It was cut from a standard aluminum pipe with 3/8-inch thickness walls. The bin was mounted on a turntable driven by an electric motor and controlled through a variable speed reducer. It was slowly rotated during filling in order to facilitate the preparation of homogeneous and consistent specimens. The specimens were prepared in a manner similar to that used in the triaxial tests. For the very dense specimens the sand was showered into the bin from a height of 18 inches. The showering device was a 10-inch diameter perforated pan filled by gravity flow from a 14-quart hopper. This device was raised during filling of the bin in order to maintain a constant drop height, and it was adjusted so that the surface of the sand specimen was quite level. This specimen preparation apparatus is shown in Figure 6-2. The specimens of looser density were obtained by hand filling the bin in layers and compacting each layer by tamping with a 45-pound weight. In all cases the surface was given a final leveling with a 12-inch diameter plate piston to which vertical pressure was applied by hand. With this piston in place, the average height of the sample was measured with a depth gauge using the edge of the bin as the reference. With this measurement, the average area of the bin, and the

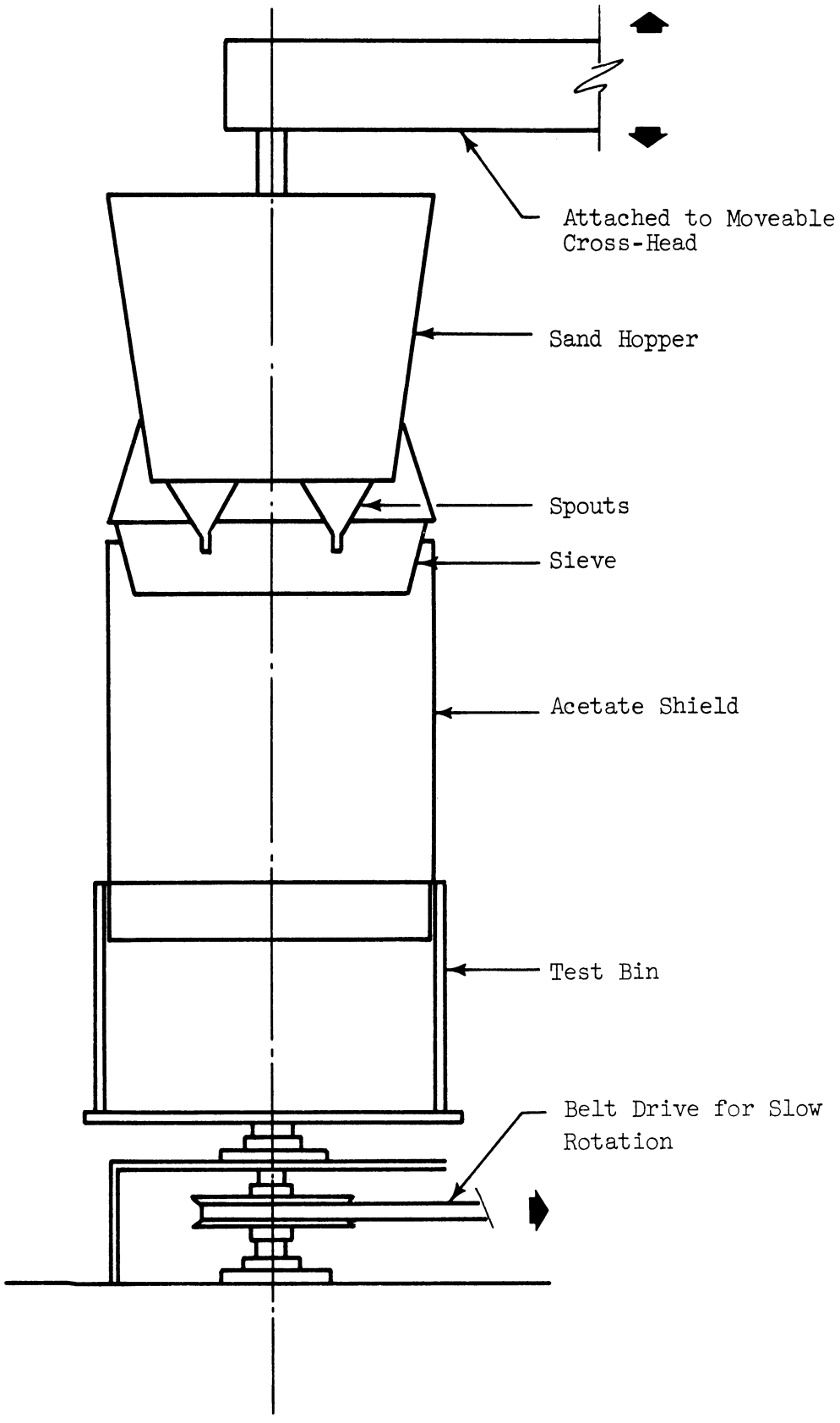

Figure 6-2. Specimen preparation apparatus.

weight of the sand, the average void ratio was computed and the angle of friction was found from Figure 6-1 for each test.

The circular punch was machined to 2.4 inches in diameter and 3 inches in length from a piece of cold-rolled steel bar stock. In order to approximate the frictionless punch condition as closely as thought to be practical, a disc of commercial grade, double-strength glass was obtained and fastened to the base of the punch. Sliding-block type of tests were conducted to determine the maximum friction between glass and sand. The results of two series of tests are shown in Figure 6-3. The limiting angle of friction was found to be about 7.5° or less. The punch was rigidly fastened in series with a Baldwin load cell by means of a threaded joint. The load cell in turn was rigidly attached to the loading head. A cursory check of the calibration by means of calibration weights indicated that the load cell was accurate to within 0.1 pound which was as close as the load indicator dial could be read. The punch displacement was measured to the nearest 0.001 inch by a machinist's dial gauge. The loading rate used for the tests was 0.018 inch/minute.

The sequence of surface displacements during a punch test was recorded by photographing dyed grains of sand spaced at equal intervals along a diameter of the specimen surface. A camera equipped with a dropping front enabled the surface to be photographed without reducing the vertical scale. The photographs were subsequently enlarged and measurements of the surface displacements were taken.

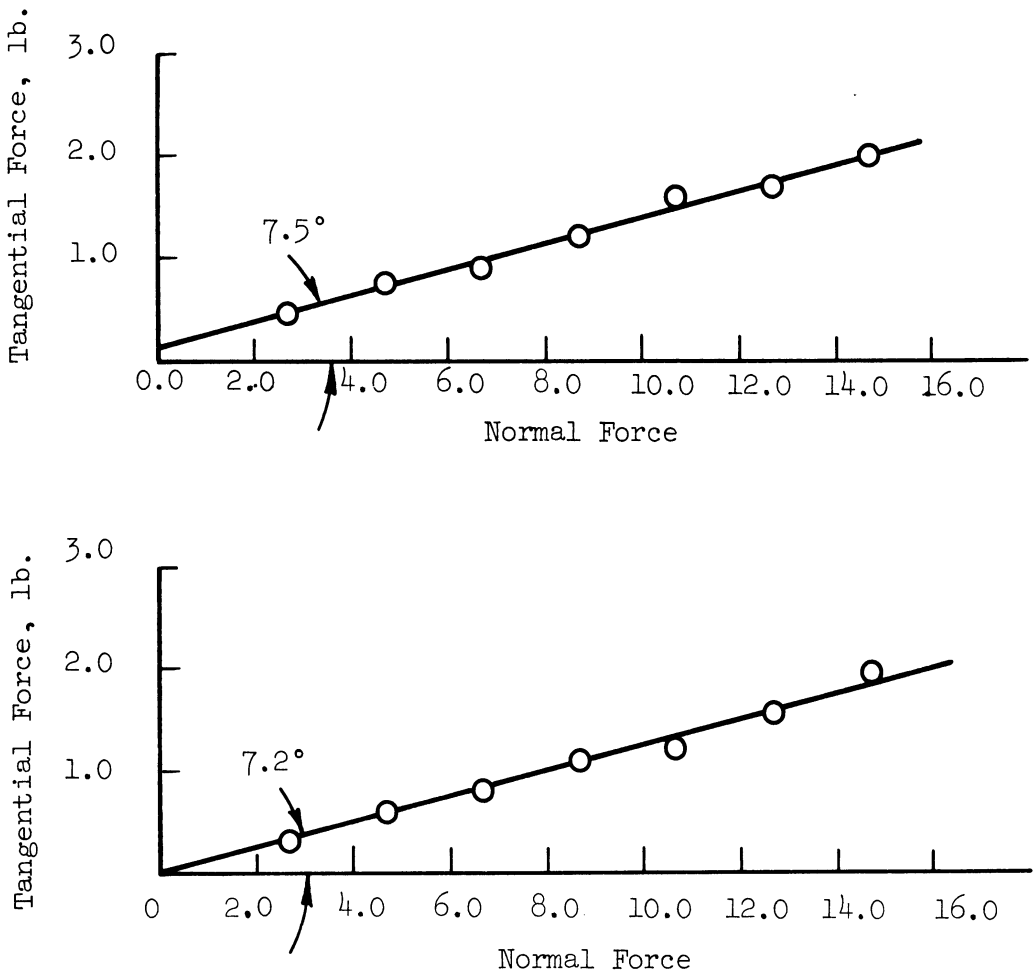

Figure 6-3. The limiting friction between Ottawa sand and glass.

Load-deflection curves and corresponding surface profiles are shown in Figures 6-4 through 6-6 for different specimen densities. Generally, the tests on dense specimens exhibited a peak or maximum load which was chosen as the yield load, whereas the loose specimens exhibited a gradually increasing load-deflection curve which sometimes became quite level as in Figure 6-6. In this case, in accordance with Terzaghi,[40] the failure load was considered to be the load at the point where the curve passes into the fairly straight portion.

The average failure pressures from the tests are plotted in Figure 6-7 on which the theoretical curve from Figure 5-21 is also shown for purposes of comparison. Except for the tests on the very dense specimens where ϕ is about 40°, the theory badly underestimates the actual failure pressures. One of the contributors to the actual strength is the initial indentation or sinkage prior to total yielding. The effects of this indentation on the theoretical bearing pressure was approximated by the addition of a surcharge equal to the weight of the thin overburden. The stress characteristics and the pressure distribution was recomputed for different surcharges or indentations for the case where $\phi = 30°$. The results are shown in Figure 6-8. The order of magnitude increase in the surcharge from $10^{-2}R\gamma$ to $10^{-1}R\gamma$, which is a more realistic value according to the test results, gives a 50% increase in the bearing pressure. However, the increase is only 23% for the same increase in surcharge when $\phi = 40°$. The bearing pressures are

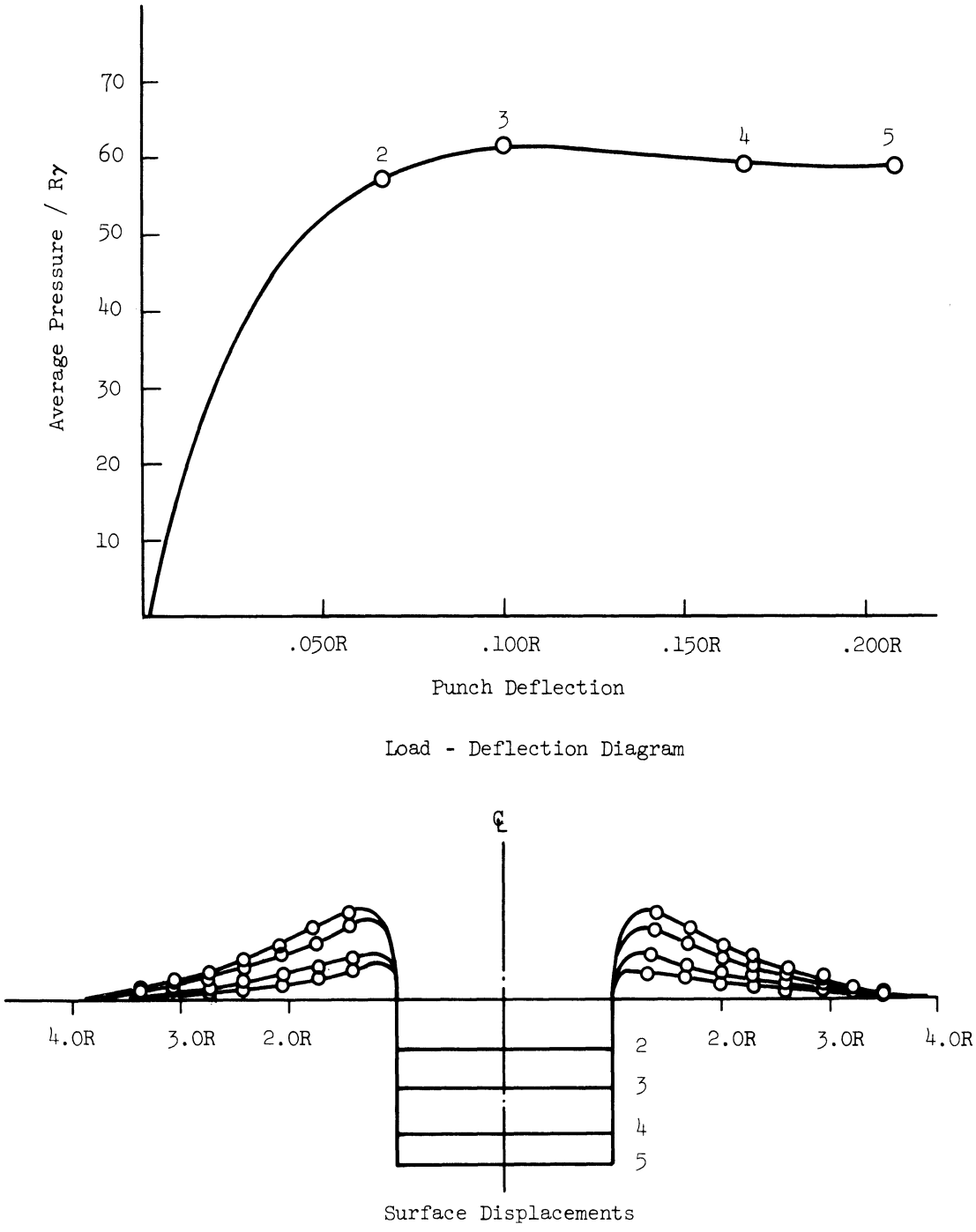

Figure 6-4. Typical indentation test results for a very dense specimen (ϕ = 42°).

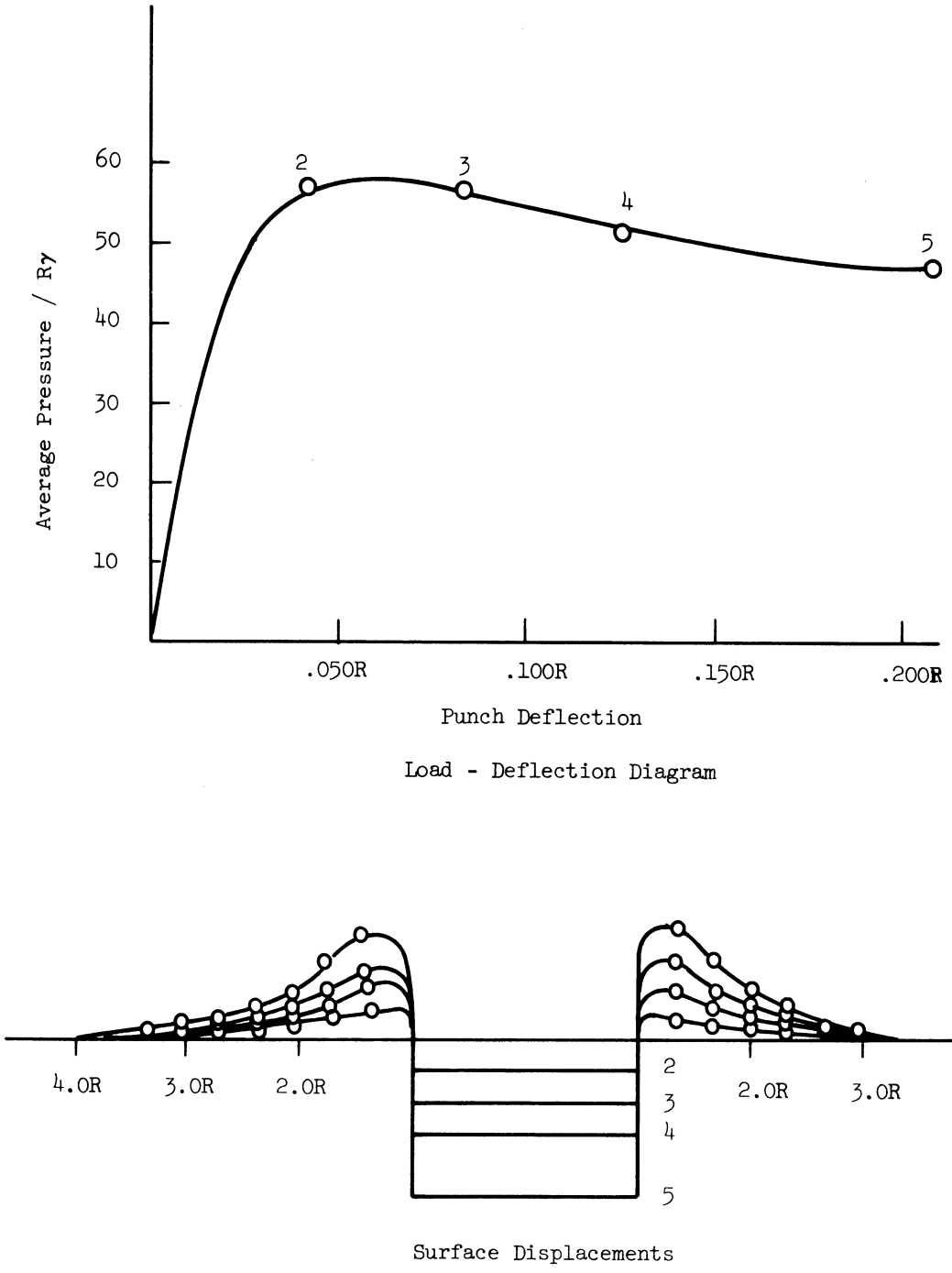

Figure 6-5. Typical indentation test results for a medium dense specimen ($\phi = 39°$).

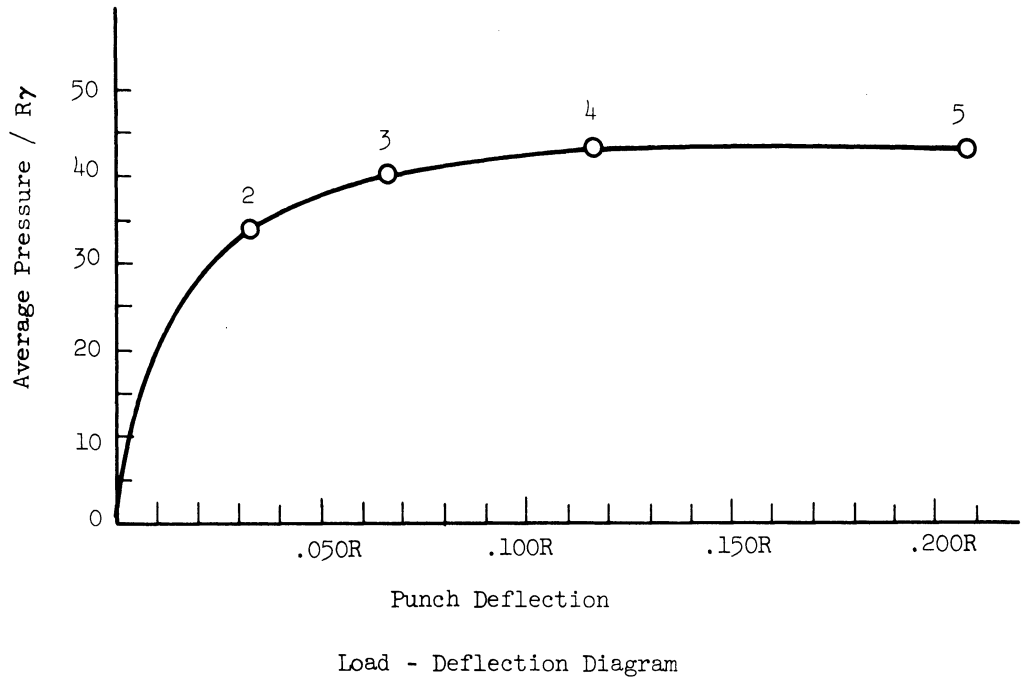

Load - Deflection Diagram

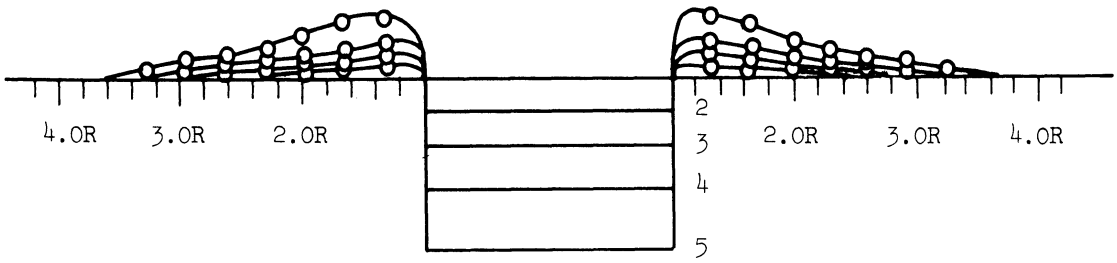

Surface Displacements

Figure 6-6. Typical indentation test results for a loose specimen ($\phi = 34°$).

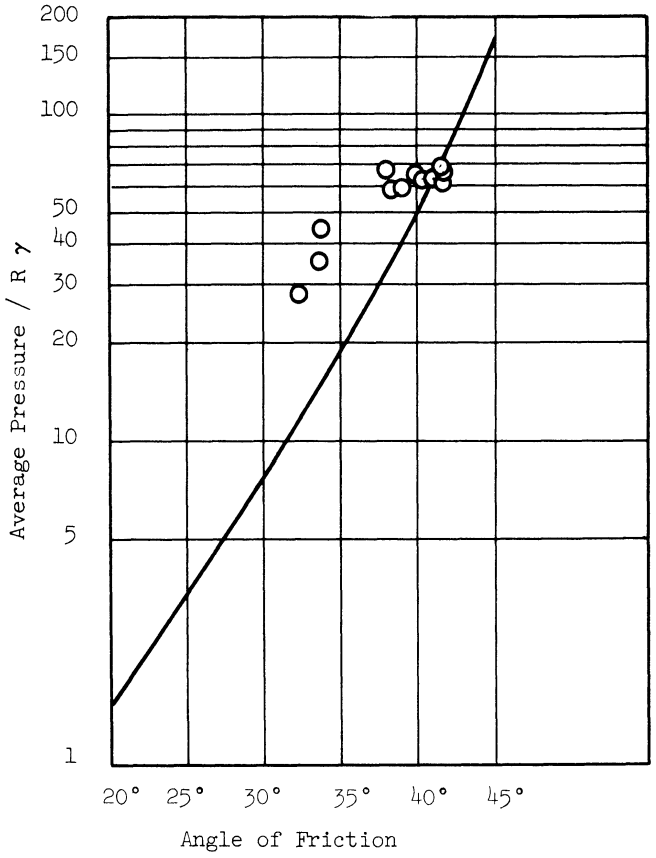

Figure 6-7. Average failure pressures for circular punch indentation tests.

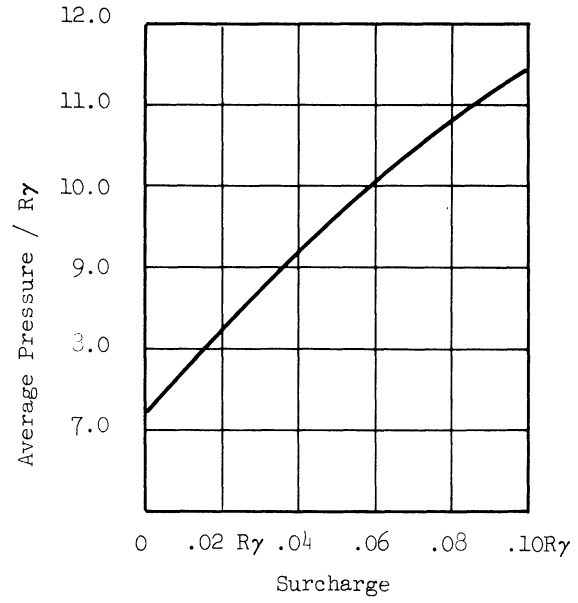

Figure 6-8. Variation of the theoretical punch pressure with surcharge for the case $\phi = 30°$.

expected to be decreasingly affected by the surcharge for increasing angle of friction because the inherent bearing capacity increases with the angle of friction. Thus it has been shown that the theoretical problem is of such a nature that the bearing pressures are quite sensitive to small changes in the geometrical configuration. This is neither an expected nor a satisfying result. While such corrections can explain the reasons for the larger actual bearing pressures at the lower angles of friction, they would cause an overestimation of some 20% or more of the actual bearing pressures on the specimens where ϕ is about 40°. The reason for this can only be speculated.

Since the actual yield load is better approximated by the theoretical solution for angles of friction around 40°, more attention concerning the velocities was focused on tests at these densities. Consider the dilatations first. An expansion rate was observed in every test. The maximum dilatations per unit deflection computed from the photographs of the surface displacements for each test are plotted in Figure 6-9 along with the theoretical results from Table III. It can be seen that the actual dilatation rate was never more than 3% and was usually less than 1% of that by the perfect plasticity theory. Hence as far as the flow rule is concerned, the material was essentially volume conserving.

In all instances the observed deforming region expanded with increasing punch displacement and,as in the case of selecting the failure load, the radius of the deforming region at failure is somewhat ar-

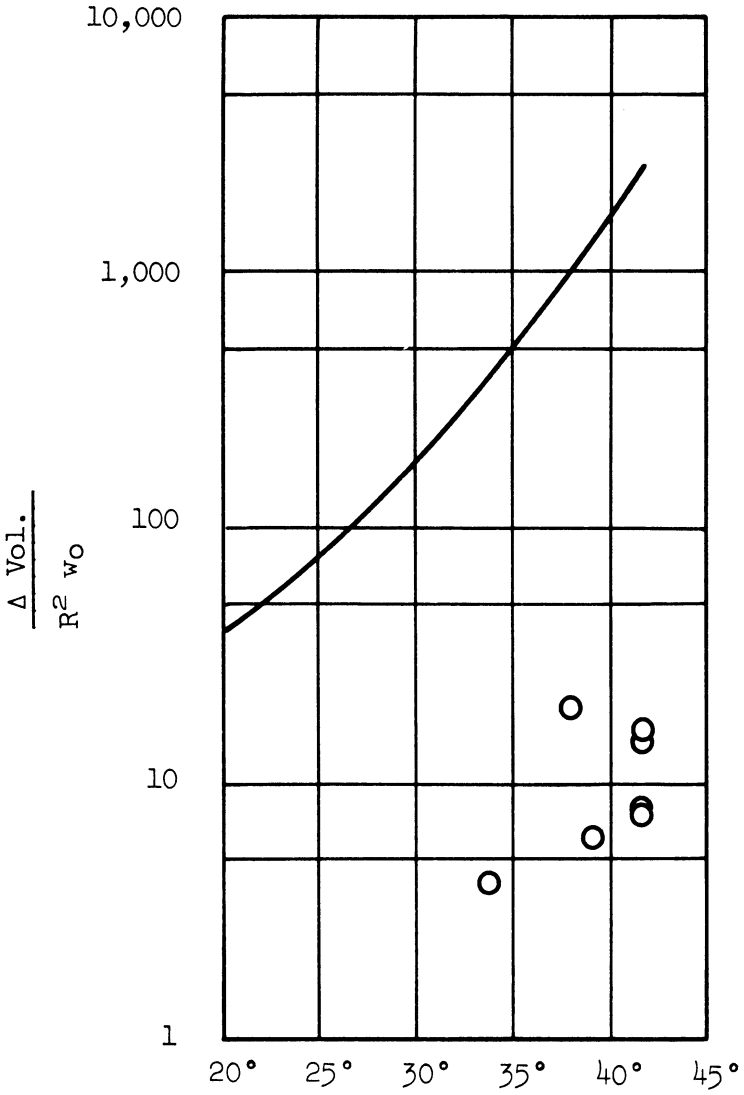

Figure 6-9. Experimental observations of the dilation rate in circular punch indentation tests.

bitrary. It was selected as that radius corresponding to the previously selected failure load. These radii are plotted in Figure 6-10 along with the theoretical results from Figure 5-20. Before any conclusions are reached from these results, it should first be noted that they confirm the occurrence of the velocity field due to Hill which was assumed in the previous chapter. The velocity field proposed by Prandtl, which requires a wedge of material directly under the punch, would require a much larger deforming region than was actually occurring. Secondly, the theoretical results shown in Figure 6-10 are lower limits, i.e., punch friction and initial indentation will cause the theoretical radius of the deforming region to increase. Therefore, corrections for these two factors should be made before the data can be properly interpreted. This was done for the case of $\phi = 41°$. The indentation was taken into account by adding a surcharge equivalent to the average initial indentation occurring in the tests. A correction for the punch friction was made by assuming the friction to be the limiting value of 7.5°. The stress characteristics and pressure distribution are shown in Figure 6-11. The outer-most second velocity characteristic for the case of coincidence of the directions of principal stress and strain rate is also shown in the figure by a heavy dotted line. It can be seen that the increase in the radius of the deforming region for this case is only some 10%. It should be noted that the corrections applied are overly conservative as evidenced by the fact that the failure pressure

Curve A: Coincidence of second stress and velocity characteristics
Curve B: Coincidence of principal stress and strain rate directions
Curve C: Coincidence of first stress and velocity characteristics

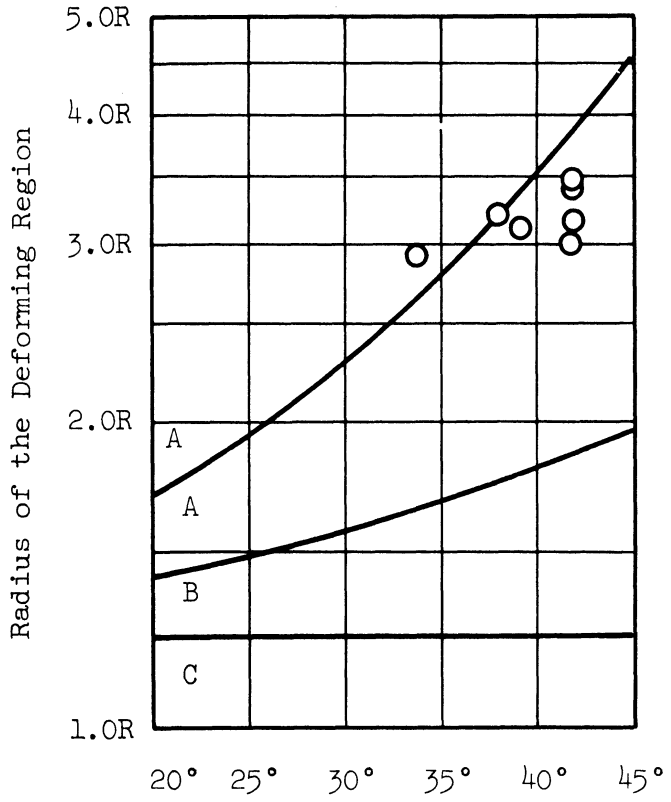

Figure 6-10. Experimental observations of the deforming region occurring in circular punch indentation tests.

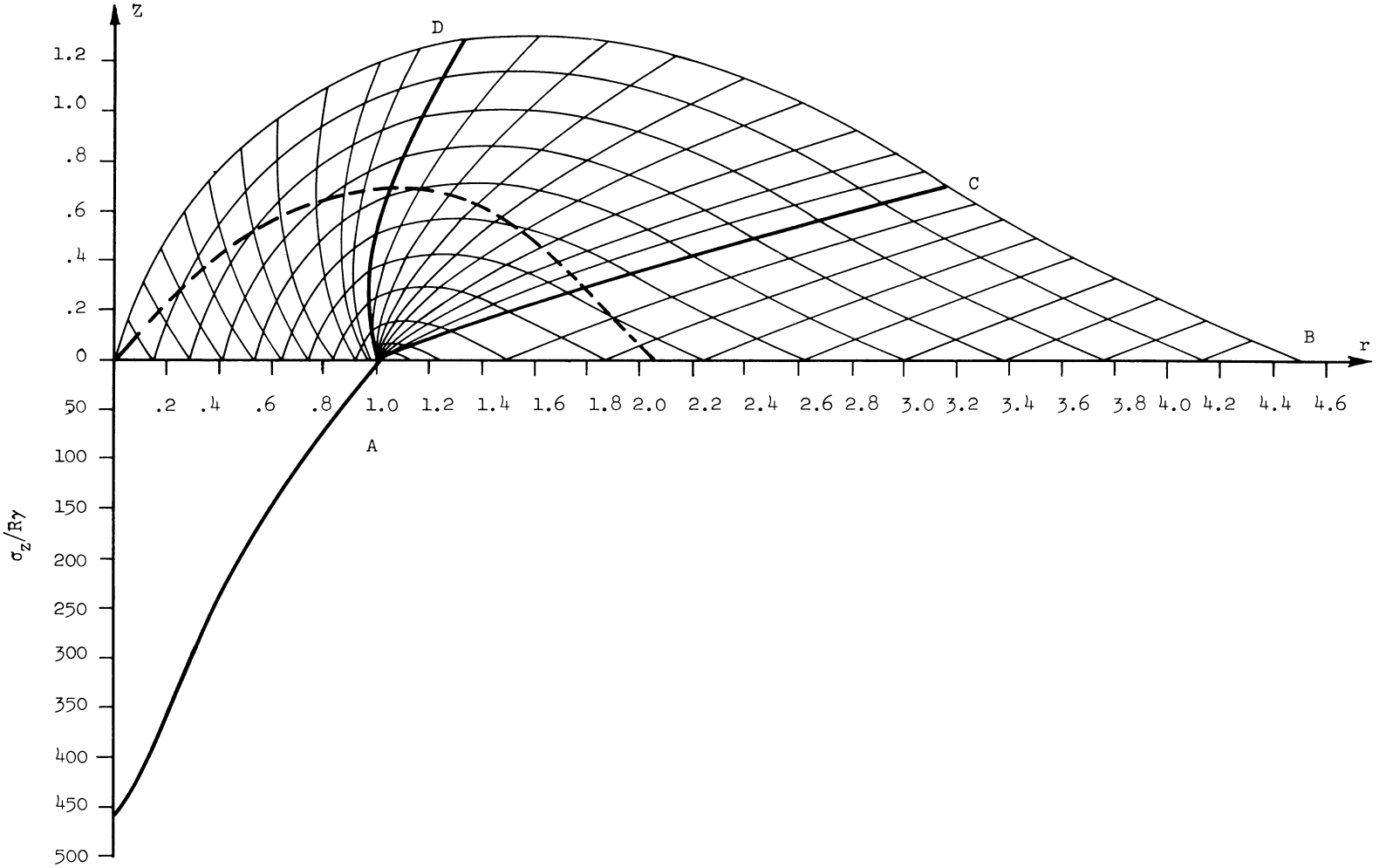

Figure 6-11. Stress characteristics and pressure distribution with corrections for punch friction and initial indentation.

given by the pressure distribution in Figure 6-11 is twice the actual value. With this upper bound case thus computed, it can be concluded from the data in Figure 6-10 that the deviation of the directions of principal stress and strain rate is quite close to the maximum amount.

CHAPTER VII

CONCLUSIONS

Analysis and experimental observations support the following conclusions regarding axially symmetric plastic failure of granular media:

1. A rigid-plastic, initial motion analysis of surface indentation will underestimate the indentation load except possibly for large angles of friction. Geometry changes during the process of failure have a significant effect on the predicted indentation load.
2. The dilatation rates predicted by the theory of plasticity are much larger than those observed.
3. The deviation of the directions of principal stress and strain rate may approach the maximum amount $1/2(\phi-\beta)$, predicted by the kinematic model.

REFERENCES

1. R. Hill, "On the State of Stress in a Plastic-Rigid Body at the Yield Point," Philosophical Magazine, 42, 1951, pp. 868-75.

2. D. C. Drucker, W. Prager, "Soil Mechanics and Plastic Analysis or Limit Design," Quart. of Applied Math., 10, No. 2, 1952, pp. 157-62.

3. R. T. Shield, "On Coulomb's Law of Failure in Soils," Journ. Mech. and Phys. Solids, 4, 1955, pp. 10-16.

4. P. Habib, "Influence de la Variation de la Constrainte Principale Moyenne sur la Resistance au Cisaillement des Sols," Proc. Third Internat. Conf. Soil Mech. and Found. Engrg., 1, 1953, pp. 131-36.

5. M. R. Peltier, "Recherches Experimentales sur la Courbe Intrinsique de Rupture des Sols Pulverulents," Proc. Fourth Internat. Conf. Soil Mech. and Found. Engrg., 1, 1957, pp. 179-82.

6. R. M. Haythornthwaite, "Mechanics of the Triaxial Test for Soils," Proc. Am. Soc. Civil Engr., 86, SM 5, 1960, pp. 35-62.

7. W. M. Kirkpatrick, "The Condition of Failure for Sands," Proc. Fourth Internat. Conf. Soil Mech. and Found. Engrg., 1, 1957, pp. 172-81.

8. T. H. Wu, A. K. Loh, and L. E. Malvern, "Study of Failure Envelope of Soils," Proc. Am. Soc. Civil Engr., 89, SM 1, 1963, pp. 145-81.

9. A. W. Bishop, A. K. Eldin, "The Effect of Stress History on the Relation Between ϕ and Porosity of Sand," Proc. Third Internat. Conf. Soil Mech. and Found. Engrg., 1, 1953, pp. 100-05.

10. P. G. Hodge Jr., Plastic Analysis of Structures. New York: McGraw-Hill, 1959.

11. S. Timoshenko, J. N. Goodier, Theory of Elasticity. New York: McGraw-Hill, 2nd ed., 1951.

12. Liang-Sheng Chen, "An Investigation of Stress-Strain and Strength Characteristics of Cohesionless Soils by Triaxial Compression Tests," Proc. Second Internat. Conf. Soil Mech. and Found. Engrg., 5, 1948, pp. 35-43.

REFERENCES (Continued)

13. A. Casagrande, W. L. Shannon, "Stress-Deformation and Strength Characteristics of Soils Under Dynamic Loads," Proc. Second Internat. Conf. Soil Mech. and Found. Engrg., 5, 1948, pp, 29-34 and A. Casagrande, W. L. Shannon, "Strength of Soils Under Dynamic Loads," Trans. Am. Soc. Civil Engr., 114, 1949, pp. 755-72.

14. R. V. Whitman, "The Behavior of Soils Under Transient Loadings," Proc. Fourth Internat. Conf. Soil Mech. and Found. Engrg., 1, 1957, pp. 207-10 and R. V. Whitman, K. H. Healy, "Shear Strength of Sands During Rapid Loading," Proc. Am. Soc. Civil Engr., 88, SM 2, 1962, pp. 99-132.

15. H. B. Seed, R. Lundgren, "Investigation of the Effect of Transient Loading on the Strength and Deformation Characteristics of Saturated Sands," Proc. Am. Soc. for Testing Matl., 54, 1954, pp.1288-1306.

16. B. de St. Venant, "Memoire sur l'establissement des equations differentialles des mouvements interieurs operes dans les corps solides ductiles au dela des limites ou l'elasticite pourrait les remener a leur premier etat," Journ. Math. pures et appl, 16, 1871, pp. 308-316.

17. M. Levy, "Extrait du Memoire sur les equations generales des mouvements interieurs des corps solides ductiles au dela des limites ou l'elasticite pourrait les ramener a leur premier etat; presente le 20 juin 1870," Journ. Math. pures et app., 16, 1871, pp. 369-372.

18. R. von Mises, "Mechanik der plastischen Formanderung von Kristallen," Zeitschrift fur Angewandte Mathematik und Mechanik, 8, 1928, pp. 161-185.

19. D. C. Drucker, "A More Fundamental Approach to Plastic Stress-Strain Relations," Proc. First U.S. National Congress of Appl. Mech., 1951, pp. 487-91.

20. A. D. Cox, G. Eason, and H. G. Hopkins, "Axially Symmetric Plastic Deformation in Soils," Trans. Royal Soc., 254, A. 1036, 1961, pp. 1-45.

21. K. H. Roscoe, A. H. Schofield, and C. P. Wroth, "On the Yielding of Soils," Geotechnique, 8, 1958, pp. 22-53.

REFERENCES (Continued)

22. K. H. Roscoe, "An Apparatus for the Application of Simple Shear to Soil Samples," Proc. Third Internat. Conf. Soil Mech. and Found. Engrg., 1, 1953, pp. 186-191.

23. A. W. Jenike, R. T. Shield, "On the Plastic Flow of Coulomb Solids Beyond Original Failure," Trans. Am. Soc. Mech. Engrs., 26, 1959 (J. Appl. Mech.), pp. 599-602.

24. D. C. Drucker, R. E. Gibson, and D. J. Henkel, "Soil Mechanics and Work-Hardening Theories of Plasticity," Trans. Am. Soc. Civil Engr., 122, 1957, pp. 338-346.

25. J. Brinch Hansen, Earth Pressure Calculations. Copenhagen: The Danish Tech. Press, The Inst. of Danish Civil Engrs., 1953.

26. J. R. Johanson, Andrew Jenike, "Stress and Velocity Fields in Gravity Flow of Bulk Solids," Engr. Exp. Station Bull. No. 116, Univ. of Utah, 1962.

27. R. Hill, The Mathematical Theory of Plasticity. New York: Oxford University Press, 1950.

28. G. de Josselin de Jong, Statics and Kinematics in the Failable Zone of a Granular Material. Delft: Uitgerig Waltman, 1959.

29. R. M. Haythornthwaite, "The Kinematics of Soils," Progress in Applied Mechanics. New York: Macmillan Co., 1963, pp. 235-250.

30. Shunsuke Takagi, "Plane Plastic Deformation of Soils," Proc. Am. Soc. Civil Engr., 88, No. EM3, 1962, pp. 107-51.

31. R. T. Shield, "Mixed Boundary Value Problems in Soil Mechanics," Quart. of Appl. Math., 11, 1953, pp. 61-75.

32. W. Sylwestrowicz, "Experimental Investigation of the Behaviour of Soil Under a Punch or Footing," Journ. Mech. and Phys. of Solids, 1, 1953, pp. 258-264.

33. E. T. Selig, K. E. McKee, "Static and Dynamic Behavior of Small Footings," Proc. Am. Soc. Civil Engr., 87, SM 6, 1961, pp. 29-47.

34. R. T. Shield, "On the Plastic Flow of Metals Under Conditions of Axial Symmetry," Proc. Royal Soc., Series A, 233, 1955, pp. 267-86.

REFERENCES (Concluded)

35. V. V. Sokolovski, Statics of Soil Media. London: Butterworth, 1956.

36. H. Lippmann, "Principal Line Theory of Axially-Symmetric Plastic Deformation," Journ. Mech. and Phys. of Solids, 10, 1962, pp. 111-22.

37. R. Hill, "The Plastic Yielding of Notched Bars Under Tension," The Quart. Journ. Mech. and Appl. Math., 2, 1949, pp. 40-51.

38. A. D. Cox, "Axially Symmetric Plastic Deformation in Soils-II. Indentation of Ponderable Soils," International Journ. of Mechanical Sciences, 4, 1962, pp. 371-80.

39. L. A. Larkin, "Axially Symmetric Indentation of Cohesionless Soils," Univ. of Mich. Tech. Report ORA-04403-10-T, 1963.

40. K. Terzaghi, Theoretical Soil Mechanics. New York: John Wiley and Sons, Inc., 1943.